OUKA
The University of Osaka
Institutional Knowledge Archive

Title	Structural design and electronic state control of carbon-based catalysts for hydrogen evolution reaction
Author(s)	Yang, Xinran
Citation	大阪大学, 2026, 博士論文
Version Type	VoR
URL	https://doi.org/10.18910/105521
rights	
Note	

The University of Osaka Institutional Knowledge Archive : OUKA

https://ir.library.osaka-u.ac.jp/

The University of Osaka

Structural design and electronic state control of carbon-based catalysts for hydrogen evolution reaction

Xinran Yang

March 2026

Structural design and electronic state control of carbon-based catalysts for hydrogen evolution reaction

A dissertation submitted to

THE GRADUATE SCHOOL OF ENGINEERING SCIENCE

THE UNIVERSITY OF OSAKA

in partial fulfillment of the requirements for the degree of

DOCTOR OF PHILOSOPHY IN ENGINEERING

BY

Xinran Yang

March 2026

Abstract

Structural design and electronic state control of carbon-based catalysts for hydrogen evolution reaction

Xinran Yang
Graduate School of Engineering Science, The University of Osaka

Green hydrogen, produced via water electrolysis, is acknowledged as the most effective method for reaching carbon neutrality in the future. Nonetheless, this process encounters a considerable challenge due to the high energy barrier associated with the hydrogen evolution reaction (HER), which significantly hinders progress. Therefore, the development of efficient and cost-effective HER catalysts is urgently needed. At present, noble metal catalysts are known for their minimal overpotential yet are limited by their rarity and high cost, rendering them impractical for an economy-driven approach. In contrast, carbon-based catalysts are economically friendly, but their application for HER is hindered by insufficient active sites and poor intrinsic activity. This research focuses on a systematic investigation into the electronic structure regulation and structure-activity relationships of carbon-based catalysts, aiming to provide theoretical foundations and practical references for enhancing their catalytic performance in the hydrogen evolution reaction.

Chapter 1 and 2 primarily elaborate on the research background and the evaluation methods for hydrogen evolution reaction catalysts. Chapter 3-5 focus on the preparation of carbon-supported/coated transition metal catalysts, while chapters 6-7 primarily introduce non-metal heteroatom-doped carbon materials.

Chapter 3 presents a flower-like carbon-coated transition metal alloy catalyst prepared through a combined CVD and hydrothermal approach. Layered double hydroxides (LDHs) was used as precursors, which could offer high specific surface area, exchangeable interlayer anions, and tunable active sites. The structure of LDHs is precisely regulated to enhance HER performance, with the main research focuses including: (1) The phosphorylation of LDHs via chemical vapour deposition (CVD) to regulate the hydrogen adsorption free energy($\triangle G_{H^*}$) of active sites. (2) Adopting CVD method for carbon coating to enhance the conductivity of LDHs, thereby accelerating charge transfer rates. (3) Employing MoO_4^{2-} chemical etching to increase the specific surface area of LDHs.

In Chapter 4, to address the limitations associated with the large size and intricate synthesis steps of the flower-like structures discussed in Chapter 3, a straightforward and eco-friendly one-step synthesis method was developed to prepare carbon-based materials loaded with nanosized transition metal phosphide particles. In this study, p Leveraging the chelating effect of phytic acid on transition metal elements, the agglomeration of CoP particles in the product was effectively restricted. A factorial analysis was conducted to evaluate the effects of temperature, precursor concentration, and precursor ratio on the material's surface area and particle size. By balancing the chelating capability of phytic acid with cobalt content, uniformly dispersed CoP nanoparticles with an average size of 23 nm were successfully synthesized. Moreover, the self-etching behavior of NH_3 derived from glycine decomposition on the carbon layer was investigated, along with its effect on modulating the conductivity through nitrogen doping.

In Chapter 5, based on the limiting effect of chelation on particle size described in Chapter 4, we utilized the spatial confinement effect of ion-exchange resins on transition metal species to develop a carbon-based catalyst loaded with nanoscale S-doped Co_2P particles. The synthesis path is recorded in Scheme 2. The Co_2P particles synthesized using this method exhibit a size of only 13 nm, demonstrating significantly enhanced catalytic activity compared to the catalysts in Chapter 3. Furthermore, this chapter investigates the feasibility of using SO_2 as a sulfur source for doping and analyzes the migration pathway of sulfur atoms derived from sulfonate groups. On this basis, the regulatory effect of S on the electronic structure of Co_2P was also analyzed.

In Chapter 6, we developed N, P co-doped carbon-based catalysts based on the crosslinking interaction mentioned in Chapter 4. By modulating precursor concentration, ultrathin heteroatom-doped carbon nanosheets were successfully prepared. Building on this, further optimization of precursor ratios and carbonization temperature yielded a series of products with gradient variations in N and P doping type and content. The synergistic doping mechanisms were investigated through experimental characterization and density functional theory (DFT) calculations. Crucially, for the inherent oxidation susceptibility of the C_3P structure, a synergistic model between C_3PO and nitrogen atoms was first constructed, effectively enhancing the adaptability of the doping system in practical applications.

In Chapter 7, building on the synergistic doping effect of graphitic nitrogen and the C_3PO structure revealed in Chapter 6, this chapter investigates the influence of precursor type on the distribution and content of nitrogen and phosphorus dopants in the final product. Using histidine and linear amino acids as comparative precursors, the research focuses on evaluating the optimization mechanism and enhancement effect of the imidazole ring on the catalytic performance of N, P-co-doped carbon-based materials, providing theoretical support and experimental evidence for the preparation of high-performance heteroatom-doped carbon-based catalysts.

In summary, novel synthesis methods for various carbon-based electrode catalysts were developed, and their structure–activity relationships were investigated. Furthermore, the electronic structure of carbon-based catalysts was modulated through heteroatom doping, and the synergistic doping mechanism was explored.

Table of contents

Abstract 1
Table of contents 4
Chapter 1 7
General introduction 7
1.1 Design Mechanism for catalysts toward HER 8
1.2 The classification and research progress of carbon-based HER Catalysts 12
1.3 The synthesis methods of carbon based catalyst 21
1.4 Overview of this study 25
Reference 26
Experimental evaluation of the catalysts for the hydrogen evolution reaction 30
2.1 Construction and working principle of the three-electrode system 30
2.2 Measurements 32
Reference 36
Fabrication of carbon-coated hierarchical Mo doped NiCo alloying catalyst for hydrogen evolution reaction 39
3.1 Introduction 39
3.2 Experiment 41
3.3 Results and discussion 42
3.4 Conclusion 46
Reference 47
Facile and cost-effective synthesis of CoP anchored N doped carbon with high catalytic performance for electrochemical hydrogen evolution reaction 51
4.1 Introduction 51
4.2 Experimental 54
4.3 Results and discussion 55
4.4 Conclusion 62
Reference 63
Straightforward synthesis of S-doped Co_2P nanoparticles on a P, S co-doped carbon substrate by using ion exchange resin for hydrogen evolution reaction 66
5.1 Introduction 66
5.2 Experimental 69
5.3 Results and discussion 71
5.4 Conclusion 77
Reference 79
Undemanding synthesis of N, P co-doped carbon nanosheets for hydrogen evolution reaction: Combining experimental quantitative analysis and DFT calculation corroboration 83
6.1 Introduction 83
6.2 Experimental 85

6.3 Results and discussion 87
6.4 Conclusion 103
Reference 104
Various amino acids serve as precursors for synthesizing nitrogen and phosphorus carbon materials 107
7.1 Introduction 107
7.2 Experimental 109
7.3 Results and discussion 111
7.4 Conclusion 113
Reference 116
General Conclusions 119
Acknowledge 122

Chapter 1

General introduction

Hydrogen stands as a promising energy carrier for supplanting fossil fuels in the future [1-5]. It is differentiated into gray, blue, and green hydrogen, depending on its production methods. Of these varieties, green hydrogen, produced via water electrolysis, is acknowledged as the most effective method for reaching carbon neutrality in the future. Nonetheless, this process encounters a considerable challenge due to the high energy barrier associated with the hydrogen evolution reaction (HER), which significantly hinders progress. Therefore, the development of efficient and cost-effective HER catalysts is urgently needed [6-9]. At present, the leading HER catalysts are categorized into noble metal and transition metal-based catalysts [10-13]. Precious metal catalysts are known for their minimal overpotential, but are limited by their rarity and high cost, making them impractical in economically driven methods [14-16]. In contrast, transition metal-based catalysts are economically friendly, but their application for HER is hindered by their low conductivity and tendency to aggregate at elevated temperatures, which compromises their suitability for HER tasks [17-18]. In the field of hydrogen evolution reaction (HER) catalysts, carbon-based materials have become a research focus due to their unique advantages. These materials are highly anticipated for their adjustable pore structure, which amplifies the exposure of active catalytic sites and accelerates the transfer of reactant species [19-24]. Additionally, their superior electrical conductivity facilitates rapid electron transfer, while their exceptional corrosion resistance ensures durability in both acidic and alkaline electrolytic environments over prolonged periods.

Despite these advantages, the intrinsic HER activity of most carbon-based catalysts remains significantly lower than that of platinum. To address this limitation, two main strategies have been widely explored: morphological engineering and electronic structure modulation. Structural design

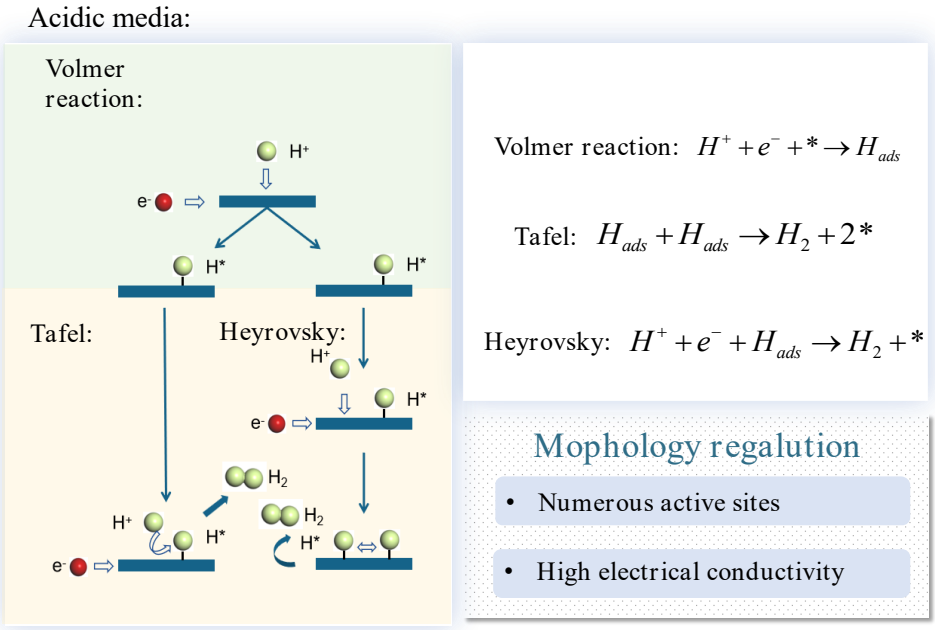

Figure 1. 1 The fundamental step of acidic HER.

aims to increase the density and accessibility of active sites, thereby enhancing the number of reaction events per unit time. Electronic regulation, on the other hand, focuses on optimizing the intrinsic activity of active sites by tuning their electronic properties, improving intermediate adsorption energies, and thus lowering kinetic barriers.

1.1 Design Mechanism for catalysts toward HER

1.1.1 The elementary steps of the HER Reaction

The reaction mechanism of HER depends strongly on the pH of the electrolyte. As this work is conducted in acidic media, only the HER pathways under acidic conditions are discussed here. In acidic electrolytes, HER proceeds via two elementary steps (**Figure 1.1**). The first is the Volmer step:

$$H^+ + e^- + * \rightarrow H^*$$

In this step, protons from the solution are reduced and adsorbed onto the catalyst surface to form adsorbed hydrogen species. In the subsequent step, molecular hydrogen is formed through either the Heyrovsky or Tafel pathway [25]:

$$H^+ + e^- + H^* \rightarrow H_2 + * \ (Heyrovsky)$$

$$H^* + H^* \rightarrow H_2 + 2* \ (Tafel)$$

The reaction depends on the surface coverage of hydrogen species. At low hydrogen coverage, H* reacts with a proton and an electron from the solution to form H_2 via the Heyrovsky reaction. At high hydrogen coverage, two neighboring H* species recombine to generate H_2 via the Tafel reaction, which is generally kinetically faster than the Heyrovsky step. At intermediate coverage, both pathways can coexist and contribute to hydrogen formation [26-27].

The rate-determining step of HER varies with applied potential. At low overpotentials, proton adsorption is sluggish and the Volmer step becomes rate-limiting. At higher overpotentials, proton adsorption becomes facile, and the desorption or recombination of adsorbed hydrogen becomes the dominant kinetic bottleneck.

1.1.2 The kinetic model of HER

To rationally optimize HER catalyst design, it is essential to establish kinetic models that incorporate intrinsic catalyst properties and relate them to experimentally accessible electrochemical parameters. One of the earliest and most widely used descriptions was proposed by Julius Tafel in 1905, based on extensive measurements of polarization curves during hydrogen evolution. He derived the Tafel equation:

$$\eta = a + b\log j$$

where η is the overpotential, j is the current density, and b is the Tafel slope. This relationship describes the logarithmic dependence of overpotential on current density in the strongly polarised regime and provides a direct link between reaction kinetics and measurable electrochemical behaviour[28-29].

Following the formulation of the Tafel equation, the Butler–Volmer equation was subsequently developed through the combined contributions of Volmer, Butler, and Grúž, leading to a more rigorous kinetic description of electrode processes. Volmer first proposed that the activation energy of the electron-transfer step governs the rate of an electrochemical reaction and varies systematically with the

applied electrode potential. Butler then integrated thermodynamic principles with reaction kinetics to quantify the relationship between electrode potential and activation energy, thereby introducing and physically interpreting the charge-transfer coefficient. Building on this framework, Grúž further refined the derivation by accounting for the coupling between anodic and cathodic processes. The resulting Butler–Volmer equation is expressed as:

$$j = j0[\exp((\alpha anF\eta)/(RT)) - exp(-(\alpha cnF\eta)/(RT))]$$

where j0 is the exchange current density, α a and α c are the anodic and cathodic transfer coefficients, n is the number of electrons transferred, and F is the Faraday constant. The overpotential is denoted by η, while R and T are the gas constant and absolute temperature, respectively. At sufficiently high overpotentials, the equation can be simplified to:

$$j \approx j_0 \exp(\alpha_a n F \eta/RT)$$

which leads to the familiar Tafel form:

$$\eta = a - b \log|j|$$

According to kinetic theory, a Tafel slope of approximately 120 mV dec^{-1} corresponds to a Volmer rate-determining step. A slope of about 40 mV dec^{-1} is associated with the Volmer–Heyrovsky pathway, whereas a slope near 30 mV dec^{-1} indicates a Volmer–Tafel mechanism [30-31].

In practice, however, most experimentally measured Tafel slopes do not coincide exactly with these three ideal values. This discrepancy reflects a key limitation of the Butler–Volmer framework, namely that it does not explicitly account for intrinsic catalyst properties such as surface structure, electronic configuration, crystallographic orientation, and defect density. As a result, the model cannot fully capture the kinetic diversity of multicomponent catalysts with different facets, compositions, and surface heterogeneities, and additional theoretical and computational approaches are required to describe mixed or intermediate reaction pathways.

Platinum, particularly the Pt (111) surface, has been extensively studied as a model HER catalyst, yet the exact reaction pathway on Pt remains a subject of debate. There is broad agreement that the Volmer step proceeds rapidly on platinum surfaces and that hydrogen desorption is the principal rate-limiting process. However, whether desorption occurs predominantly through the Heyrovsky or Tafel mechanism is still unresolved.

Early studies suggested that HER activity was largely insensitive to surface crystallography, but more

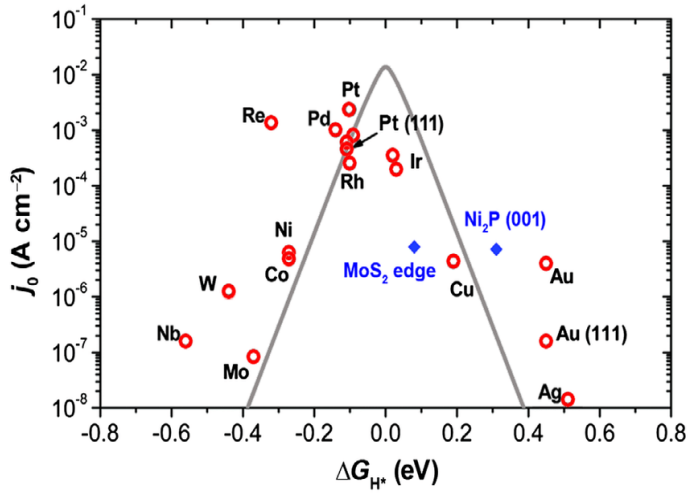

Figure 1. 2 The volcano plot of the various catalysts.

recent work has demonstrated that reactivity is strongly influenced by structural features such as crystal orientation, step density, and surface defects. Furthermore, the size of metal nanoparticles can modulate HER performance by altering the relative exposure of different crystallographic facets and edge sites [32-33].

1.1.3 The volcano curve theory

The relationship between catalytic activity and hydrogen adsorption strength is commonly described by the volcano plot in electrocatalysis (**Figure 1.2**). According to this model, optimal catalytic performance is achieved when the binding strength between the active site and the intermediate reaction is neither too strong nor too weak. Excessively strong adsorption hampers desorption and product release, whereas overly weak adsorption limits intermediate formation. A moderate binding strength therefore provides a balance between adsorption and desorption kinetics, leading to maximal reaction rates and superior catalytic activity. The development of volcano-plot theory has progressed through several key stages. The conceptual foundation was laid by Paul Sabatier in 1913, who proposed that catalytic activity depends on the strength of interaction between the catalyst and reactants. If the binding is too weak, adsorption becomes inefficient; if it is too strong, intermediates bind excessively to the surface, hindering desorption and blocking active sites, which ultimately suppresses catalytic turnover. Building on this concept, Parsons et al. in 1958 developed an electrocatalytic kinetic framework that integrated the elementary steps of the hydrogen evolution reaction with the Butler–Volmer formalism. This approach enabled a quantitative relationship to be established between the exchange current density and the free energy of hydrogen adsorption. Later, in 2003, Nørskov et al. further advanced this idea by constructing a direct correlation between hydrogen adsorption free energy and electrocatalytic activity, and by introducing density functional theory (DFT) as a predictive tool for catalyst screening and performance evaluation[34-35].

Dai et al. [36] subsequently investigated the $La_2Sr_2PtO_7$ catalyst using DFT calculations to model hydrogen adsorption under acidic conditions. They constructed (001) surface slab models with different surface terminations and optimized their geometries to describe the three elementary states of the acidic HER pathway. Free-energy calculations at various adsorption sites showed that hydrogen binding at the O site was significantly stronger than thermoneutral ($\Delta G_{H^*} \ll 0$), indicating that hydrogen desorption is kinetically unfavorable. In contrast, adsorption at Pt sites was too weak ($\Delta G_{H^*} \gg 0$), making proton adsorption inefficient. The hydrogen binding energy (HBE) is a core thermodynamic parameter that characterizes the interaction between the catalyst surface and adsorbed hydrogen atoms. It directly determines the intrinsic catalytic activity of the catalyst for the hydrogen evolution reaction (HER). Derived from the Sabatier principle, the HBE concept states that an optimal catalyst should exhibit a moderate interaction strength with reaction intermediates: excessively strong interactions hinder intermediate desorption, while excessively weak interactions impede sufficient reactant adsorption. Notably, the La–Pt bridge site exhibited a hydrogen adsorption free energy close to zero, identifying it as the primary active center of the catalyst. Moreover, when compared with the Pt (111) surface, the ΔG_{H^*} value at the La–Pt bridge site was even closer to the thermoneutral condition, suggesting a potentially superior balance between adsorption and desorption kinetics. Li et al. constructed a series of NiCoRu alloy models to quantify the effect of Ru doping on the electronic structure of NiCo alloys. Different surface doping configurations with increasing Ru concentrations

were considered, including a limiting case in which Ru atoms fully covered the alloy surface. The calculations showed that the fully Ru-covered surface exhibits the most thermoneutral hydrogen adsorption free energy. Compared with pristine NiCo alloys, Ru doping significantly enhances hydrogen adsorption kinetics and lowers the energy barrier of the Volmer step by approximately 0.4 eV, thereby accelerating proton reduction. Fung et al. [37] investigated transition-metal-doped, nitrogen-containing graphene systems and systematically compared how different metal dopants regulate the electronic structure of the carbon framework. Their results indicated that the smaller the graphene domain, the more strongly the transition metal contributes to the overall electronic structure of the catalyst. As a result, the hydrogen adsorption free energy (ΔG_{H^*}) of small-sized, metal-doped graphene is reduced by about 0.3 eV compared with that of larger graphene configurations. This moderation of ΔG_{H^*} substantially improves proton adsorption kinetics on carbon active sites and promotes the overall water electrolysis reaction.

1.1.4 D bond theory

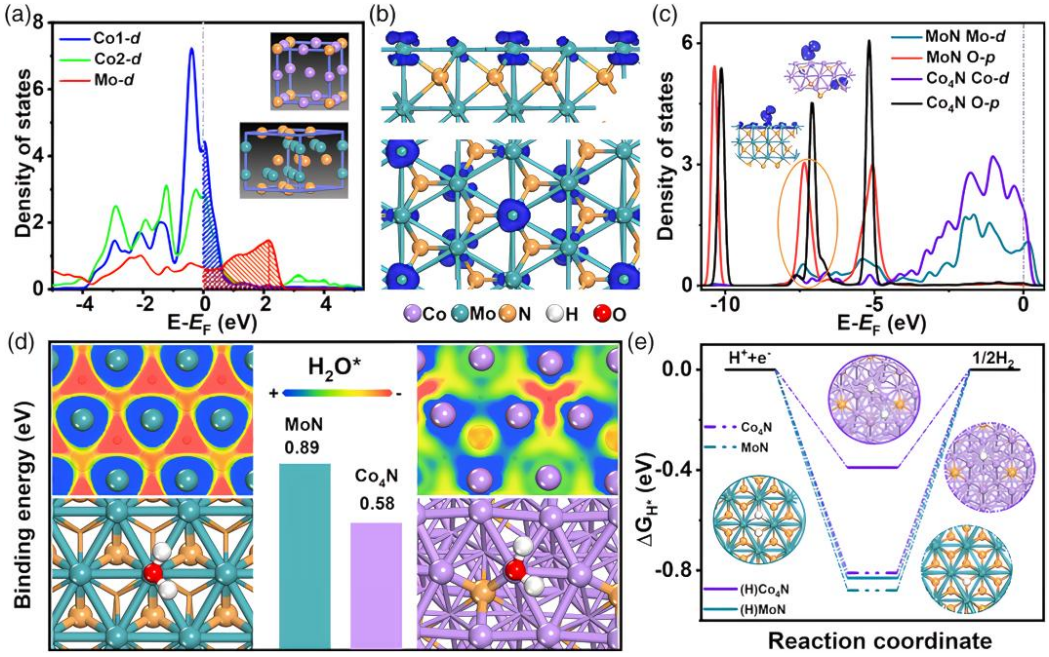

Figure 1. 3 (a) Calculated PDOS of d-band for Co and Mo. (b) The orbital analysis for Mo of the strongest peak above EF. (c) The electron density differences of MoN(001) and Co_4N(111). (d) The PDOS of Mo-d, Co-d, and O-p. (e) ΔG_{H^*} on MoN, (H)MoN, Co_4N, and (H)Co_4N [38].

Since the mid-20th century, the evolution of d-band theory has fundamentally shaped the design of hydrogen evolution reaction (HER) catalysts. Early research recognized the importance of transition metal d electrons, but lacked quantitative tools, making catalyst development largely dependent on experience. Through advances in surface science and quantum chemistry, researchers have established the physical definition of the d-band center (ε_d) and its relationship with adsorption energy.

$$\varepsilon_d = \frac{\int_{-\infty}^{E_F} E \cdot n_d(E)\, dE}{\int_{-\infty}^{E_F} n_d\,(E)\, dE}$$

Here, $n_d(E)$is the density of the d state. When ε_d approaches the Fermi level, the overlap between the metal d orbitals and the adsorbate orbitals increases, enhancing adsorption. The rise of density functional theory (DFT) has enabled quantitative prediction of ε_d and the correlation between ε_d and the hydrogen adsorption free energy ΔG_{H^*}:

$$\Delta G_{H^*} \approx \alpha(\varepsilon_d - \varepsilon_0)$$

where α is a material-dependent coefficient, and ε_0 is a reference energy. This linear relationship explains the volcano-type activity trend for HER and guides rational design—alloying, nano

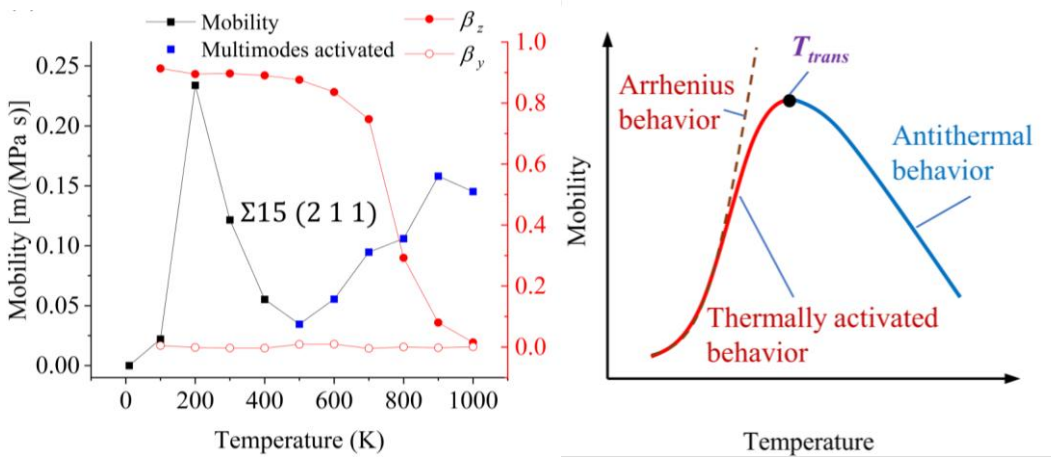

Figure 1. 4 Illustration of the thermally activated behavior, the anti-thermal behavior , and the transition temperature *T*rans.

structuring, and defect engineering can tune ε_d to optimize ΔG_{H^*}. Recent in-situ studies further reveal how ε_d shifts under working conditions:

$$\varepsilon_d(U) = \varepsilon_d^0 + \gamma(U - U_0)$$

Where U represents electrode potential and γ represents potential response coefficient. This dynamic view shifts the design from static optimization to operational adaptability [38].

Nowadays, the combination of d-band theory with high-throughput computing, machine learning, and multi-scale modeling has formed a complete descriptor-driven framework (**Figure 1. 3**). Its progress has transformed HER catalyst design from trial-and-error screening to rational electronic structure engineering, providing a clear physical pathway for developing efficient, stable, and cost-effective electrocatalysts.

1.2 The classification and research progress of carbon-based HER Catalysts

1.2.1 Transition metal species/carbon-based catalyst

Transition-metal-based species, including both alloys and compounds, exhibit Pt-like d-band electronic structures and typically possess moderate hydrogen adsorption free energies (ΔG_{H^*}), which are favorable for the hydrogen evolution reaction. However, transition metal alloys are prone to surface

segregation and particle sintering at elevated temperatures, leading to the coverage of active sites and progressive catalyst deactivation. In transition metal compounds, the incorporation of non-metallic elements weakens the metallic character of the transition metals, resulting in reduced electrical conductivity. These compounds can also suffer from agglomeration under thermal or electrochemical stress, which further compromises catalytic stability. Carbon-based materials, by contrast, exhibit high electrical conductivity and structural robustness, and carbon atoms migrate only slowly at elevated temperatures, making carbon frameworks intrinsically resistant to aggregation. Nevertheless, purely carbonaceous materials generally show overly positive hydrogen adsorption free energies, which leads to sluggish proton adsorption kinetics and insufficient surface hydrogen coverage. As a result, carbon materials alone usually display limited intrinsic HER activity. Combining transition metal species with carbon materials, therefore, creates a strong synergistic effect. In such composite systems, transition metal species act as the primary active centers, while the carbon scaffold serves multiple functional roles. It enhances electronic conductivity and increases the accessible surface area, thereby facilitating rapid charge transport and reactant diffusion. At the same time, the carbon framework effectively disperses and stabilizes nanoscale metal species, suppresses their aggregation, and maximizes the exposure of catalytically active sites. Owing to this complementary interaction, transition metal–carbon composites generally outperform their single-component counterparts in terms of catalytic activity, durability, and cost efficiency. This makes them highly attractive candidates for the development of efficient, stable, and economically viable non-precious-metal catalysts for the hydrogen evolution reaction [39-40].

1.2.1.1 Transition alloy/carbon substrate catalyst

Transition metal alloys combine favorable hydrogen adsorption free energies with high electrical conductivity. However, compared with transition metal compounds, they exhibit much higher atomic mobility at elevated temperatures. The metallic bonds in these alloys are relatively weak and non-directional, which leads to low diffusion barriers and facilitates rapid surface atom migration. Consequently, transition metal alloys are highly susceptible to Ostwald ripening upon thermal treatment, resulting in particle growth, loss of active surface area, and eventual catalyst deactivation. To suppress atomic diffusion and structural coarsening, carbon coating is widely employed to immobilize transition metal alloys. In addition, transition metal alloys are prone to oxidation in air and corrosion in acidic or alkaline environments, whereas a carbon shell can effectively isolate the metal core from aggressive species and thereby enhance long-term stability. Song et al. investigated Ni atom migration along grain boundaries and derived a temperature-dependent migration rate based on theoretical calculations. Their results showed that below 500°C, the migration rate of Ni increases sharply with temperature, with the maximum rate typically occurring in this temperature range. This observation highlights the necessity of introducing carbon materials to restrain atomic mobility during catalyst synthesis and operation (**Figure 1. 4**) [41].

Among transition metal alloys, nickel-based systems generally exhibit the highest intrinsic HER activity and are therefore widely used as active centres. Mohanty et al[42]. prepared nitrogen-doped carbon-coated NiCo alloy nanoparticles by complexing Ni and Co ions with organic ligands followed by pyrolysis. To elucidate the role of nickel, alloying models of Co with various metals (Ni, Mn, Fe, and Zn) were constructed and analyzed by DFT. Among these alloys, NiCo exhibited the most favorable

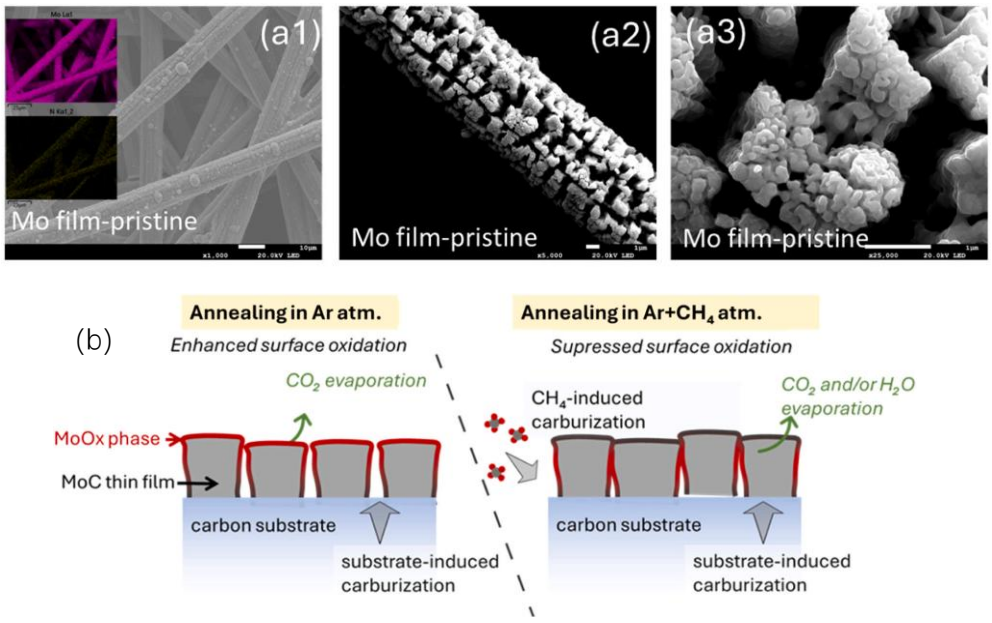

Figure 1. 5 (a1-a3) SEM images of Mo composites deposited on carbon paper. (b) Schematic illustration depicting the annealing step in argon and methane atmosphere. [44]

local electronic states near the Fermi level, indicating a more thermoneutral ΔG_{H^*} compared with either pure metals or other alloy combinations.

Xiao et al. [43] further reported the construction of NiCo–$NiCoO_2$/NC heterostructures using NiCo LDHs as precursors. During thermal treatment, the LDHs were carbonized to "freeze" the structural framework, while transition metal oxides at the interface between the carbon matrix and the LDHs were simultaneously reduced to form thin NiCo alloy films. The resulting heterostructure exhibited pronounced synergistic effects between the alloy and the carbon support. Moreover, the presence of the carbon layer ensured excellent structural stability, allowing the catalyst to operate continuously for more than 50 hours in alkaline electrolyte without significant degradation.

1.2.1.2 Transition metal carbides (TMCs)/Carbon substrate catalyst

In transition metal carbides (TMCs), covalent bonding between the metal and carbon atoms shifts the d-band centre of the transition metal to lower energies. This downshift weakens the binding strength between the metal sites and hydrogen intermediates, thereby facilitating hydrogen desorption and accelerating HER kinetics. At the same time, the strong metal–carbon bonding enhances resistance to acid and alkaline corrosion, making TMCs less susceptible to dissolution or oxidation in harsh electrolytes and thus extending their operational lifetime. Because the metal atoms are covalently anchored to the carbon framework, their migration at elevated temperatures is strongly suppressed, and detachment of active species from the support is effectively prevented.

Among transition metals, molybdenum forms particularly strong bonds with carbon and exhibits one of the highest metal–carbon bond energies, resulting in exceptional structural and chemical stability. As a result, Mo_2C has been widely explored as an active phase for HER electrocatalysis. Chaitog lou et al[44]. prepared columnar N-doped carbon-coated Mo_2C materials by combining pulsed laser deposition and chemical vapour deposition. In their approach, N-doped Mo precursors were first deposited by pulsed laser deposition, after which methane was used as a carbon source to grow carbon thin films on

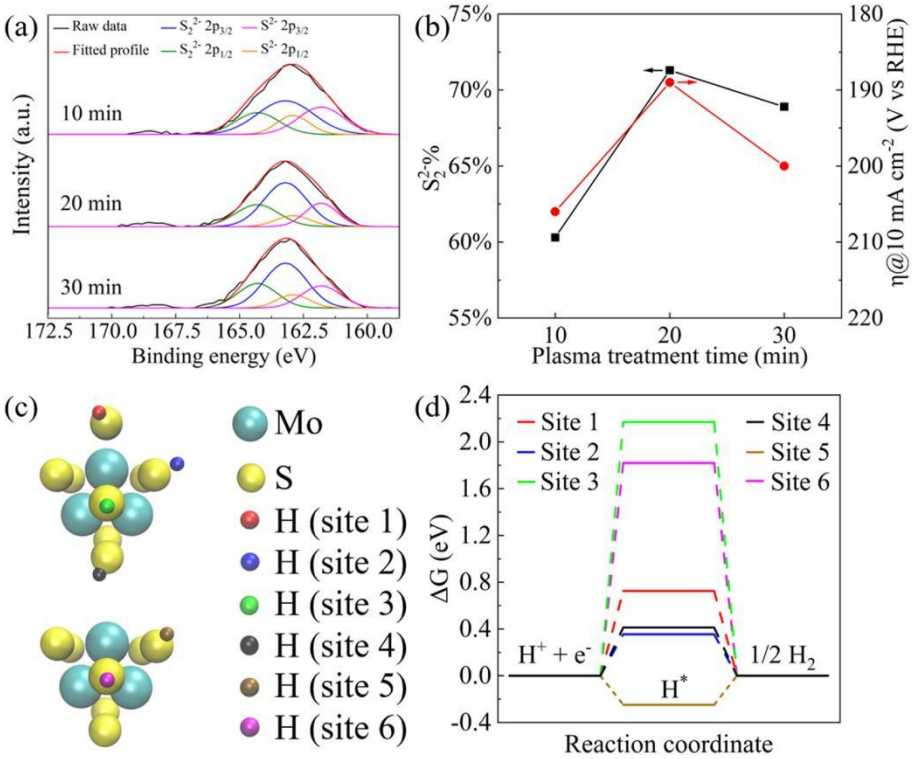

Figure 1. 6 (a1-a3) SEM images of Mo composites deposited on carbon paper. (b) Schematic illustration depicting the annealing step in argon and methane atmosphere. [46]

the Mo surface. X-ray photoelectron spectroscopy confirmed the formation of a Mo_2C interfacial layer between Mo and carbon (**Figure 1. 5**).

Electrochemical impedance spectroscopy further showed that the conductivity of the Mo_2C/NC catalyst was several orders of magnitude higher than that of N-doped Mo prepared by inert-gas annealing. Gong et al [45]. synthesized carbon-supported heterojunction catalysts using nitrogen-rich biomass as the carbon precursor. The resulting biomass-derived carbon possessed a high specific surface area and a hierarchical porous structure, which effectively suppressed aggregation of the transition metal species. A Mo_2C layer formed at the Mo–carbon interface, with one side bonded to the carbon support and the other to Mo, thereby significantly enhancing both electrical conductivity and structural stability.

Interestingly, the heterojunction also modulated the electronic structure of the surrounding carbon matrix. This regulation rendered the adjacent carbon atoms catalytically active, with a near-thermoneutral hydrogen adsorption free energy ($\Delta G_{H^*} \approx 0.01$ eV), indicating that the primary active sites in this system reside on the carbon atoms adjacent to the Mo_2C interface.

1.2.1.3 transition metal sulfide (TMSs)/Carbon substrate catalyst

Unlike most transition metal compounds, transition metal sulfides (TMSs) possess a layered structure composed of stacked two-dimensional sheets, analogous to graphene. Strong covalent bonding dominates within each layer, whereas adjacent layers are held together by comparatively weak van der Waals interactions. In Mo-based sulfides, each Mo atom in the basal plane is coordinated by six sulfur atoms, leading to a fully saturated coordination environment and intrinsically low HER activity. In contrast, Mo atoms located at edge sites are coordinatively unsaturated and exhibit ΔG_{H^*} much closer to the thermoneutral value, which makes them the primary active centres for hydrogen evolution.This

structural anisotropy implies that, for TMSs, catalytic optimisation relies more on morphological control than on bulk compositional tuning. Rather than forming large, continuous basal planes, structures with abundant edges and defects are preferred in order to maximise the density of exposed active sites. Among the various transition metal sulfides, MoS_2 has attracted particular attention because of its rich polymorphism and the ease with which its phase and morphology can be engineered. Bhavanari et al[46]. grew MoS_x nanoparticles with an average size of approximately 3 nm on nitrogen-doped carbon cloth. The ultrasmall particle size ensured a high density of edge sites, while the conductive N-doped carbon substrate facilitated rapid charge transport during electrocatalysis. Notably, MoS_x was found to nucleate preferentially at graphitic nitrogen sites and to form strong interfacial bonds with nitrogen atoms. This enhanced anchoring suppressed particle migration and aggregation, thereby maintaining a small particle size and significantly improving HER performance (**Figure 1. 6**). Zhang et al[47]. reported the room-temperature synthesis of molybdenum sulfide/graphene composites using plasma treatment. By varying the plasma exposure time, the loading and distribution of active molybdenum sulfide species could be precisely tuned, providing an additional route to optimize catalytic activity.

1.2.1.4 Transition metal phosphide (TMPs)/carbon substrate catalyst

Phosphorus readily reacts with most transition metals at relatively low temperatures to form thermodynamically stable transition metal phosphides (TMPs). A wide range of TMP systems has therefore been investigated, as summarized in **Figure 1.7**(a). By adjusting the stoichiometric ratio between phosphorus and the metal precursor, TMPs with diverse crystal structures and distinctive morphologies can be obtained. Nickel phosphides provide a representative example, and the various

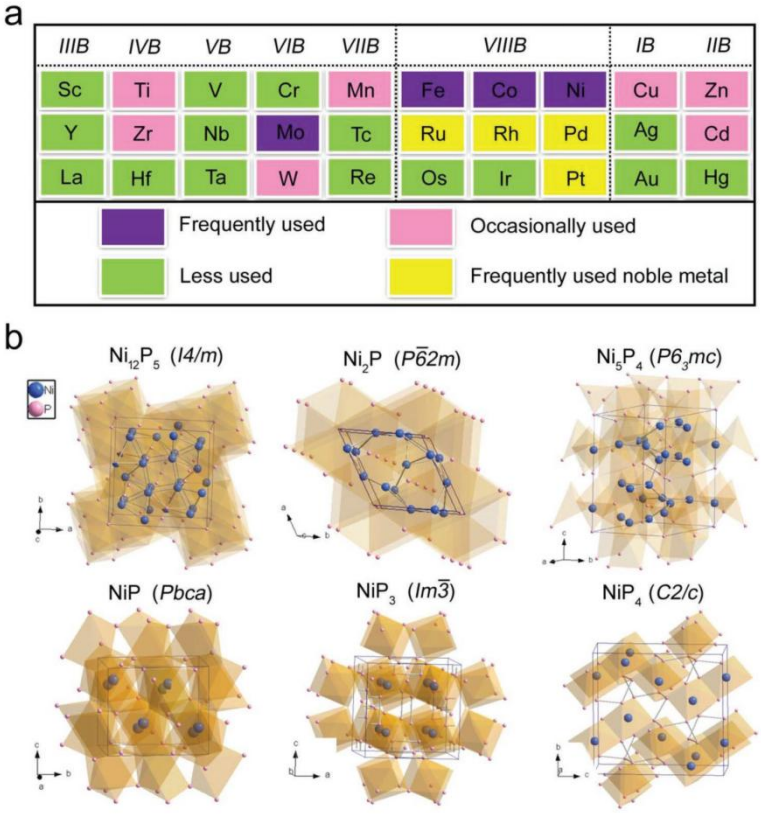

Figure 1. 7(a) Elements that are used to form TMPs for electrocatalysis. (b) Selected polyhedral representation of the nickel phosphides lattice based on the Ni polyhedra. [48]

accessible crystal phases are shown in **Figure 1. 7**(b). Compared with transition metal oxides and sulfides, TMPs exhibit superior electrical conductivity, which facilitates electron transfer and accelerates the Volmer step of HER. In addition, TMP crystals often expose a high density of surface facets, providing abundant active sites and enhancing surface hydrogen coverage. From an electrochemical perspective, transition metal oxides are generally unstable in acidic media, whereas transition metal sulfides typically show reduced activity in alkaline or neutral electrolytes. In contrast, TMPs maintain good stability across a wide pH range. Owing to their mild synthesis conditions, excellent resistance to acid and alkaline corrosion, and tunable structures, TMPs have therefore attracted considerable interest as active HER catalysts.

Riyajuddin et al [49]. fabricated a three-dimensional carbon-based self-supported system by growing graphene and carbon nanotubes on nickel foam using chemical vapor deposition, followed by the formation of a $Ni_2P–CuP_2$ heterojunction via Cu deposition and subsequent phosphorylation. This hierarchical carbon framework provided both a very high specific surface area and excellent electrical conductivity. Moreover, the strong interaction between TMPs and the carbon substrate increased structural disorder and defect density, generating additional active sites. Combined experimental measurements and DFT calculations demonstrated that the Ni_2P/CuP_2 heterojunction effectively regulates the hydrogen adsorption free energy at Ni sites by downshifting the d-band center, thereby improving HER performance. Liu et al. [50] reported the growth of carbon quantum dots on nickel foam, followed by the deposition of CoP nanoparticles onto the carbon quantum dot layer. The resulting material consisted of sea-urchin-like cobalt phosphide microspheres. This architecture exhibited high catalytic activity and long-term stability, which were attributed to its large surface area and the strong

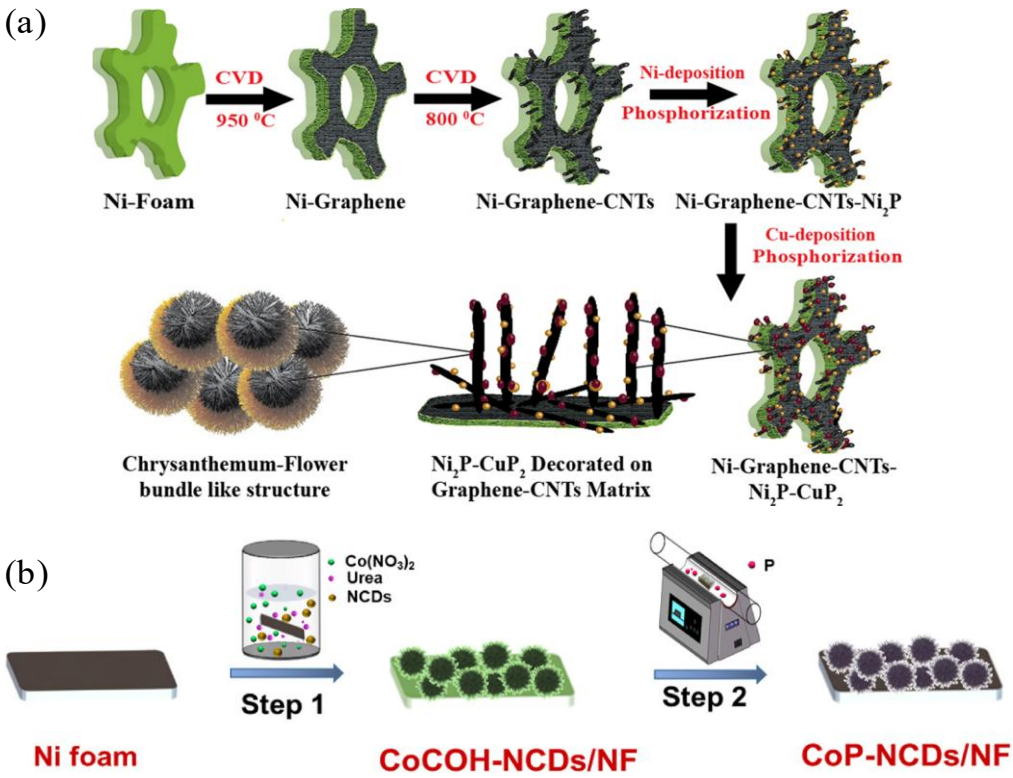

Figure 1. 8 (a) Schematic illustration depicting the synthesis process of Ni_2P-CuP_2/CNTs [49]. (b) Schematic illustration of the synthesis process of CoP-NCDs/NF [50].

interfacial interaction between the carbon quantum dots and CoP (**Figure 1. 8**).

1.2.2 Metal free carbon catalysts

Pure carbon is abundant and inexpensive; however, its ΔG_{H^*} is typically too positive, which hinders proton adsorption on active sites and leads to intrinsically poor HER activity. In recent years, it has been demonstrated that introducing heteroatoms with markedly different electronegativities from carbon (such as N, S, B, P, F, and O) into the carbon lattice can effectively modulate the local electronic structure, optimize the adsorption and desorption behavior of reaction intermediates, and thereby enhance the overall catalytic performance.

As a result, heteroatom-doped carbon materials have attracted considerable attention as promising alternatives to noble-metal catalysts. Compared with transition-metal-based catalysts, non-metallic carbon catalysts offer several distinct advantages: (1) the active sites created by heteroatom doping are more uniformly distributed, resulting in more homogeneous catalytic behavior; (2) carbon materials exhibit excellent resistance to acidic and alkaline corrosion as well as oxidation, which confers superior long-term stability; (3) unlike metal/carbon composites, they do not suffer from metal leaching or active phase detachment during ultrasonic dispersion; and (4) they are generally less expensive and easier to synthesize than nanoscale metal catalysts.

1.2.2.1 N-doped carbon catalyst

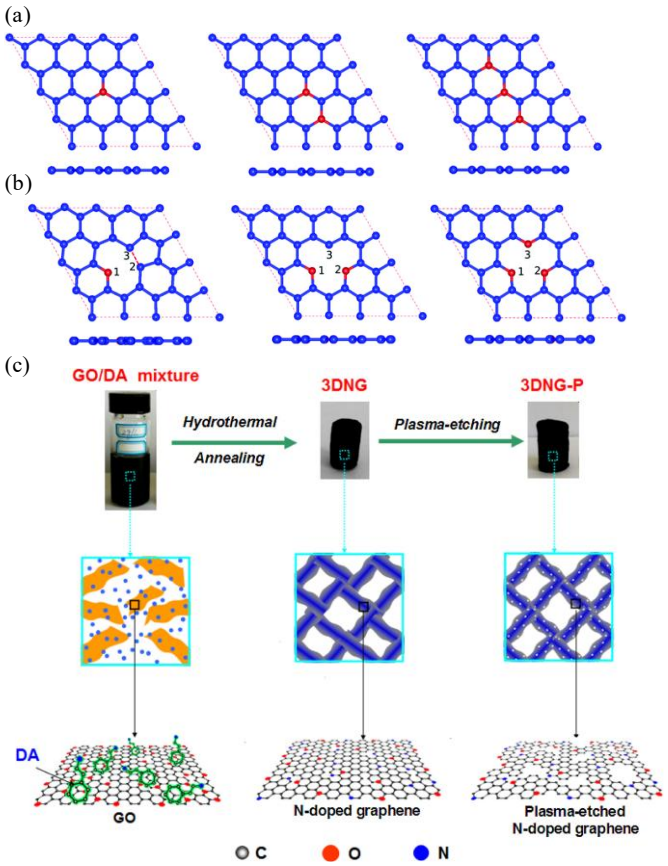

Figure 1. 9 (a) The model of N-doped graphene [51]. (b) Schematic illustration of the synthesis process of 3DNG-P [51].

Among the various non-metal dopants, nitrogen is the most extensively studied element for tuning the

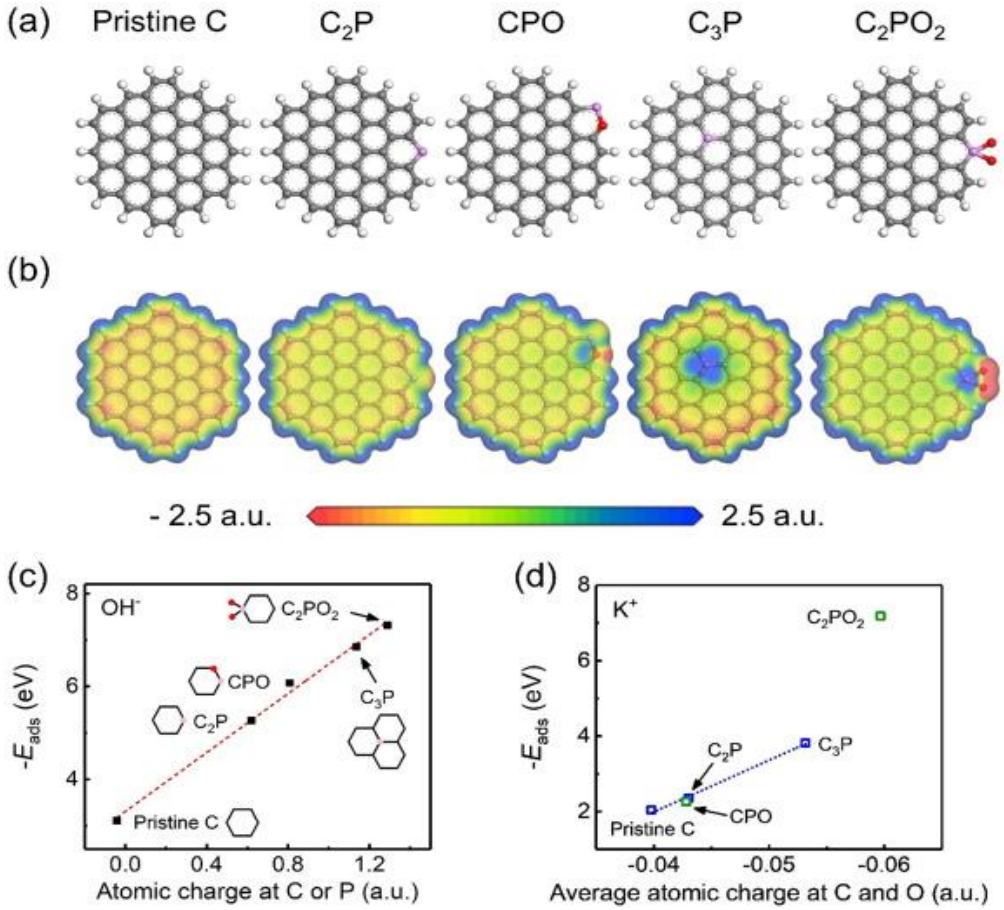

Figure 1. 10 (a) The model of P-doped graphene. (b) The ESP images of P-doped graphene. (c-d) The atomic charge at C, P or O [54].

electronic structure of carbon materials. In graphitic lattices, nitrogen is mainly incorporated in three configurations—pyridinic N, pyrrolic N, and graphitic (quaternary) N—which interact differently with the surrounding carbon π-conjugated network and therefore lead to distinct electronic and catalytic effects. Pyridinic and pyrrolic nitrogen are classified as edge-type dopants and are typically located at graphene edges or vacancy defects. Pyrrolic nitrogen is bonded to two carbon atoms within a five-membered ring and contributes two π-electrons to the π-system, whereas pyridinic nitrogen substitutes a carbon atom in a six-membered ring and contributes one p-electron. In contrast, graphitic nitrogen is incorporated within the basal plane of the carbon lattice, where it participates in the conjugated system through its lone pair and donates electron density to the sp^2 network (**Figure 1. 9**) [51].

Joonhee Moon et al. [52] synthesized nitrogen-doped carbon quantum dots via a top-down strategy. Graphene films were first grown on copper foil by chemical vapor deposition, followed by nitrogen plasma treatment to fragment the graphene into quantum dots while simultaneously introducing nitrogen dopants. The resulting quantum dots could either be dry-transferred using PMMA as a support or extracted into organic solvents, and uniform dispersion on porous silicon substrates yielded particles with an average size of approximately 5 nm, which exhibited excellent HER activities Tian et al. [53] prepared cylindrical hydrogel precursors from dopamine and graphene oxide by hydrothermal synthesis, and subsequently converted them into nitrogen-doped nanosheets by pyrolysis. Plasma etching introduced uniformly distributed mesopores of about 2 nm on the graphene surface. Although Raman spectroscopy indicated a decrease in the degree of graphitization after plasma treatment, the

overall electrocatalytic activity toward water splitting was enhanced, which was attributed to the increased specific surface area and the higher density of accessible active sites provided by the mesoporous structure.

1.2.2.2 P-doped carbon catalyst

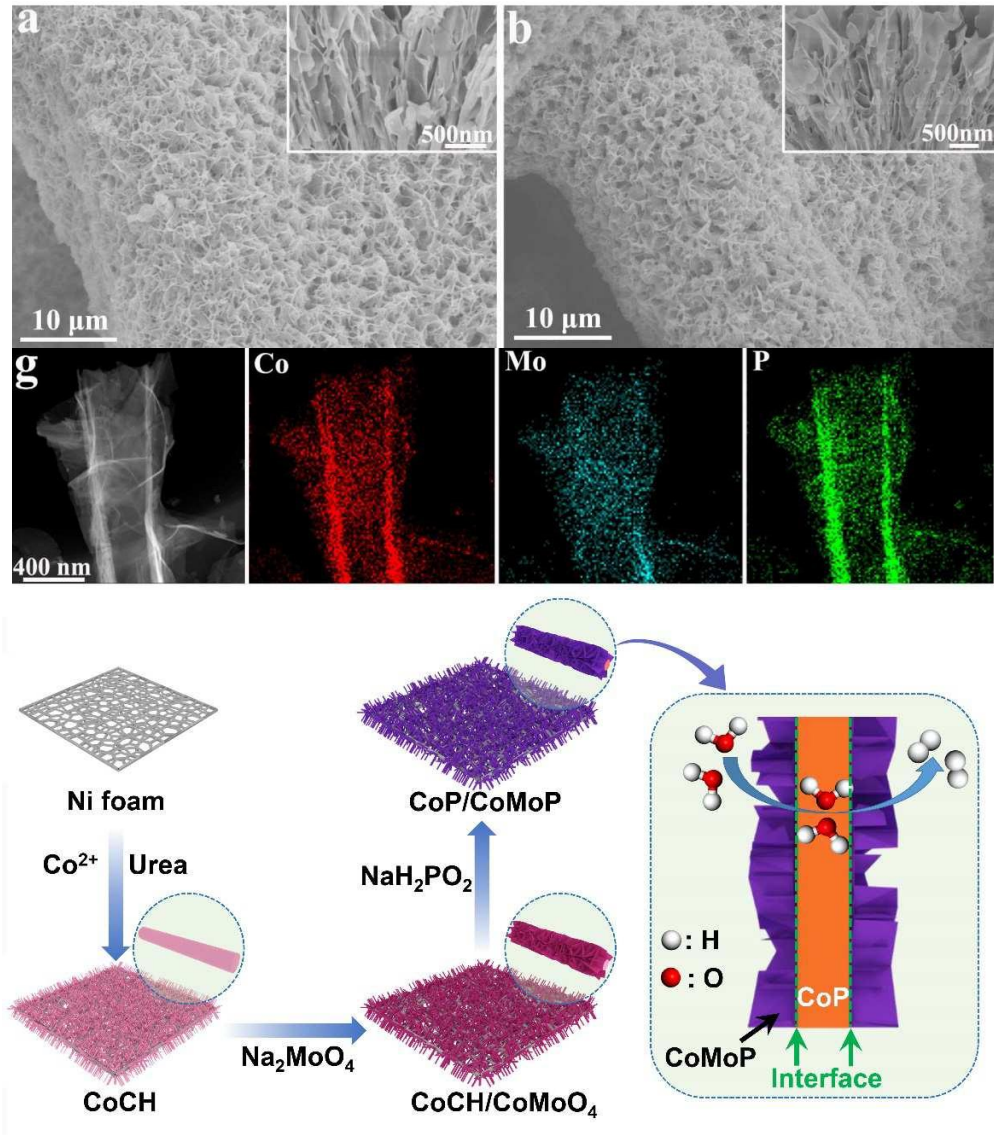

Figure 1. 11 The schematic diagram to illustrate the fabrication process of CoP/CoMoP via topotactic conversion from CoCH [58].

Unlike nitrogen, phosphorus has a much larger atomic radius than carbon, and its incorporation therefore induces pronounced lattice distortion together with substantial electronic redistribution within the carbon framework. The main phosphorus configurations in doped carbon materials can be classified as C_3P, C_3PO, C_2PO_2, CPO_3, and C-O-P species, as schematically illustrated in Figure X. Among these, the C_3P configuration is thermodynamically unstable and readily undergoes oxidation, making it difficult to exist as an isolated species under practical conditions. The incorporation of C_3P causes significant out-of-plane (z-direction) distortion of the carbon lattice and effectively enlarges the interlayer spacing. Because phosphorus is less electronegative than carbon, electron density is

transferred from the surrounding carbon atoms towards the phosphorus center, whereas within the C-P bond itself, the electron density is polarized towards carbon. This asymmetric charge redistribution perturbs the local electronic environment and may optimize the GH adsorption characteristics of neighboring carbon sites (**Figure 1. 10**) [54].

Sergio García-Dalí et al. [55] employed Pluronic® F-127 as a crosslinking agent and phytate as a combined phosphorus and carbon source to prepare phosphorus-doped carbon materials. The presence of the crosslinker suppressed phosphorus volatilization during carbonization, enabling a phosphorus content above 7 wt.% to be retained even after treatment at 1000 °C. X-ray photoelectron spectroscopy was used to elucidate the temperature-dependent evolution of phosphorus-containing functional groups. At 500°C, the material mainly contained phosphodiester and pyrophosphate species, and the carbon framework remained poorly carbonized, forming predominantly amorphous microporous carbon. Upon heating to 700-800 °C, the carbon layers gradually densified, and the decomposition of phytic acid produced phosphoric acid that acted as a self-activating agent, generating microporosity within the carbon matrix. Simultaneously, P–O species were progressively converted into P-C bonds, which are regarded as the key active sites for the hydrogen evolution reaction. The concentration of P-C species reached a maximum at 900 °C, corresponding to the highest HER activity. Further heating to 1000 °C increased the degree of graphitization but also promoted the desorption of phosphorus species from the carbon framework, leading to a slight decline in catalytic performance. Ziwu Liu et al. [56] proposed that the progressive detachment of C_3PO structures from the carbon lattice at elevated temperatures generates a high density of defect sites. Raman spectroscopy supports this interpretation, as evidenced by the increase in the ID/IG ratio with increasing temperature, indicating an increasing defect concentration. By combining experimental observations with theoretical calculations, the authors concluded that these defect sites created by the removal of C_3PO species constitute the primary active centers for HER.

1.2.2.3 Dual-doped carbon catalyst

Qiao et al. designed various nitrogen-containing co-doped graphene-based materials and evaluated their HER activity through a combination of electrochemical testing and DFT calculations, revealing the HER activity trend of different nitrogen-containing co-doped carbon materials. Ito et al. [57] synthesized a series of graphene doped with heteroatoms and revealed that the differences in HER performance of graphene doped with heteroatoms are related to the doping number and configuration of heteroatoms.

1.3 The synthesis methods of carbon based catalyst

1.3.1 Wet chemical preparation technology

Wet chemical synthesis is a synthetic method in which a precursor is dissolved in a solvent to form a solution, and the desired compound target material is formed through reactions such as hydrolysis and polymerization in the liquid phase. The wet chemical synthesis method has the characteristics of low temperature, simplicity and controllability. The reactants are dispersed in the liquid phase in molecular or ionic form, and the reaction occurs at the homogeneous/heterogeneous interface.

1.3.1.1 Hydrothermal synthesis

The hydrothermal synthesis method mainly involves dissolving the product in an aqueous solution and transferring it to a hydrothermal synthesis reactor for reaction. After heating, the pressure inside the reaction vessel increases, and the water is in a subcritical or supercritical state, resulting in significant changes in its physical and chemical properties. The viscosity and surface tension of aqueous solutions under high temperature and high-pressure conditions are significantly reduced, resulting in a decrease in ion diffusion energy barriers and accelerated diffusion kinetics. This result will greatly increase the probability of reaction collisions per unit time, allowing the reaction to occur at lower temperatures. After the collision of reactants generates crystal nuclei, other reactants in the solution tend to deposit on the surface of the generated crystal nuclei. Affected by the concentration gradient in the solution, small crystal nuclei dissolve and migrate to the surface of large crystal nuclei, improving through the Oswald ripening process. The structure, size, and crystallinity of the final product can be controlled by adjusting the reaction parameters.

Xingkai Huang et al. [58] grew CoCH/$CoMoO_4$ precursors on the surface of foam nickel by hydrothermal synthesis method and then grew CoP/CoMoP heterostructures by CVD method. The CoP nanowires in the heterojunction were modified, and layered CoMoP nanosheets were grown on the outside, exhibiting a large specific surface area and excellent conductivity. The morphology, element distribution, and synthesis pathway of the sample are recorded in **Figure 1.11**. Combining DFT calculations, researchers found that CoP and CoMoP exhibit good synergistic effects through electron transfer.

1.3.1.2 Co-precipitation method

Coprecipitation is a classic preparation technology for wet synthesis of nanopowder materials. The core principle is to add precipitation agents (such as hydroxide, carbonate, oxalate, etc.) in the mixed solution containing two or more kinds of soluble metal salts, so that the metal ions in the solution can precipitate at the same time according to the preset proportion to form precursor precipitates with uniform composition. After washing, drying, calcination, and other subsequent processing, the target composite powder materials can be obtained. This method is easy to operate, cost-effective, and can accurately control the stoichiometric ratio of the product, effectively avoiding the problem of component segregation that is prone to occur in single precipitation methods. It is widely used in fields such as electrocatalysis. The key process parameters include solution pH value, reaction temperature, precipitation agent droplet acceleration rate, and aging time, which directly affect the particle size distribution, morphology, and final product properties of the precursor.

Zhaojie Wang et al. [59] synthesized $Co_2(PO_4)_3$-$8H_2O$ nanoflowers using cobalt nitrate and iron nitrate as reactants and sodium phosphate as precipitant. This reaction can only be carried out at room temperature, with mild synthesis conditions and very low cost. This catalyst exhibits good water electrolysis activity in alkaline electrolytes.

1.3.2 CVD method

Chemical vapor deposition (CVD) is a bottom-up synthesis method mainly used to synthesize high-quality two-dimensional thin film materials. The specific process of CVD method refers to introducing gaseous reactants into the reaction chamber, causing chemical reactions on the surface of the substrate.

According to different excitation methods, CVD can be divided into thermal CVD, plasma vapor CVD, and atomic layer deposition (ALD). The precursor, temperature, pressure, and growth substrate collectively will affect the growth process of two-dimensional materials. Among them, the type of precursor and temperature will affect the concentration distribution of reaction intermediates; The type of precursor and pressure changes can alter the supply rate of reactants; Temperature and pressure jointly affect the material and heat transfer rates during the reaction process; When using different growth substrates, it is necessary to choose the appropriate precursor type, growth temperature, and reaction pressure, and the growth rate on the surface of different growth substrates may vary.

1.3.2.1 Thermal CVD

In the process of growing two-dimensional thin film materials using thermal CVD, the composition and uniformity of reaction products can be controlled by changing the temperature and flow rate. Taking the growth of graphene as an example, temperature changes can significantly affect the diffusion rate of carbon atoms, thereby altering the concentration gradient of carbon atoms and ultimately affecting the nucleation process of graphene. The temperature has a more significant impact on the process of using solid precursors to produce transition metal compounds. Firstly, by changing the carbonization, the vapor pressures of solid precursors will be regulated, thereby altering the morphology and edge structure of transition metal compounds. In addition, high temperatures usually subject the nucleation process to thermodynamic control, leading to more stable multi-nucleation of multi-layer transition metal compounds.

Li Yadong et al. [60] used bulk metal as a metal source, followed by NH_3 etching strategy to successfully

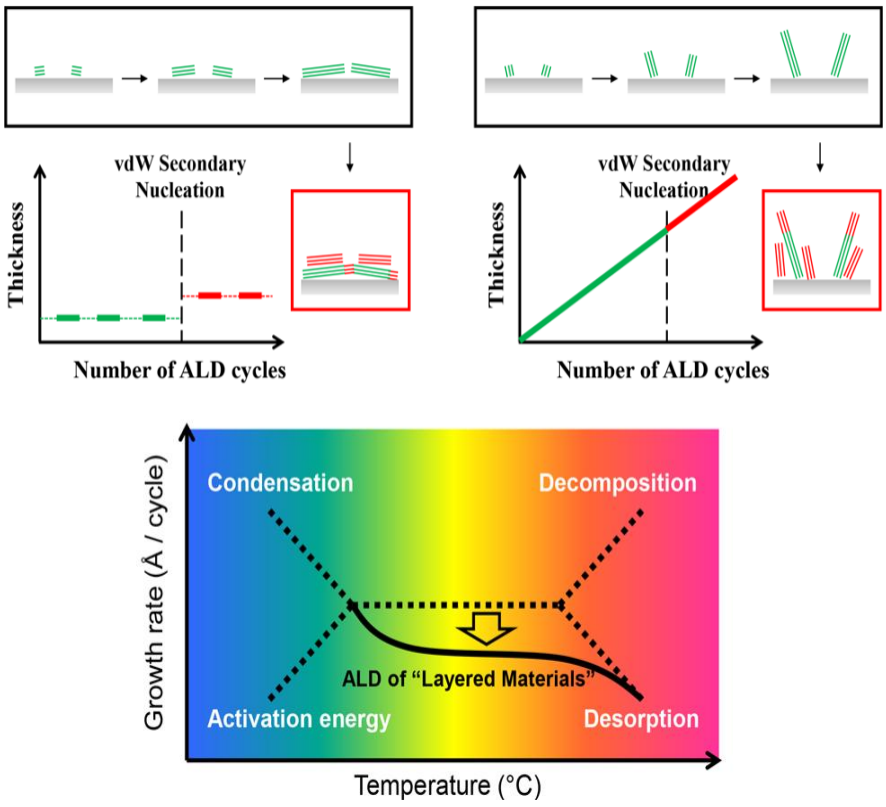

Figure 1. 12 Two distinctive growth modes of layered materials such as MoS_2 grown by ALD and the ALD window with four factors affecting the nonideality of ALD processes.

deposit metal atoms onto carbon support.

1.3.2.2 Atomic layer deposition technology (ALD)

Atomic layer deposition technology can be used to grow single-layer high-quality thin films. It is usually accompanied by two surface reactions. In the first reaction, precursor A undergoes chemical adsorption on the substrate surface, triggering a surface reaction between precursor A and the substrate. Subsequently, the first surface reaction is completed by blowing inert gas to remove by-products and unreacted precursor A. In the second reaction, precursor B will be introduced to have a reaction with the synthesized precursor A layer, followed by removing by-products and unreacted precursor B through a second round of inert gas blowing. These two surface reactions form an ALD cycle. By repeating several deposition reactions, any desired catalyst structures can be achieved. Due to the self-limiting reaction of each layer deposited on the basis of the previous layer, the deposited film is uniform and dense.

Thi Anh Ho et al. [60] used the ALD method to synthesize MoS_2 thin films as HER catalysts. The $MoCl_5$ and H_2S were used as precursors, and the products exhibited excellent electrocatalytic activity (**Figure 1. 12**).

1.3.3 Spatial confinement method

The spatial confinement strategy refers to the use of molecular-scale cages to restrict the migration of metal atoms, such as MOFs, COFs, and ion exchange resins, which have uniform and adjustable pore structures. Through physical adsorption or dual solvent methods, the target metal precursor will be uniformly encapsulated in the pore structure and finally anchored to the carbon substrate through pyrolysis treatment. The spatial confinement strategy retains the high activity of TMs species while inheriting the excellent mass transfer performance of porous carriers

1.3.3.1 MOFs-derived catalysts

MOFs are a type of crystal compound with a graded pore structure obtained by infinite extension of secondary units formed by organic long ligands and metal center bridging. Due to their rich pore size, uniform composition, large internal space, and desirable thermal stability, MOFs have attracted widespread attention from researchers in recent years. MOF-derived materials, therefore, are widely used in the field of electrocatalysis. For example, high surface area porous carbon materials can be obtained by carbonizing MOF materials at high temperatures, while metal centers remaining inside the framework can form oxides, phosphides, and sulfides. Organic components can prevent the aggregation of transition metal components during carbonization decomposition, limit the growth of transition metal particles, and thus form highly dispersed transition metal nanoparticles.

1.3.3.2 COFs -derived catalysts

Covalent organic frameworks (COFs) are novel ordered porous materials constructed by reversible reactions of light elements such as C, H, O, N, and S through organic linkers in a thermodynamically stable state. Their structural units are connected by covalent bonds. Since the first boron-containing COFs were reported in 2005, they have attracted much attention due to their controllable chemical composition, regular pore structure, and excellent chemical stability, which cannot be achieved

simultaneously with other porous materials. By one-step pyrolysis of COFs materials, heteroatom doped carbon skeletons can be easily obtained, demonstrating significant potential in electrocatalysis.

1.4 Overview of this study

In summary, the intrinsic HER activity of most carbon-based catalysts remains significantly lower than that of platinum. To address this limitation, two main strategies have been explored in this essay: morphological engineering and electronic structure modulation. Structural design aims to increase the density and accessibility of active sites, thereby enhancing the number of reactions per unit time. Electronic regulation, on the other hand, focuses on optimizing the intrinsic activity of active sites by tuning their electronic properties, improving intermediate adsorption energies, and thus lowering kinetic barriers. Specifically, I have synthesized transition-metal/hetero-atom-doped carbon and metal-free carbon with special morphology for HER.

Chapters 3 to 5 developed morphological control strategies for synthesizing transition metal-based carbon materials, aimed at limiting the migration kinetics of metal species at high temperatures. In Chapter 3, carbon coating and alloy reduction modification were simultaneously applied to layered double hydroxide (LDH) materials through chemical vapor deposition (CVD) technology, significantly improving the conductivity of the catalyst. Meanwhile, the layered structural characteristics of LDHs precursors are preserved. In addition, the chemical etching effect of different molybdenum source reagents on LDHs precursors was systematically studied. In Chapter 4, the chelation effect of phytic acid on transition metal elements was used to effectively limit the aggregation of CoP particles in the product. The size of CoP particles in the prepared product is only 25 nm, demonstrating excellent HER activity. In Chapter 5, CoP nanoparticles with an average particle size of 19nm were successfully anchored on a carbon substrate through the spatial confinement effect of ion exchange resin and the molecular bridging effect of phytic acid. This catalyst exhibits comparable performance to Pt-based catalysts, while significantly reducing preparation costs. In addition, we systematically studied the migration mechanism of S atoms after the decomposition of sulfonic acid groups and explored the feasibility of using SO_2 as a doping sulfur source.

In Chapters 6 and 7, ultra-thin carbon nanosheets with high specific surface area were developed. I also studied the synergistic enhancement mechanism of N and P dual-doped systems. In Chapter 6, ultra-thin heteroatom-doped carbon nanosheets were synthesized by precisely adjusting the precursor concentration and utilizing the self-activation effect of phytic acid to enhance the exposure of active sites. Subsequently, the precursor ratio and carbonization temperature were further optimized to obtain products with customized N and P doping types and content gradients. Through DFT calculations, the synergistic doping mechanism was elucidated, and a synergistic effect model of C_3PO and N dopants was finally constructed for the first time. In Chapter 7, I studied the influence of precursor types on N and P dopants in the final product. The conjugation between the imidazole ring and phytic acid hexagonal skeleton was utilized to increase the content of graphite nitrogen in the product. In addition, by protonating the imidazole ring with phosphate groups, the content of C_3PO structure in the product was increased. The prepared catalyst exhibits excellent HER activity.

Reference

[1] H. Li, M. Eddaoudi, M. O'Keeffe, O. M. Yaghi. Design and synthesis of an exceptionally stable and highly porous metal-organic framework. Nature, 1999, 402, 276–279.

[2] Dubouis N, Grimaud A. The hydrogen evolution reaction: from material to interfacial descriptors[J]. Chemical Science, 2019, 10(40): 9165-9181.

[3] A. E. Baumann, D. A. Burns, B. Liu, V. S. Thoi. Metal-organic framework functionalization and design strategies for advanced electrochemical energy storage devices. Commun Chem, 2019, 2, 86.

[4] Zeng M, Li Y. Recent advances in heterogeneous electrocatalysts for the hydrogen evolution reaction[J]. Journal of Materials Chemistry A, 2015, 3(29): 14942-14962.

[5] Zheng Y, Jiao Y, Jaroniec M, et al. Advancing the electrochemistry of the hydrogen‐evolution reaction through combining experiment and theory[J]. Angewandte Chemie International Edition, 2015, 54(1): 52-65.

[6] Wang H, Fu W, Yang X, et al. Recent advancements in heterostructured interface engineering for hydrogen evolution reaction electrocatalysis[J]. Journal of materials chemistry A, 2020, 8(15): 6926-6956.

[7] Olivares-Ramírez J M, Campos-Cornelio M L, Godínez J U, et al. Studies on the hydrogen evolution reaction on different stainless steels[J]. International Journal of Hydrogen Energy, 2007, 32(15): 3170-3173.

[8] Bender J T, Petersen A S, Østergaard F C, et al. Understanding cation effects on the hydrogen evolution reaction[J]. ACS Energy Letters, 2022, 8(1): 657-665.

[9] Li Y, Wang H, Xie L, et al. MoS2 nanoparticles grown on graphene: an advanced catalyst for the hydrogen evolution reaction[J]. Journal of the American Chemical Society, 2011, 133(19): 7296-7299.

[10] Wei J, Zhou M, Long A, et al. Heterostructured electrocatalysts for hydrogen evolution reaction under alkaline conditions[J]. Nano-micro letters, 2018, 10(4): 75.

[11] Cao X, Han Y, Gao C, et al. Highly catalytic active PtNiCu nanochains for hydrogen evolution reaction[J]. Nano Energy, 2014, 9: 301-308.

[12] Sheng W, Myint M N Z, Chen J G, et al. Correlating the hydrogen evolution reaction activity in alkaline electrolytes with the hydrogen binding energy on monometallic surfaces[J]. Energy & Environmental Science, 2013, 6(5): 1509-1512.

[13] Shi Y, Zhang B. Recent advances in transition metal phosphide nanomaterials: synthesis and applications in hydrogen evolution reaction[J]. Chemical Society Reviews, 2016, 45(6): 1529-1541.

[14] Ďurovič M, Hnát J, Bouzek K. Electrocatalysts for the hydrogen evolution reaction in alkaline and neutral media. A comparative review[J]. Journal of Power Sources, 2021, 493: 229708.

[15] Vesborg P C K, Seger B, Chorkendorff I B. Recent development in hydrogen evolution reaction catalysts and their practical implementation[J]. The journal of physical chemistry letters, 2015, 6(6): 951-957.

[16] Sun F, Tang Q, Jiang D. Theoretical advances in understanding and designing the active sites for hydrogen evolution reaction[J]. ACS Catalysis, 2022, 12(14): 8404-8433.

[17] Sun H, Yan Z, Liu F, et al. Self‐supported transition‐metal‐based electrocatalysts for hydrogen

and oxygen evolution[J]. Advanced materials, 2020, 32(3): 1806326.

[18] Kibsgaard J, Tsai C, Chan K, et al. Designing an improved transition metal phosphide catalyst for hydrogen evolution using experimental and theoretical trends[J]. Energy & Environmental Science, 2015, 8(10): 3022-3029.

[19] Saini R, Naaz F, Bashal A H, et al. Recent advances in nitrogen-doped graphene-based heterostructures and composites: mechanism and active sites for electrochemical ORR and HER[J]. Green Chemistry, 2024, 26(1): 57-102.

[20] Li S, Yu Z, Yang Y, et al. Nitrogen-doped truncated carbon nanotubes inserted into nitrogen-doped graphene nanosheets with a sandwich structure: a highly efficient metal-free catalyst for the HER[J]. Journal of Materials Chemistry A, 2017, 5(14): 6405-6410.

[21] Fung V, Hu G, Wu Z, et al. Descriptors for hydrogen evolution on single atom catalysts in nitrogen-doped graphene[J]. The Journal of Physical Chemistry C, 2020, 124(36): 19571-19578.

[22] Ye S, Luo F, Xu T, et al. Boosting the alkaline hydrogen evolution of Ru nanoclusters anchored on B/N–doped graphene by accelerating water dissociation[J]. Nano Energy, 2020, 68: 104301.

[23] Tian Y, Ye Y, Wang X, et al. Three-dimensional N-doped, plasma-etched graphene: Highly active metal-free catalyst for hydrogen evolution reaction[J]. Applied Catalysis A: General, 2017, 529: 127-133.

[24] Zhou S, Yang X, Pei W, et al. Heterostructures of MXenes and N-doped graphene as highly active bifunctional electrocatalysts[J]. Nanoscale, 2018, 10(23): 10876-10883.

[24] Zhou S, Yang X, Pei W, et al. Heterostructures of MXenes and N-doped graphene as highly active bifunctional electrocatalysts[J]. Nanoscale, 2018, 10(23): 10876-10883.

[25] H. Liu, M.-Q. Wang, Z.-Y. Chen, H. Chen, M.-W. Xu, S.-J. Bao. Design and synthesis of Co–N–C porous catalyst derived from metal organic complexes for highly effective ORR. *Dalton Trans.*, **2017**, *46*, 15646–15650.

[26] Y. Chen, R. Gokhale, A. Serov, K. Artyushkova, P. Atanassov. Novel highly active and selective Fe-N-C oxygen reduction electrocatalysts derived from in-situ polymerization pyrolysis. *Nano Energy*, **2017**, *38*, 201–209.

[27] C. Zhu, C. Kim, Y. Aoki, H. Habazaki. Nitrogen-Doped Hierarchical Porous Carbon Architecture Incorporated with Cobalt Nanoparticles and Carbon Nanotubes as Efficient Electrocatalyst for Oxygen Reduction Reaction. *Adv. Mater. Interfaces*, **2017**, *4*, 1700583.

[28] X.-F. Yang, A. Wang, B. Qiao, J. Li, J. Liu, T. Zhang. Single-Atom Catalysts: A New Frontier in Heterogeneous Catalysis. *Acc. Chem. Res.*, **2013**, *46*, 1740–1748.

[29] C. Tang, B. Wang, H. Wang, Q. Zhang. Defect Engineering toward Atomic Co–N_x–C in Hierarchical Graphene for Rechargeable Flexible Solid Zn-Air Batteries. *Adv. Mater.*, **2017**, *29*, 1703185.

[30] Y. Zhu, K. Miyake, Y. Shu, A. Gabe, Y. Hirota, Y. Uchida, S. Tanaka, E. Morallón, D. Cazorla-Amorós, N. Nishiyama. Anchoring a Co/2-methylimidazole complex on ion-exchange resin and its transformation to Co/N-doped carbon as an electrocatalyst for the ORR. *Catal. Sci. Technol.*, **2019**, *9*, 578–582.

[31] L. R. Arcot, M. Lundahl, O. J. Rojas, J. Laine. Asymmetric cellulose nanocrystals: thiolation of reducing end groups via NHS–EDC coupling. *Cellulose*, **2014**, *21*, 4209–4218.

[32] D. G. Castner, K. Hinds, D. W. Grainger. X-ray Photoelectron Spectroscopy Sulfur 2p Study of Organic Thiol and Disulfide Binding Interactions with Gold Surfaces. *Langmuir*, **1996**, *12*, 5083–

5086.

[33] P. Gobbo, M. C. Biesinger, M. S. Workentin. Facile synthesis of gold nanoparticle (AuNP)–carbon nanotube (CNT) hybrids through an interfacial Michael addition reaction. *Chem. Commun.*, **2013**, *49*, 2831.

[34] P. F. Siril, N. R. Shiju, D. R. Brown, K. Wilson. Optimising catalytic properties of supported sulfonic acid catalysts. *Applied Catalysis A: General*, **2009**, *364*, 95–100.

[35] M. Kim, D.-H. Nam, H.-Y. Park, C. Kwon, K. Eom, S. Yoo, J. Jang, H.-J. Kim, E. Cho, H. Kwon. Cobalt-carbon nanofibers as an efficient support-free catalyst for oxygen reduction reaction with a systematic study of active site formation. *J. Mater. Chem. A*, **2015**, *3*, 14284–14290.

[36] J. Jin, X. Fu, Q. Liu, J. Zhang. A highly active and stable electrocatalyst for the oxygen reduction reaction based on a graphene-supported g-C3N4@cobalt oxide core–shell hybrid in alkaline solution. *J. Mater. Chem. A*, **2013**, *1*, 10538–10545.

[37] X. Tong, X. Xia, C. Guo, Y. Zhang, J. Tu, H. J. Fan, X.-Y. Guo. Efficient oxygen reduction reaction using mesoporous Ni-doped Co_3O_4 nanowire array electrocatalysts. *J. Mater. Chem. A*, **2015**, *3*, 18372–18379.

[38] Han D, Cai J, Xie Y, et al. Constructing Complementary Catalytic Components on Co4N Nanowires to Achieve Efficient Hydrogen Evolution Catalysis[J]. Advanced Energy and Sustainability Research, 2022, 3(6): 2100219.

[39] G. Tao, L. Zhang, L. Chen, X. Cui, Z. Hua, M. Wang, J. Wang, Y. Chen, J. Shi. N-doped hierarchically macro/mesoporous carbon with excellent electrocatalytic activity and durability for oxygen reduction reaction. *Carbon*, **2015**, *86*, 108–117.

[40] X. Wang, J. Zhou, H. Fu, W. Li, X. Fan, G. Xin, J. Zheng, X. Li. MOF derived catalysts for electrochemical oxygen reduction. *J. Mater. Chem. A*, **2014**, *2*, 14064–14070.

[41] Song X, Deng C. Driving force induced transition in thermal behavior of grain boundary migration in Ni[J]. Physical Review Materials, 2023, 7(9): 093401.

[42] J. Quílez-Bermejo, C. González-Gaitán, E. Morallón, D. Cazorla-Amorós. Effect of carbonization conditions of polyaniline on its catalytic activity towards ORR. Some insights about the nature of the active sites. *Carbon*, **2017**, *119*, 62–71.

[43] Meng, Y.; Gu, D.; Zhang, F.; Shi, Y.; Cheng, L.; Feng, D.; Wu, Z.; Chen, Z.; Wan, Y.; Stein, A.; Zhao, D. A Family of Highly Ordered Mesoporous Polymer Resin and Carbon Structures from Organic−Organic Self-Assembly. *Chem. Mater.* **2006**, *18* (18), 4447–4464. https://doi.org/10.1021/cm060921u.

[44] Wang, T.; Sun, Y.; Wu, J.; Liu, X.; Pan, R.; Liu, X. Shape and Phase Controlled Synthesis of Mesostructured Carbon Single Crystals through Mesoscale Self-Assembly of Reactive Monomicelles and Their Unprecedented Exfoliation into Single-Layered Carbon Nanoribbons. *Journal of Colloid and Interface Science* **2020**, *558*, 32–37. https://doi.org/10.1016/j.jcis.2019.09.098.

[45] Wei, J.; Sun, Z.; Luo, W.; Li, Y.; Elzatahry, A. A.; Al-Enizi, A. M.; Deng, Y.; Zhao, D. New Insight into the Synthesis of Large-Pore Ordered Mesoporous Materials. *J. Am. Chem. Soc.* **2017**, *139* (5), 1706–1713. https://doi.org/10.1021/jacs.6b11411.

[46] G. Panomsuwan, N. Saito, T. Ishizaki. Electrocatalytic oxygen reduction activity of boron-doped carbon nanoparticles synthesized via solution plasma process. Electrochemistry Communications, 2015, 59, 81–85.

[47] Paraknowitsch, J. P.; Thomas, A. Doping Carbons beyond Nitrogen: An Overview of Advanced Heteroatom Doped Carbons with Boron, Sulphur and Phosphorus for Energy Applications. *Energy Environ. Sci.* **2013**, *6* (10), 2839. https://doi.org/10.1039/c3ee41444b.

[48] Li Y, Dong Z, Jiao L. Multifunctional transition metal‐based phosphides in energy‐related electrocatalysis[J]. Advanced Energy Materials, 2020, 10(11): 1902104.

[49] He H, Mai J H, Hu K S, et al. Recent advances in electrocatalysts for efficient hydrogen evolution reaction[J]. Rare Metals, 2025, 44(4): 2208-2238.

[50] Yao, F.; Ye, G.; Peng, W.; Zhao, G.; Wang, X.; Wang, Y.; Zhu, W.; Jiao, Y.; Huang, H.; Ye, D. Preparation of Activated Biochar with Adjustable Pore Structure by Hydrothermal Carbonization for Efficient Adsorption of VOCs and Its Practical Application Prospects. *Journal of Environmental Chemical Engineering* **2023**, *11* (2), 109611. https://doi.org/10.1016/j.jece.2023.109611.

[51] Tian Y, Ye Y, Wang X, et al. Three-dimensional N-doped, plasma-etched graphene: Highly active metal-free catalyst for hydrogen evolution reaction[J]. Applied Catalysis A: General, 2017, 529: 127-133.

[52] Estevez, L.; Barpaga, D.; Zheng, J.; Sabale, S.; Patel, R. L.; Zhang, J.-G.; McGrail, B. P.; Motkuri, R. K. Hierarchically Porous Carbon Materials for CO_2 Capture: The Role of Pore Structure. *Ind. Eng. Chem. Res.* **2018**, *57* (4), 1262–1268.

[53] Ding, Y.; Qi, J.; Hou, R.; Liu, B.; Yao, S.; Lang, J.; Chen, J.; Yang, B. Preparation of High-Performance Hierarchical Porous Activated Carbon via a Multistep Physical Activation Method for Supercapacitors. *Energy Fuels* **2022**, *36* (10), 5456–5464.

[54] Jin Q, Khandelwal M, Kim W. High-frequency supercapacitors with phosphorus-doped Ketjen black[J]. Journal of Energy Chemistry, 2023, 82: 464-474.

[55] Huang X, Xu X, Luan X, et al. CoP nanowires coupled with CoMoP nanosheets as a highly efficient cooperative catalyst for hydrogen evolution reaction[J]. Nano Energy, 2020, 68: 104332.

[56] Heidarinejad, Z.; Dehghani, M. H.; Heidari, M.; Javedan, G.; Ali, I.; Sillanpää, M. Methods for Preparation and Activation of Activated Carbon: A Review. *Environ Chem Lett* **2020**, *18* (2), 393–415.

[57] Conway, B. E. TECHNICAL PAPERS' ELECTROCHEMICAL SCIENCE AND TECHNOLOGY.

[58] Trasatti, S.; Buzzanca, G. Ruthenium Dioxide: A New Interesting Electrode Material. Solid State Structure and Electrochemical Behaviour. *Journal of Electroanalytical Chemistry and Interfacial Electrochemistry* **1971**, *29* (2), A1–A5.

[59] Rudge, A.; Davey, J.; Raistrick, I.; Gottesfeld, S.; Ferraris, J. P. Conducting Polymers as Active Materials in Electrochemical Capacitors. *Journal of Power Sources* **1994**, *47* (1–2), 89–107.

[60] Winter, M.; Brodd, R. J. What Are Batteries, Fuel Cells, and Supercapacitors? *Chem. Rev.* **2004**, *104* (10), 4245–4270.

Chapter 2

Experimental evaluation of the catalysts for the hydrogen evolution reaction

The reaction kinetics of the electrocatalytic hydrogen evolution reaction (HER) are closely related to the intrinsic activity of the catalyst, the electrode interface structure, and the electrolyte environment. In electrochemical evaluation systems, the three-electrode setup has become the standard testing platform for HER performance assessment due to its ability to precisely control and measure the electrochemical behavior of the working electrode. This chapter systematically elaborates on the testing principles, methods, and key evaluation parameters of HER performance based on the three-electrode system, providing an assessment framework for subsequent catalyst activity characterization and mechanistic analysis[1-5].

2.1 Construction and working principle of the three-electrode system

2.1.1 The composition of the three-electrode system

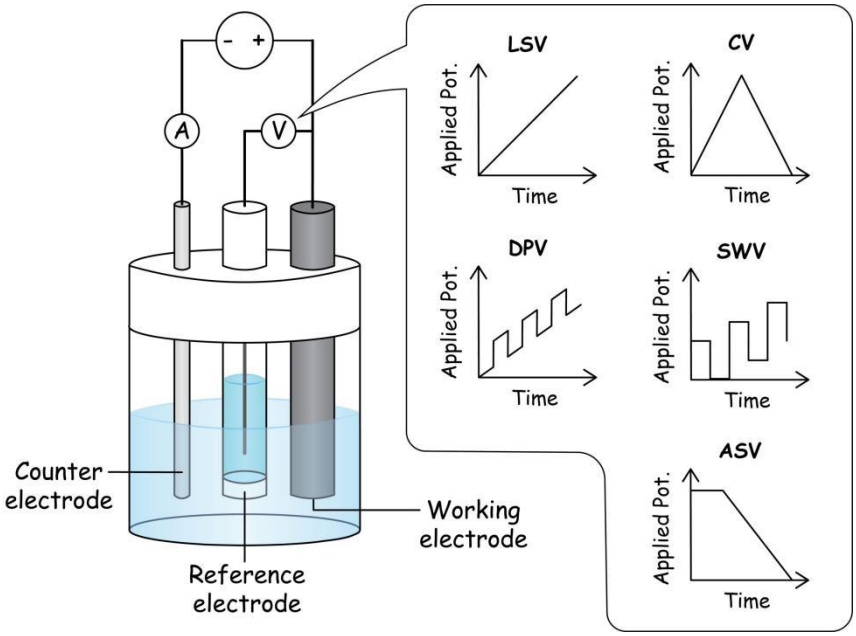

Figure 2. 1 The schematic illustration of three electrode cell system.

The three-electrode system consists of a working electrode (WE), a reference electrode (RE), and a counter electrode (CE), all immersed in an electrolyte solution. Electrochemical signals are applied and collected via a potentiostat, with a schematic diagram shown in **Figure 2.1**. The working electrode, which supports the catalyst and serves as the site for electrochemical reactions, can be made of materials such as glassy carbon electrodes, carbon cloth, or nickel mesh. The reference electrode provides a stable potential reference to eliminate the influence of ohmic drop in the solution, while the counter electrode

completes the current loop by conducting electrons to balance the redox reactions at the working electrode [6-9].

A potential is applied between the working electrode and the counter electrode via the potentiostat, while the potential difference between the working electrode and the reference electrode is monitored in real time. The reference electrode maintains a constant potential, accurately reflecting the actual potential of the working electrode. The counter electrode acts solely as an electron carrier and does not participate in the HER reaction. This system effectively separates the functions of potential control and current measurement, enabling precise regulation and characterization of the interfacial reactions at the working electrode.

2.1.2 Rotating disk electrode and rotating ring disk electrode[6-9]

In the performance characterization of the hydrogen evolution reaction (HER), the conventional three-electrode system only enables tests under static electrolyte conditions, making it difficult to accurately distinguish the effects of catalyst intrinsic activity and mass transfer processes on the reaction rate. The Rotating Disk Electrode (RDE) constructs a dynamic and quantifiable mass transfer environment through controllable electrode rotation speed, serving as a core tool for evaluating the kinetic parameters of HER catalysts[10-14].

The rotating disk electrode consists of three parts: electrode shaft, insulating sheath, and disk substrate, and its core structure is shown in **Figure 2.2**. The disk substrate is usually made of glassy carbon (with a diameter of 3 mm or 5 mm), and the catalyst to be tested is loaded on its surface; the electrode shaft is connected to the rotating device, which can precisely control the rotation speed (0–10000 r/min).

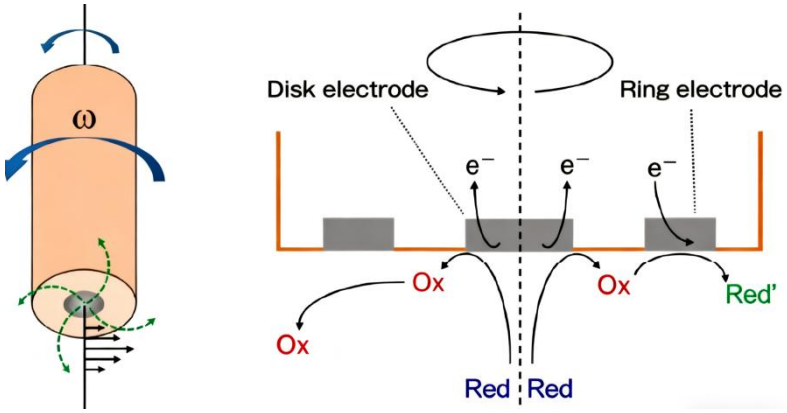

Figure 2. 2 The schematic illustration of rotating disk electrode

When the RDE rotates at a specific speed, it drives the surrounding electrolyte to form a radial flow field from the center of the disk to the edge. Reactants (H^+) are continuously transported to the electrode surface, while products (such as H_2 bubbles) are promptly stripped away. According to the Levich equation, the limiting diffusion current density has a linear relationship with the square root of the electrode rotation speed:

$$j_d = 0.62nFAD^{2/3}\nu^{-1/6}C_0\omega^{1/2}$$

where j_d is the limiting diffusion current density, n is the number of transferred electrons (n=2 for HER), F is the Faraday constant (96485 C·mol^{-1}), A is the geometric area of the electrode, D is the diffusion coefficient of the reactant, $\nu^{-1/6}$ is the kinematic viscosity of the electrolyte, C_0 is the bulk concentration of the reactant, and ω is the angular velocity of the electrode rotation ω =2\pi N/60, where N is the

rotation speed in r/min).

2.2 Measurements

2.2.1 Linear sweep voltammetry

Linear sweep voltammetry (LSV) is one of the basic potentiometric sweep methods; the potential of the working electrode is swept linearly, yielding a graph of current versus potential, called a voltammogram[15-19].

During an LSV measurement, the electrode potential E is varied linearly with time t according to:

$$E = E_i + vt$$

where E_i is the initial potential and v is the scan rate (in V s^{-1} or mV s^{-1}). When such a potential waveform is applied to the working electrode, oxidation or reduction of electroactive species generates a current response. The measured current i reflects contributions from electrode kinetics, mass transport, and double-layer charging[20-23]. LSV is a key tool for evaluating the performance of electrocatalysts for the HER, providing the following essential parameters:

(1) Overpotential (η)

Overpotential (η) is the extra potential beyond the thermodynamic equilibrium potential required to drive an electrochemical reaction at a measurable rate. It represents the kinetic barrier inherent to electrode processes and is one of the most critical parameters for evaluating electrocatalyst performance[24-26].

$$\eta = E_{\text{applied}} - E_{\text{eq}}$$

Where: E_{applied} represents experimentally applied electrode potential and E_{eq} is the thermodynamic equilibrium potential (Nernst potential) under given conditions.

(2) Tafel Slope

Obtained by linear fitting of η versus $\log |j|$ in the low-overpotential region of the LSV curve. The slope provides mechanistic insight into the rate-determining step (**Figure 2. 3**):

- ≈ 120 mV dec^{-1}: Volmer step (electrochemical adsorption) is rate-limiting;
- ≈ 40 mV dec^{-1}: Heyrovsky step (electrochemical desorption) is rate-limiting;

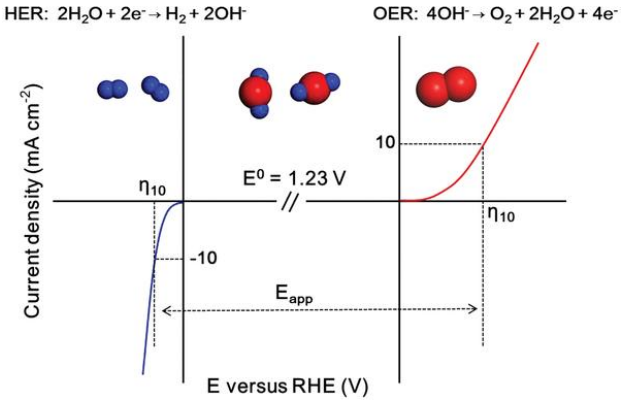

Figure 2. 3 The schematic illustration of Overpotential for HER and OER.

- ≈ 30 mV dec⁻¹: Tafel step (chemical desorption) is rate-limiting.

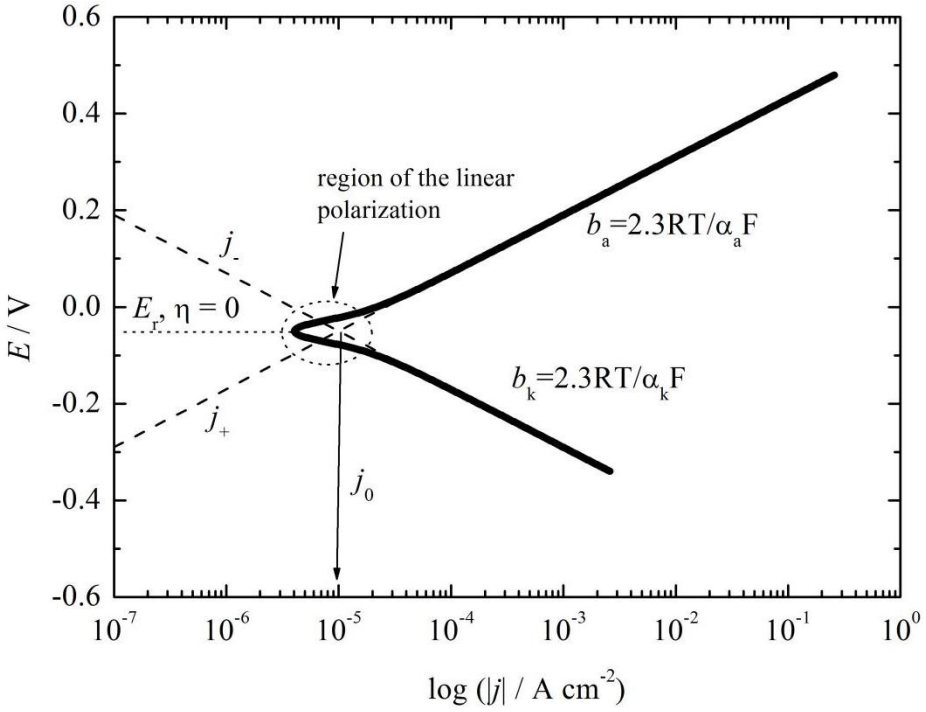

Figure 2. 4 The schematic illustration of $\boldsymbol{j_0}$.

For a single-electron transfer reaction under high overpotential (| η |>~ 50 mV), the current density (j) relates to the overpotential (η) through the Tafel equation:

$$\eta = a + b\log\ |\ j\ |$$

where:

- a is the Tafel intercept (related to the exchange current density j_0),
- b is the Tafel slope, given by:

$$b = \frac{2.303RT}{\alpha nF}$$

with:

- R: universal gas constant (8.314 J mol⁻¹ K⁻¹)
- T: absolute temperature (K)
- α: charge-transfer coefficient (typically 0.3–0.7)
- n: number of electrons transferred in the RDS
- F: Faraday constant (96485 C mol⁻¹)

At 298 K (25°C), this simplifies to:

$$b(\text{mV dec}^{-1}) \approx \frac{59.2}{\alpha n}$$

(3) Exchange Current Density ($\boldsymbol{j_0}$)

Exchange current density (j_0) represents the intrinsic rate of electron transfer at equilibrium—when the anodic and cathodic currents are equal and the net current is zero. It quantifies the inherent activity of an electrode material for a specific electrochemical reaction, independent of overpotential[27-30].

For a single-electron transfer reaction:

$$j = j_0 \left[\exp\left(\frac{\alpha F \eta}{RT}\right) - \exp\left(-\frac{(1-\alpha) F \eta}{RT}\right)\right]$$

At equilibrium ($\eta = 0$):

$$j_{\text{anodic}} = j_{\text{cathodic}} = j_0$$

2.2.2 Cyclic voltammetry

Cyclic voltammetry (CV) is a practical electrochemical technique that provides intuitive information on the redox potential, equilibrium constant, number of electrons related to electrode reactions, adsorption processes, etc. By comparing CV curves obtained from oxygen-saturated and inert gas-saturated solutions, the activity (e.g., reduction potential) of the catalyst can be determined. It is also possible to check whether the catalyst is stabilized or whether contamination of impurities in the aqueous solution has occurred before the measurement, using a known sample.

Since ORR is a solid-liquid interfacial reaction, maximizing the contact area of the two interfaces between the electrolyte and the catalyst surface is a prerequisite for improving the catalytic activity; thus, the argument of electrochemically active surface areas (ECSA) is significantly important for electrocatalysts. The ECSA can be calculated according to the measured double-layer capacitance (C_{dl}) by using CV measurements at different scan rates (v) in the non-Faradaic potential region.

$$C_{dl} = \frac{i_{dl}}{v}$$

$$ECSA = \frac{C_{dl}}{C_s}$$

where C_s is the specific capacitance value in the alkaline solution; the general value of C_s in 0.1 M KOH is 40×10^{-6} F cm $^{-2}$.

2.2.3 Turnover frequency

Turnover frequency (TOF) refers to the conversion of a catalyst per unit time and per unit active site. The quantity of reactants to a specific product reflects the inherent catalytic activity of a single active site of the catalyst, and is used to evaluate the catalyst. An important indicator of intrinsic activity. The larger the TOF value, the higher the intrinsic catalytic activity of the catalyst. The calculation formula is as follows:

$$TOF = \frac{jA}{zFn}$$

Among them, j is the current density, A is the geometric area of the electrode, z is the number of electron transfers required to generate product molecules, F is the Faraday constant, and n is the total number of catalytic active sites in the catalyst. At present, there is no accurate method to determine the total number of active sites in catalysts, so there is still a huge challenge in accurately calculating TOF. The total number of active sites can usually be calculated based on the mass and crystal structure of the

active substance in the catalyst, or using cyclic voltammetry. However, TOF can still serve as an important reference when comparing the intrinsic activity of different electrodes.

2.2.4 Electrochemical active area

Electrochemical active surface area (ECSA) refers to the effective active area of an electrode during the electrocatalytic reaction process, which can truly reflect the actual area of contact between the electrode material and the electrolyte. It is the most intuitive parameter to reflect the number of exposed active sites of the catalyst. The ECSA of the electrode is directly proportional to the electrochemical double-layer capacitance (Cdl) of the catalyst. The larger Cdl, the larger ECSA. The relationship between Δ j and scan rate obtained by testing cyclic voltammetry curves at different scan rates in the illegal Faraday region, where half of the linear fitting slope is Cdl, is calculated as follows:

$$ESCA = \frac{C_{dl}}{C_s \times ASA}$$

Among them, Cs is the specific capacitance, and ASA is the geometric area of the electrode. The current density can be normalized through ECSA, which can avoid the activity differences caused by differences in electrode ECSA. Therefore, the ECSA normalized current density is usually used to compare the intrinsic activity of catalysts.

2.2.5 Stability

Stability is another important indicator for measuring the electrochemical performance of catalysts, especially in industrial hydrogen production applications, which directly affects the device cost and service life of electrolytic cells. It can be evaluated through chronoamperometry, chronopotentiometry, or accelerated aging methods. The chronoamperometry (or potential) method is to record the trend of current (or potential) changes with reaction time under a constant voltage (or current). In long-term testing, the smaller the change, the better the stability of the catalyst. The accelerated aging method involves conducting thousands of cyclic voltammetry tests to compare the polarization curves before and after the test. The higher the coincidence, the better the cyclic stability of the catalyst[31-33].

Reference

[1] Hossain M N, Zhang L, Neagu R, et al. Exploring the properties, types, and performance of atomic site catalysts in electrochemical hydrogen evolution reactions[J]. Chemical Society Reviews, 2025.
[2] Meng W, Pang R, Li M, et al. Integrated catalyst‐substrate electrodes for electrochemical water splitting: a review on dimensional engineering strategy[J]. Small, 2025, 21(28): 2310469.
[3] Yang R, Yang L, Yong W, et al. Surface interrogation of advanced electrocatalysts by scanning electrochemical microscopy: fundamentals, progress and perspectives[J]. Chemical Science, 2025, 16(40): 18482-18495.
[4] Kousar N, Patil G, Kumbara A C, et al. Engineering of abundant metal complexes for electrochemical water splitting[J]. Dalton Transactions, 2025, 54(34): 12714-12736.
[5] Liu Y, Hu H, Wang K, et al. Advancing Seawater Electrolysis: NiFe‐LDH‐Based Electrocatalysts for the Oxygen Evolution Reaction[J]. Advanced Energy Materials, 2026, 16(5): e04101.
[6] Láng G G, Ujvári M, Kovács N, et al. The Theory and Applications of Dual Dynamic Voltammetry with Rotating Ring− Disk Electrodes[J]. ChemElectroChem, 2025, 12(9): e202400661.
[7] Khatun E, Ramona G, Sobota L, et al. Au-Ni Rotating Ring–Disk Electrode (RRDE) study: A new and rapid screening technique for quantitatively detecting aldehyde during electrochemical alcohol oxidation reaction[J]. Electrochimica Acta, 2025, 519: 145803.
[8] Ranaivoniriana A, Akouche A B, de Marbaix A D, et al. Upcycling old hard drives into polishing machines and rotating disk electrodes[J]. Journal of Solid State Electrochemistry, 2025, 29(6): 2419-2425.
[9] Mensharapov R M, Spasov D D, Sinyakov M V, et al. Carbon-Supported Pt-SiO2 Catalysts for Oxygen Reduction Reaction in Low-Temperature Range: Rotating Disk Electrode Study[J]. Hydrogen, 2025, 6(1): 5.
[10] Y. Garsany, O. A. Baturina, K. E. Swider-Lyons, S. S. Kocha. Experimental Methods for Quantifying the Activity of Platinum Electrocatalysts for the Oxygen Reduction Reaction. *Anal. Chem.*, 2010, *82*, 6321–6328.
[11] Z.-F. Huang, J. Wang, Y. Peng, C.-Y. Jung, A. Fisher, X. Wang. Design of Efficient Bifunctional Oxygen Reduction/Evolution Electrocatalyst: Recent Advances and Perspectives. *Advanced Energy Materials*, 2017, *7*, 1700544.
[12] R. Zhou, Y. Zheng, M. Jaroniec, S.-Z. Qiao. Determination of the Electron Transfer Number for the Oxygen Reduction Reaction: From Theory to Experiment. *ACS Catal.*, 2016, *6*, 4720–4728.
[13] O. El Mouahid, C. Coutanceau, E. M. Belgsir, P. Crouigneau, J. M. Léger, C. Lamy. Electrocatalytic reduction of dioxygen at macrocycle conducting polymer electrodes in acid media. *Journal of Electroanalytical Chemistry*, 1997, *426*, 117–123.
[14] W. Chen, Q. Xiang, T. Peng, C. Song, W. Shang, T. Deng, J. Wu. Reconsidering the Benchmarking Evaluation of Catalytic Activity in Oxygen Reduction Reaction. *iScience*, 2020, *23*, 101532.
[15] X. Ge, A. Sumboja, D. Wuu, T. An, B. Li, F. W. T. Goh, T. S. A. Hor, Y. Zong, Z. Liu. Oxygen Reduction in Alkaline Media: From Mechanisms to Recent Advances of Catalysts. *ACS Catal.*, 2015, *5*, 4643–4667.
[16] T. R. Garrick, T. E. Moylan, M. K. Carpenter, A. Kongkanand. Editors' Choice—Electrochemically Active Surface Area Measurement of Aged Pt Alloy Catalysts in PEM Fuel Cells by CO Stripping. *J. Electrochem. Soc.*, 2017, *164*, F55–F59.

N. Talukder, Y. Wang, B. B. Nunna, E. S. Lee. An In-Depth Exploration of the Electrochemical Oxygen Reduction Reaction (ORR) Phenomenon on Carbon-Based Catalysts in Alkaline and Acidic Mediums. *Catalysts*, 2022, *12*, 791.

[18] N. K. Bakirhan, B. Uslu, S. A. Ozkan. Sensitive and Selective Assay of Antimicrobials on Nanostructured Materials by Electrochemical Techniques, in *Nanostructures for Antimicrobial Therapy*, Elsevier, 2017, pp. 55–83.

[19] J. Wang. *Analytical Electrochemistry*, Wiley-VCH, New York, 2000.

[20] S. A. Özkan, B. Uslu, H. Y. Aboul-Enein. Analysis of Pharmaceuticals and Biological Fluids Using Modern Electroanalytical Techniques. *Critical Reviews in Analytical Chemistry*, 2003, *33*, 155–181.

[21] P. T. Kissinger, W. R. Heineman. Cyclic voltammetry. *J. Chem. Educ.*, 1983, *60*, 702.

[22] N.-T. Suen, S.-F. Hung, Q. Quan, N. Zhang, Y.-J. Xu, H. M. Chen. Electrocatalysis for the oxygen evolution reaction: recent development and future perspectives. *Chem. Soc. Rev.*, 2017, *46*, 337–365.

[23] Y. J. Kim, A. Lim, J. M. Kim, D. Lim, K. H. Chae, E. N. Cho, H. J. Han, K. U. Jeon, M. Kim, G. H. Lee, G. R. Lee, H. S. Ahn, H. S. Park, H. Kim, J. Y. Kim, Y. S. Jung. Highly efficient oxygen evolution reaction via facile bubble transport realized by three-dimensionally stack-printed catalysts. *Nat Commun*, 2020, *11*, 4921.

[24] M. J. Frisch, G. W. Trucks, H. B. Schlegel, G. E. Scuseria, M. A. Robb, J. R. Cheeseman, G. Scalmani, V. Barone, G. A. Petersson, H. Nakatsuji, X. Li, M. Caricato, A. V. Marenich, J. Bloino, B. G. Janesko, R. Gomperts, B. Mennucci, H. P. Hratchian, J. V. Ortiz, A. F. Izmaylov, J. L. Sonnenberg, Williams, F. Ding, F. Lipparini, F. Egidi, J. Goings, B. Peng, A. Petrone, T. Henderson, D. Ranasinghe, V. G. Zakrzewski, J. Gao, N. Rega, G. Zheng, W. Liang, M. Hada, M. Ehara, K. Toyota, R. Fukuda, J. Hasegawa, M. Ishida, T. Nakajima, Y. Honda, O. Kitao, H. Nakai, T. Vreven, K. Throssell, J. A. Montgomery Jr., J. E. Peralta, F. Ogliaro, M. J. Bearpark, J. J. Heyd, E. N. Brothers, K. N. Kudin, V. N. Staroverov, T. A. Keith, R. Kobayashi, J. Normand, K. Raghavachari, A. P. Rendell, J. C. Burant, S. S. Iyengar, J. Tomasi, M. Cossi, J. M. Millam, M. Klene, C. Adamo, R. Cammi, J. W. Ochterski, R. L. Martin, K. Morokuma, O. Farkas, J. B. Foresman, D. J. Fox. Gaussian 16 Rev. C.01. 2016.

[25] J. K. Nørskov, J. Rossmeisl, A. Logadottir, L. Lindqvist, J. R. Kitchin, T. Bligaard, H. Jónsson. Origin of the Overpotential for Oxygen Reduction at a Fuel-Cell Cathode. *J. Phys. Chem. B*, 2004, *108*, 17886–17892.

[26] R. Ma, G. Lin, Y. Zhou, Q. Liu, T. Zhang, G. Shan, M. Yang, J. Wang. A review of oxygen reduction mechanisms for metal-free carbon-based electrocatalysts. *npj Comput Mater*, 2019, *5*, 78.

[27] D. Deng, L. Yu, X. Pan, S. Wang, X. Chen, P. Hu, L. Sun, X. Bao. Size effect of graphene on electrocatalytic activation of oxygen. *Chem. Commun.*, 2011, *47*, 10016.

[28] J. Rossmeisl, Z.-W. Qu, H. Zhu, G.-J. Kroes, J. K. Nørskov. Electrolysis of water on oxide surfaces. *Journal of Electroanalytical Chemistry*, 2007, *607*, 83–89.

[29] M. Li, L. Zhang, Q. Xu, J. Niu, Z. Xia. N-doped graphene as catalysts for oxygen reduction and oxygen evolution reactions: Theoretical considerations. *Journal of Catalysis*, 2014, *314*, 66–72.

[30] F. Li, H. Shu, X. Liu, Z. Shi, P. Liang, X. Chen. Electrocatalytic Activity and Design Principles of Heteroatom-Doped Graphene Catalysts for Oxygen-Reduction Reaction. *J. Phys. Chem. C*, 2017, *121*, 14434–14442.

[31] P. W. Atkins, P. W. Atkins, J. De Paula. *Atkins' Physical Chemistry*, Oxford University Press, Oxford ; New York, 2002.

[32] I. C. Man, H.-Y. Su, F. Calle-Vallejo, H. A. Hansen, J. I. Martínez, N. G. Inoglu, J. Kitchin, T. F. Jaramillo, J. K. Nørskov, J. Rossmeisl. Universality in Oxygen Evolution Electrocatalysis on Oxide Surfaces. *ChemCatChem*, 2011, *3*, 1159–1165.
[33] X. Ao, W. Zhang, Z. Li, L. Lv, Y. Ruan, H.-H. Wu, W.-H. Chiang, C. Wang, M. Liu, X. C. Zeng. Unraveling the high-activity nature of Fe–N–C electrocatalysts for the oxygen reduction reaction: the extraordinary synergy between Fe–N_4 and Fe_4N. *J. Mater. Chem. A*, 2019, *7*, 11792–11801.

Chapter 3

Fabrication of carbon-coated hierarchical Mo doped NiCo alloying catalyst for hydrogen evolution reaction

Layered double hydroxides (LDHs) are two-dimensional layered materials composed of positively charged metal hydroxide layers and interlayer exchangeable anions. Owing to their large specific surface area, exchangeable interlayer anions, tunable active sites, and controllable morphology, they demonstrate considerable potential in the field of electrocatalysis. Consequently, this chapter primarily addresses methods for modifying LDHs to enhance their HER catalytic activity, which including: (1) The phosphorylation of LDHs via chemical vapor deposition (CVD) to regulate the hydrogen adsorption free energy($\triangle G_{H^*}$) of active sites. (2) Adopting CVD method for carbon coating to enhance the conductivity of LDHs, thereby accelerating charge transfer rates. (3) Employing MoO_4^{2-} chemical etching to increase the specific surface area of LDHs.

3.1 Introduction

The overuse of fossil fuels has caused severe environmental damage, accelerating the need for renewable energy sources. Hydrogen energy is a promising candidate due to its high energy density and clean combustion. Among all of the hydrogen-producing strategies, water splitting is truly carbon-free. However, its practical implementation is hindered by a high energy barrier that has challenged researchers for decades. Hydrogen evolution reaction (HER), one of the half reactions for water splitting, determines the overall water splitting efficiency. Currently, platinum-based catalysts are the most effective for HER, but their high cost and scarcity limit their applications. Therefore, developing affordable alternatives with comparable performance is critical [1-6].

Transition metal species (TMs) exhibit similar d-band structures compared to Pt-based catalysts. According to d-band center theory, TMs hold significant potential as HER catalysts. However, these materials possess several drawbacks that limit their application in electrocatalysis. tend to agglomerate at high temperatures, resulting in active site coverage and a subsequent decline in catalytic performance [7-12]. Secondly, the ΔG_{H^*} of transition metal species is insufficiently mild, necessitating combination with non-metallic elements to form transition metal compounds with optimized ΔG_{H^*}. To solve the above problems, special morphology design and electronic state design is required to ensure a large specific surface area and suitable ΔG_{H^*}.

Layered double hydroxides (LDHs) are two-dimensional layered materials composed of positively charged metal hydroxide layers and interlayer exchangeable anions [13-19]. They have attracted considerable research attention due to their large specific surface area, exchangeable interlayer anions, tunable active sites, and controllable morphology. Chen et al. constructed NiMo-LDH nanoflower

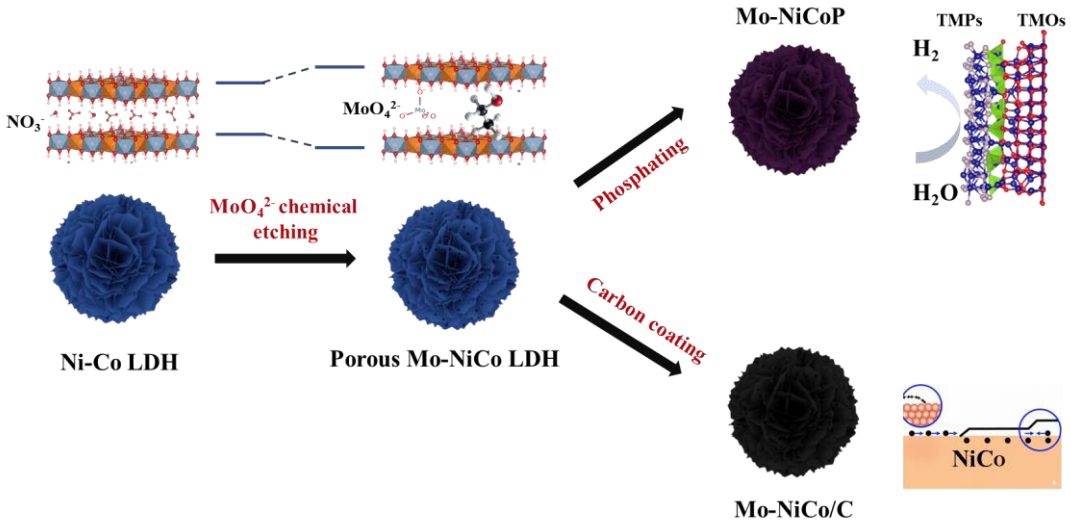

Scheme 3. 1 Schematic diagram of sample preparation.

structures for supercapacitors. This architecture exhibited an exceptionally high specific surface area, achieving a capacitance of 1482.2 F g^{-1} at 1 A g^{-1} alongside excellent stability. Consequently, based on these findings, we conclude that LDHs represent an excellent precursor for synthesizing catalysts with specialised structures. However, the poor conductivity of LDHs impedes rapid Volmer reactions, resulting in sluggish mass transfer kinetics. Furthermore, LDH structures lack a mild ΔG_{H^*}, necessitating additional steps to optimize this parameter [20-25].

Carbon coating represents an effective strategy for enhancing the conductivity of transition metal-based catalysts. Current efficient methods for synthesizing transition metal/carbon composite materials include chemical vapor deposition (CVD), in situ pyrolysis, and hydrothermal synthesis. Among these, CVD-based carbon coating allows precise control over the thickness and uniformity of the carbon layer, attracting significant attention from researchers. For optimizing the ΔG_{H^*} of transition metal catalysts, the phosphorylation step can effectively achieve the objective. Among all phosphorylation strategies, employing chemical vapor deposition (CVD) phosphorylation enables precise control over the thickness and compactness of transition metal phosphide films, providing valuable insights for material structural design [26-38].

Based on this, by optimizing preparation conditions, we successfully synthesized Mo-NiCoP and Mo-NiCo@C three-dimensional hierarchical nano-flower structures using porous nanosheets as a precursor with an LDHs structure. The synthetic schematic is presented in **Scheme 3. 2**. Specifically, I first employed a hydrothermal synthesis method to prepare the NiCo LDH precursor. Subsequently, using chemical vapor deposition (CVD), we investigated the modifying effects of phosphorylation and carbonization steps on the LDHs structure, applying the final products to the HER field. To increase the specific surface area of the LDHs, we exchanged MoO_4^{2-} into the interlayer space, thereby expanding the interlayer spacing [39-50]. Moreover, owing to the chemical etching effect of MoO_4^{2-}, the NiCo LDH surface exhibited abundant mesoporous structures, enabling full exposure of active sites. Notably, the intercalated MoO_4^{2-} could further be doped into NiCo during subsequent thermal treatment, thereby modulating the ΔG_{H^*} of the NiCo alloy. The incorporation of molybdenum ions not only increases the material's specific surface area but also generates a synergistic catalytic effect, significantly enhancing hydrogen evolution reaction (HER) activity.

3.2 Experiment

3.2.1The synthesize of Ni-Co precursors, Na_2MoO_4NiCo and $MoCl_5$NiCo.

The flower-like Ni-Co LDHs layered double hydroxides were synthesized via a solvothermal method. Typically, 1.5 mmol of $Ni(NO_3)_2{\cdot}6H_2O$, 1.5 mmol of $Co(NO_3)_2{\cdot}6H_2O$, and 6 mmol of urea were dissolved in 30 mL of ethanol, followed by 30min stirring process to form a homogeneous solution. The solution was then transferred into a 40 mL stainless steel autoclave for 120°C solvothermal process. After 10h, the resulting precipitate was collected by centrifugation and washed with water three times. After drying for a whole night, the Ni-Co precursors have been synthesized.

To investigate the effect of Mo doping on the HER performance of the products, we studied samples doped with different Mo sources, following the synthesis route outlined below. Typically, 1.5 mmol of $Ni(NO_3)_2{\cdot}6H_2O$, 1.5 mmol of $Co(NO_3)_2{\cdot}6H_2O$, Mo source (Na_2MoO_4 and $MoCl_5$) with a mass equal to half of the total mass of Ni and Co starting materials and 6 mmol of urea were dissolved in 30 mL of ethanol followed by 30min stirring process to form a homogeneous solution. The solution was then transferred into a 40 mL stainless steel autoclave for 120°C solvothermal process. After 10h, the resulting precipitate was collected by centrifugation and washed with water three times. After drying for a whole night, the Mo-doped precursors have been synthesized. They are named as Na_2MoO_4NiCo and $MoCl_5$NiCo.

3.2.2 The synthesize of Na_2MoO_4@NiCo and $MoCl_5$@NiCo.

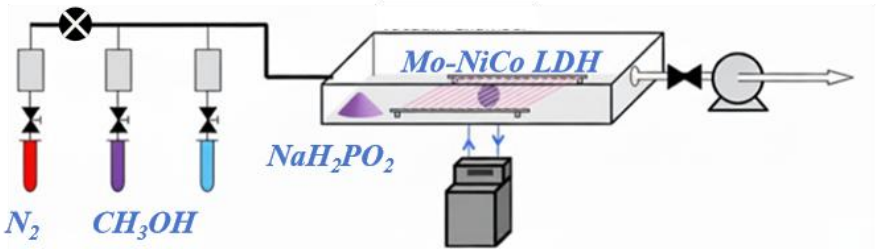

Scheme 3.2 The diagram of the CVD device.

0.2 g of the dried Ni-Co precursor was dissolved in 30 ml of deionized water with 20 min of stirring to obtain a green suspension. 0.1 g Na_2MoO_4 and corresponding urea (according to the molar ratio of 1:2) were dissolved in the above suspension. Then, the mixture was transferred to a sealed Teflon-lined 40 mL stainless steel autoclave for further reaction. After heating at 120 °C for 10 h, the precipitates were collected by centrifugal separation, and then washed with water three times and dried. The sample is noted as Na_2MoO_4@NiCo. In order to investigate the effect of the Mo source on sample performance, we also use $MoCl_5$ as the Mo source. The sample is noted as $MoCl_5$@NiCo (**Scheme 3.2**).

3.2.3 The synthesize of NiCo@C, Na_2MoO_4@NiCo@C, $MoCl_5$@NiCo@C and Mo-NiCoP

The prepared Na_2MoO_4@NiCo, $MoCl_5$@NiCo and Ni-Co precursors were heated to 350 °C under N_2 atmosphere with a heating rate of 2.5 °C/min. Methanol was used as C source and it is bubbled with N_2 for 3h deposition process. The samples are noted as Na_2MoO_4@NiCo@C, $MoCl_5$@NiCo@C and NiCo@C.

As for the typical preparation of Mo-NiCoP, the as-made Ni-Co (0.2 g) precursor was located in the downstream side of a quartz tube with NaH_2PO_2 (2.0 g) at the upstream side. The sample was subsequently heated to 350 °C with a rate of 2 °C min^{-1} and kept for 3 h under a N_2 atmosphere. The specific CVD device is illustrated in **Scheme 3.2**.

3.2.4 Characterization

The examination of morphology and particle dimensions was conducted through the utilization of transmission electron microscopy (TEM, Hitachi H800). The mass ratio of different elements was analyzed via energy-dispersive X-ray spectroscopy (EDX). Powder X-ray diffraction (XRD, RINT2200 with Cu Kα radiation) was used to determine the crystal structures and compositional phases.

3.3 Results and discussion

3.3.1 Crystalline structure of Na_2MoO_4@NiCo@C and $MoCl_5$@NiCo@C

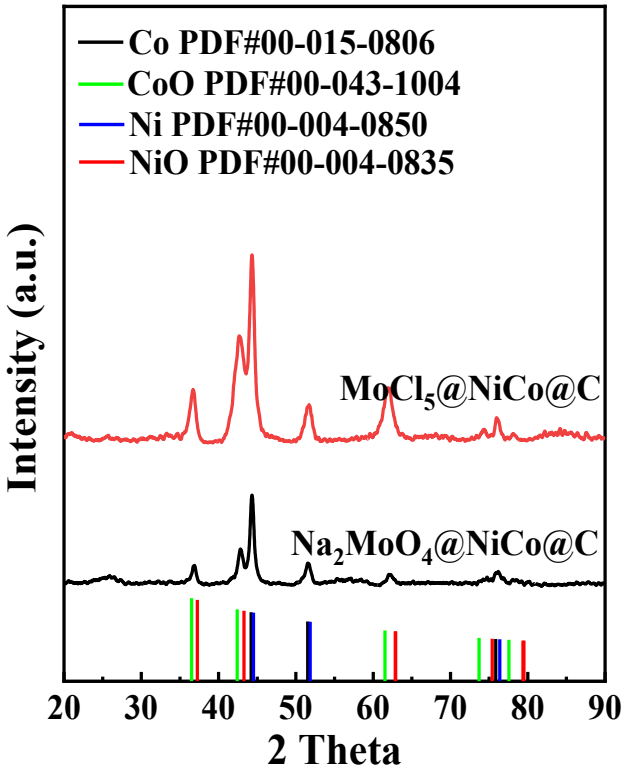

Figure 3. 1 The XRD patterns of Na_2MoO_4@NiCo and $MoCl_5$@NiCo.

The XRD patterns of Na_2MoO_4@NiCo and $MoCl_5$@NiCo is shown in **Figure 3.1.**, obvious diffraction peaks appeared at 37.2°, 43.2°, 62.9°and 75.4°, corresponding to (1 1 1), (2 0 0), (0 1 2), (2 2 0) and (3 1 1) planes, respectively, of phases of NiO. Besides, diffraction peaks also can be found at 36.7°, 42.6°, 61.7°and 73.8°, corresponding to (1 1 1), (2 0 0), (0 1 2), (2 2 0) and (3 1 1) planes of CoO. The formation of these two phases is due to the decomposition of the LDH structure at 350°C, resulting in the generation of transition metal oxides. The diffraction peaks appeared at 44.2°, 51.5°and 75.8° are corresponding to (0 1 1), (2 0 0) and (2 2 0) planes of Ni. The diffraction peaks appeared at 44.1°, 51.6°and 75.8° are corresponding to (0 1 1), (2 0 0) and (2 2 0) planes of Co[41-45]. The transition metal phase was formed through reduction by CO. Specifically, methanol was introduced into the CVD setup via a

bubbling method and decomposed into CO and H_2 at high temperatures. These gases came into contact with the transition metal oxides and rapidly reduced most of them to transition metal elements. Subsequently, CO underwent a disproportionation reaction on the surface of the transition metals, generating CO_2 and C atoms:

$$2CO \rightleftharpoons C+CO_2$$

The C atoms dissolved into the transition metal elements, precipitated upon reaching saturation, and formed a coating on the surface of the transition metals. Comparing the two samples, we observed that the content of transition metal oxide crystalline phases in the Na_2MoO_4@NiCo@C sample was significantly lower than that in $MoCl_5$@NiCo@C, indicating that the CO reduction effect was more effective on the Na_2MoO_4@NiCo@C sample.

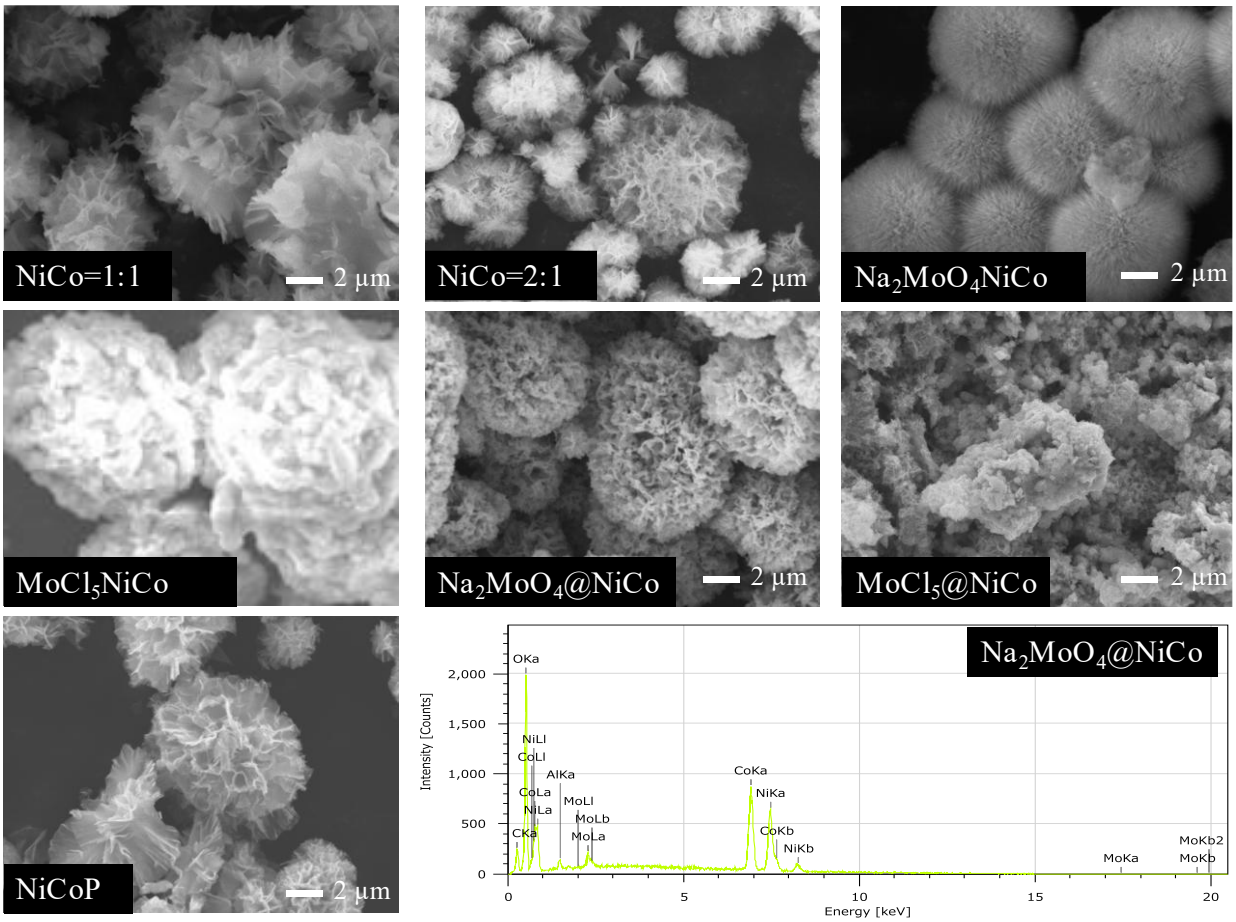

Figure 3. 2 SEM and EDX images of the various samples.

3.3.2 The investigation of samples' morphology by SEM testing

The microstructures and morphologies were observed using field emission scanning electron microscopy (SEM). **Figure 3.2** shows the SEM images of the as-prepared precursors. When the precursor ratio is 1:1, the sample revealed a flower-like microsphere structure composed of ultrathin nanosheets, with a size of 5 μm. It is found that the hierarchical flower-like Ni-Co layered double hydroxide nanostructures was sucessfully obtained. The ultrathin nanosheets are interconnected to each other to form an open hierarchical structure without stacking together. When the precursor ratio is 2:1, the size distribution of the flower-like structures in the product expands, ranging from 1 μm to 5 μm. This indicates that the concentration gradient inside the reaction vessel during hydrothermal

synthesis increases, intensifying the Ostwald ripening process. It is worth noting that after the addition of Na_2MoO_4 during the preparation of NiCo LDHs, the morphology transitions from flower-like to urchin-like. The flower-like structure of NiCo LDHs originates from the random and uniform growth of nanosheets along multiple crystal planes, whereas the MoO_4^{2-} anion selectively adsorbs onto high-surface-energy crystal planes of the NiCo LDHs, suppressing lateral growth along these planes while promoting one-dimensional radial growth perpendicular to the substrate. This directional difference in growth transforms the nanosheets from a "disordered interwoven floral cluster" into a "radially oriented needle/sheet-like aggregate extending from a central core," forming the characteristic spiny texture of an urchin. Furthermore, while the flower-like assembly of pure NiCo LDHs relies on van der Waals forces and electrostatic interactions between nanosheets, resulting in high interfacial energy and loose, irregular floral clusters, the introduction of Na_2MoO_4 allows MoO_4^{2-} to participate in balancing interlayer charges within the LDHs. This reduces the surface energy of the nanosheets, while electrostatic interactions between Na^+ and interlayer anions guide the nanosheets to assemble in a radially oriented manner centered around nucleation sites. This results in a more compact and regularly aligned structure, consistent with the dense radial features of an urchin-like morphology.

The addition of $MoCl_5$ during the preparation of NiCo LDHs leads to a morphological transformation into walnut-like structures, which is likely driven by the hydrolysis behavior of $MoCl_5$. As a salt of a strong acid and weak base, $MoCl_5$ undergoes stepwise hydrolysis in aqueous solution [46-50]:

$$MoCl_5 + H_2O \rightarrow MoOCl_3 + 2HCl$$

$$MoOCl_3 + H_2O \rightarrow MoO_2Cl + 2HCl$$

The hydrolysis continuously releases H^+, causing a rapid drop in the pH of the reaction system. The nucleation of NiCo LDHs typically requires a weakly alkaline environment. The lowered pH slows the hydrolysis and precipitation rates of metal ions, shifting the nucleation process from "rapid multi-core nucleation" to "slow single-core growth". As a result, the multi-core interwoven characteristic of the flower-like structure disappears, and particle aggregation occurs around individual cores, providing the structural basis for the walnut-like spherical clusters. Furthermore, MoO_x intermediates generated during hydrolysis induce local heterogeneous nucleation and stacking. Hydrolysis of $MoCl_5$ produces intermediates such as $MoOCl_3$ and MoO_2Cl, which further hydrolyze/oxidize to form MoO_x nanoparticles. These particles act as heterogeneous nucleation sites, adsorbing precursor ions of NiCo LDHs. Consequently, LDH nanosheets no longer grow freely but undergo irregular stacking around MoO_x particles. During stacking, the edges of the nanosheets press against and fuse with each other, forming clusters with uneven surfaces, ultimately resulting in the rough texture characteristic of walnut-like structures. Also, the release of Cl^- during hydrolysis etches the NiCo LDH nanosheets, fragmenting them from intact sheets into short rod-like structures and disrupting the sheet-based skeleton of the flower-like morphology. Additionally, Cl^- forms complexes with Ni^{2+}/Co^{2+}, reducing the coordination reactivity of the metal ions. This shifts the growth of LDHs from oriented sheet-like growth to random particle aggregation, ultimately leading to the tight clustering of nanoparticles into dense walnut-like aggregates. On contrast, when we prepare flower-like NiCo LDHs first, and then introduced Na_2MoO_4 for doping, we found a morphological transformation of the sample into a flower-like substrate with a mesoporous structure. This suggests that MoO_4^{2-} may undergo exchange with OH^- on the LDHs surface, dissolving local metal ions (Ni^{2+}/Co^{2+}) and creating nanoscale pores on the nanosheets. Since the etching occurs only at localized sites rather than across entire crystal planes, the

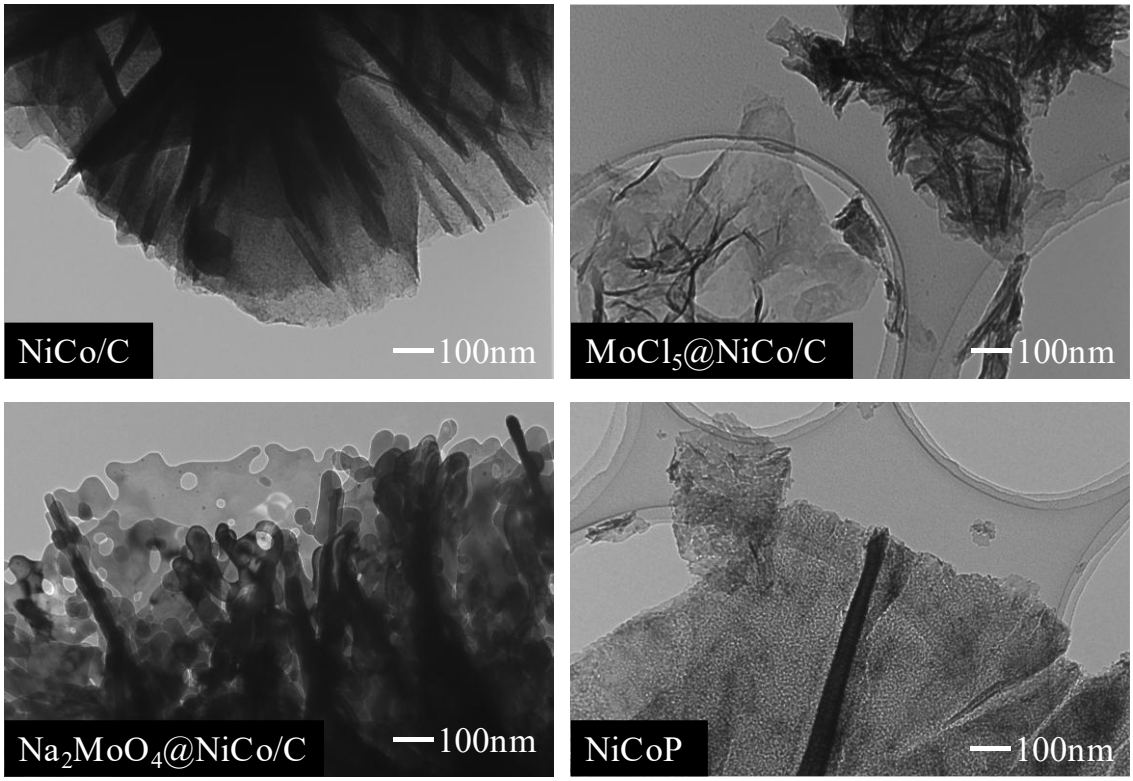

Figure 3. 3 TEM images of the various samples**.**

macroscopic flower-like framework is preserved, with mesoporous structures forming solely on the nanosheets. Additionally, during the post-doping process, MoO_4^{2-} can undergo ion exchange with anions such as NO_3^- and Cl^- in the interlayers of NiCo LDHs, entering the LDH interlayers. This process disrupts the charge balance of the original layered lattice, inducing local lattice contraction and reconstruction: in some regions, vacancies form due to ion migration and atomic rearrangement, and these vacancies interconnect to create mesopores. Furthermore, the larger volume of MoO_4^{2-} compared to the original interlayer anions expands the interlayer spacing, further enlarging the pore size and ultimately resulting in mesoporous characteristics. The presence of a mesoporous structure can effectively enhance the specific surface area of LDHs materials.

3.3.3 The HER activity measurements of the catalysts

The catalytic activity of samples was measured in 0.5 M H_2SO_4 at 1600 rpm on a carbon-like (GC) electrode. Graphite rods were used as counter electrodes in this measurement to prevent corrosion of the counter electrodes. The results of HER activity measurements for each sample are shown in **Figure 3.4**. Before carbon coating, all catalysts exhibited relatively low HER activity. At this stage, the Volmer reaction served as the rate-determining step, with slow charge transfer kinetics. After carbon coating, the performance of the catalysts improved significantly. Furthermore, we conducted a comparative analysis of the HER performance between NiCoP and NiCo catalysts. The phosphating process significantly enhanced the electronic structure of active sites, thereby improving HER activity. However, when compared to NiCo/C samples, despite NiCoP exhibiting a milder ΔG_{H^*}, the carbide-treated samples still demonstrated superior HER performance. This discrepancy can be attributed to the insufficient conductivity of NiCoP, which causes sluggish charge transfer kinetics, rendering the Volmer reaction as the rate-limiting step. Furthermore, Mo source etched samples showed superior HER activity over unetched counterparts. The $MoCl_5$ etched samples maintained higher activity than

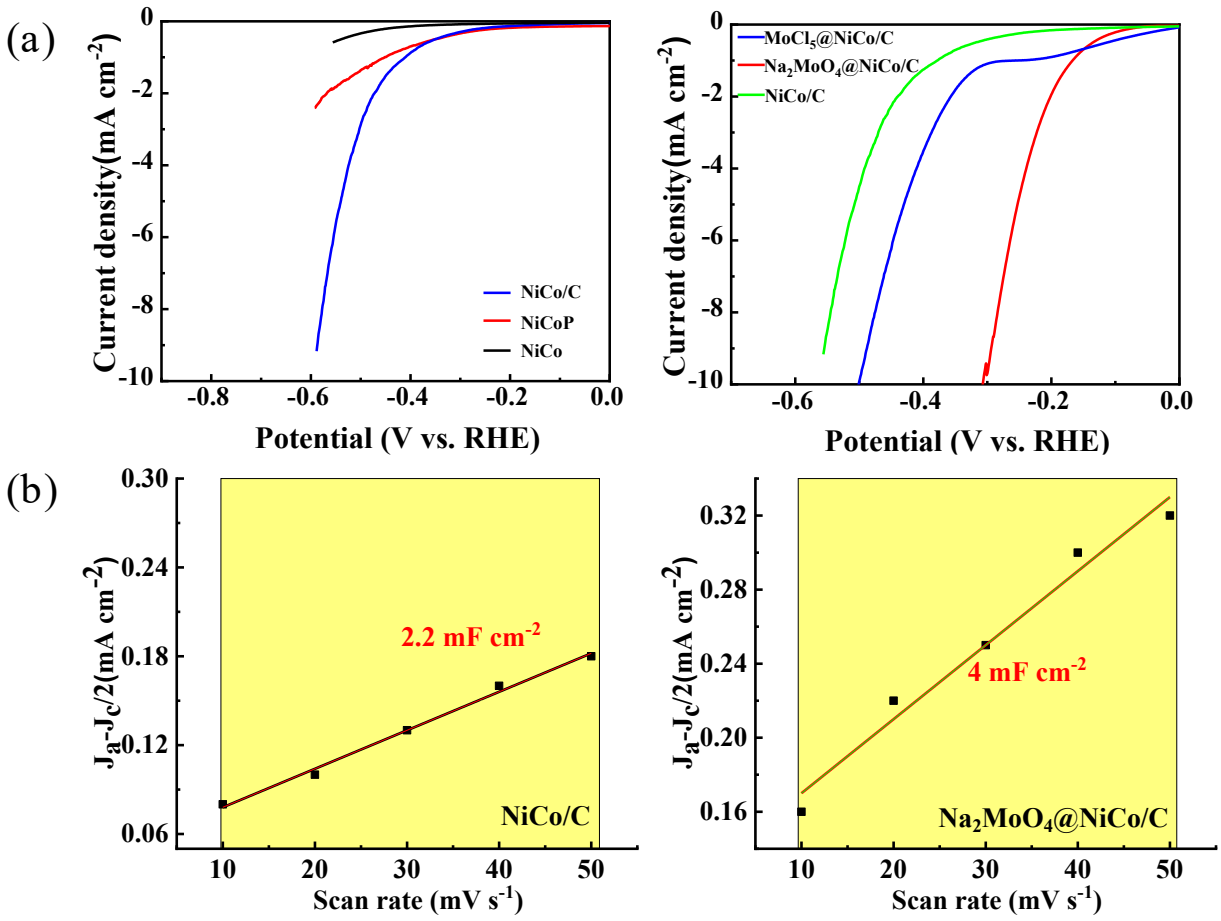

Figure 3. 4 HER catalytic activities of each sample.

NiCo/C despite structural disruption, which originates from the optimized electronic structure via Mo doping. Na_2MoO_4 etched samples achieved the highest HER activity among all samples, for the reason that this catalyst retained a floral morphology and uniform mesopores, suggesting an improved active surface area

3.4 Conclusion

A flower-like carbon-coated transition metal alloy catalyst prepared through a combined CVD and hydrothermal approach. Layered double hydroxides (LDHs) was used as precursors, which could offer high specific surface area, exchangeable interlayer anions, and tunable active sites. Carbon coating was applied to LDHs materials using the CVD method, while simultaneously reducing them into alloy, significantly enhancing the conductivity of the catalyst system. Additionally, MoO_4^{2-} ions were used to chemically etch the LDH precursors, increasing the active surface area of the catalyst.

Reference

[1] Bian J, Sun C. Platinum-based electrocatalysts: advances in synthesis, characterization, and challenges for energy conversion[J]. Journal of Physics: Condensed Matter, 2025, 37(31): 313002.

[2] Yang Q, Zeng J, Yang G, et al. Carbon-supported platinum-based electrocatalysts for alkaline hydrogen evolution[J]. EES Catalysis, 2025, 3(5): 972-993.

[3] Chen Y, Ding R, Li J, et al. Highly active atomically dispersed platinum-based electrocatalyst for hydrogen evolution reaction achieved by defect anchoring strategy[J]. Applied Catalysis B: Environmental, 2022, 301: 120830.

[4] Ali S M. Biomass derived carbon/platinum nanoparticles as electrocatalyst for the hydrogen evolution[J]. Scientific Reports, 2025, 15(1): 4602.

[5] Xu W, Zhang D, Wang T, et al. Non-platinum-based electrocatalysts for high performance acidic hydrogen evolution reactions in proton exchange membrane water electrolysis[J]. Applied Catalysis B: Environment and Energy, 2025, 361: 124626.

[6] Liu J, Ma X, Roh J, et al. Targeted construction of high-performance single-atom platinum-based electrocatalysts for hydrogen evolution reaction[J]. Chinese Journal of Catalysis, 2025, 69: 259-270.

[7] Ke S, Zhao Y, Min X, et al. Tailoring the d-band center in Pt-based catalysts for hydrogen evolution via transition metals incorporation[J]. International Journal of Hydrogen Energy, 2025, 105: 806-816.

[8] Nie Y, Uddin M, Wang Q, et al. Recent progress in Pt-based alloy catalysts: a comprehensive review on green synthesis and sustainable biomass hydrogenation applications[J]. Green Chemistry, 2025, 27(39): 12070-12106.

[9] Abbas F, Khan S N, Bibi S, et al. Exploring Single-Atom Catalysis for Hydrogen Evolution and Storage: A DFT Insight into First-Row Transition Metal-Porphyrin Complexes (Porph@ TMs)[J]. Gas Science and Engineering, 2025: 205646.

[10] Mu N, Hu Y, Bo T, et al. Enhanced ORR and HER performance of transition metal-doped SnS monolayers via strain engineering[J]. International Journal of Hydrogen Energy, 2026, 204: 153299.

[11] D. Higgins, P. Zamani, A. Yu, Z. Chen. The application of graphene and its composites in oxygen reduction electrocatalysis: a perspective and review of recent progress. Energy Environ. Sci., 2016, 9, 357–390.

[12] M. J. Allen, V. C. Tung, R. B. Kaner. Honeycomb Carbon: A Review of Graphene. Chem. Rev., 2010, 110, 132–145.

[13] Guo H, Tang Q, Hou D, et al. Kinetics and mechanism of anion exchange in layered double hydroxide nanoparticle[J]. Applied Clay Science, 2025, 266: 107694.

[14] Sherryna A, Zerga A Y, Zakaria Z Y, et al. Advances in the Morphological Design and Dimensional Approaches of Layered Double Hydroxides for Photocatalytic Applications: A Critical Review[J]. Energy & Fuels, 2025, 39(10): 4565-4609.

[15] Shang X, Hu J, Yan Y, et al. Deep insights into LDH reconstruction for enhanced capacitive deionization[J]. Journal of Environmental Chemical Engineering, 2025: 119593.

[16] M. D. Stoller, S. Park, Y. Zhu, J. An, R. S. Ruoff. Graphene-Based Ultracapacitors. Nano Lett., 2008, 8, 3498–3502.

[17] Karwasra R, Siwatch P, Gupta Y, et al. Recent advancements in layered double hydroxides as an

electrode material for high-performance asymmetric supercapacitors[J]. Journal of Solid State Electrochemistry, 2025: 1-31.

[18] Kainat F, Ilyas S, Jabeen N, et al. Advancements in Layered Double Hydroxide (LDH) Nanosheets: Preparation Techniques and Optoelectronic Applications[M]//Layered Nanomaterials for Solution-Processed Optoelectronics. CRC Press, 2025: 295-317.

[19] Tallal M, Ishaq T, Laraib S, et al. Recent modifications of layered double hydroxides for enhanced photocatalytic water splitting[J]. Journal of Materials Science, 2025: 1-30.

[20] J. Liang, Y. Jiao, M. Jaroniec, S. Z. Qiao. Sulfur and Nitrogen Dual-Doped Mesoporous Graphene Electrocatalyst for Oxygen Reduction with Synergistically Enhanced Performance. Angew. Chem. Int. Ed., 2012, 51, 11496–11500.

[21] K. M. Villemson, K. Kaare, R. Raudsepp, T. Käämbre, K. Šmits, P. Wang, A. V. Kuzmin, A. Šutka, B. A. Shainyan, I. Kruusenberg. Identification of Active Sites for Oxygen Reduction Reaction on Nitrogen- and Sulfur-Codoped Carbon Catalysts. J. Phys. Chem. C, 2019, 123, 16065–16074.

[22] R. Liu, C. von Malotki, L. Arnold, N. Koshino, H. Higashimura, M. Baumgarten, K. Müllen. Triangular Trinuclear Metal-N_4 Complexes with High Electrocatalytic Activity for Oxygen Reduction. J. Am. Chem. Soc., 2011, 133, 10372–10375.

[23] M. Quernheim, H. Liang, Q. Su, M. Baumgarten, N. Koshino, H. Higashimura, K. Müllen. Cobalt Phenanthroline-Indole Macrocycles as Highly Active Electrocatalysts for Oxygen Reduction. Chem. Eur. J., 2014, 20, 14178–14183.

[24] X. Fu, J.-Y. Choi, P. Zamani, G. Jiang, Md. A. Hoque, F. M. Hassan, Z. Chen. Co–N Decorated Hierarchically Porous Graphene Aerogel for Efficient Oxygen Reduction Reaction in Acid. ACS Appl. Mater. Interfaces, 2016, 8, 6488–6495.

[25] H. Liu, M.-Q. Wang, Z.-Y. Chen, H. Chen, M.-W. Xu, S.-J. Bao. Design and synthesis of Co–N–C porous catalyst derived from metal organic complexes for highly effective ORR. Dalton Trans., 2017, 46, 15646–15650.

[26] Y. Chen, R. Gokhale, A. Serov, K. Artyushkova, P. Atanassov. Novel highly active and selective Fe-N-C oxygen reduction electrocatalysts derived from in-situ polymerization pyrolysis. Nano Energy, 2017, 38, 201–209.

[27] C. Zhu, C. Kim, Y. Aoki, H. Habazaki. Nitrogen-Doped Hierarchical Porous Carbon Architecture Incorporated with Cobalt Nanoparticles and Carbon Nanotubes as Efficient Electrocatalyst for Oxygen Reduction Reaction. Adv. Mater. Interfaces, 2017, 4, 1700583.

[28] X.-F. Yang, A. Wang, B. Qiao, J. Li, J. Liu, T. Zhang. Single-Atom Catalysts: A New Frontier in Heterogeneous Catalysis. Acc. Chem. Res., 2013, 46, 1740–1748.

[29] C. Tang, B. Wang, H. Wang, Q. Zhang. Defect Engineering toward Atomic Co–Nx–C in Hierarchical Graphene for Rechargeable Flexible Solid Zn-Air Batteries. Adv. Mater., 2017, 29, 1703185.

[30] Alam M R, Gharami M, Dev B, et al. Next-generation materials for multifunctional applications: design progress and prospects of 2D MXene-enabled hybrid architectures[J]. Advanced Materials Interfaces, 2025, 12(6): 2400681.

[31] Jetti M, Vasimalla Y, Maloji S, et al. Emerging Role of 2D Nanomaterials in the Design and Development of Optical Sensors: Mechanisms, Architectures, and Applications[J]. IEEE Sensors Reviews, 2025.

[32] Jiang Z, Zhang S, Xu J, et al. Two-Dimensional Materials for Selective Ion Transport Membrane: Synthesis and Application Advances[J]. Colloids and Interfaces, 2025, 9(5): 63.

[33] Wang J, Yang G, Jiao Y, et al. Subtle 2D/2D MXene-based heterostructures for high-performance electrocatalytic water splitting[J]. Small Methods, 2025, 9(2): 2301602.

[34] Liu X, Li H, Zhang G, et al. Rational Design of Spherical Carbon Materials: Resolving Performance Trade-Offs in Electrochemical Energy Storage[J]. Small, 2026: e14440.

[35] Sharifirad A, Michel M, Roge V, et al. Strategies for enhancing the electrocatalytic performance of transition metal thin films deposited via chemical vapor process for hydrogen cells and electrolysers[J]. ChemElectroChem, 2025, 12(7): e202400609.

[36] Selvam R, Gengan S. Transition Metal Phosphides and Nitrides: Advanced Electrodeposition Strategies for Efficient Hydrogen Evolution-Review[J]. Topics in Catalysis, 2025: 1-24.

[37] Adeoye A E, Adeaga O A, Ukoba K. Chemical Vapour Deposition (CVD) and Physical Vapour Deposition (PVD) techniques: Advances in thin film solar cells[J]. Nigerian Journal of Technology, 2024, 43(3): 479-489.

[38] Ishaq M, Jabeen M, Haider R, et al. Geometric Design and Electronic Engineering of Transition Metal Phosphides for Key Electrochemical Energy Technologies: Nanoarchitectonics and Application[J]. Advanced Functional Materials, 2025: 2424141.

[39] Jing C, Huang L, Tao S, et al. Construction of MoB@ LDH heterojunction and its derivates through phase and interface engineering for advanced supercapacitor applications[J]. Journal of Colloid and Interface Science, 2024, 660: 10-20.

[40] Liao Z, He T, Shi L, et al. Selenium Oxoanions Removal from Wastewater by MoS_4^{2-} Intercalated FeMgAl LDH: Catalytic Roles of Fe and Mechanism Insights[J]. Catalysts, 2022, 12(12): 1592.

[41] Dong C, Guo M, Gao W, et al. Oriented interlayered charge transfer in NiCoFe layered double hydroxide/MoO3 stacked heterostructure promoting the oxygen-evolving behavior[J]. Journal of Colloid and Interface Science, 2022, 627: 891-899.

[42] Yang Q, Liu W, Wang X, et al. MoO_4^{2-}-LDH films for active protection of steel substrates by Electrodeposition–Hydrothermal method[J]. Applied Surface Science, 2024, 665: 160342.

[43] Zhou P, Ji Y, Zhang B, et al. Achieving both expanded interlayer spacing and anionic doping in NiCo-LDH as high performance supercapacitor electrode materials[J]. Materials Today Energy, 2025: 102138.

[44] Nagappan S, Karmakar A, Madhu R, et al. Tuning the active sites and optimizing the d-spacing value in CoFe-LDH by ex situ intercalation of guest anions: an innovative electrocatalyst for overall water splitting reaction[J]. Catalysis Science & Technology, 2023, 13(22): 6377-6391.

[45] Sun L, Liu Y, Luo B, et al. Hierarchical multiphase (Ni, Co)-Se with adjustable interlayer distance derived from reconstructed ZIF-L for enhanced hybrid-supercapacitors[J]. Chemical Engineering Journal, 2023, 454: 140088.

[46] Cheng Y, Wang X, Zhang D, et al. High-capacity binderless supercapacitor electrode obtained from sulfidation large interlayer spacing of NiMn-LDH[J]. Electrochimica Acta, 2022, 429: 141039.

[47] Wang D, Repo E, He F, et al. Dual functional sites strategies toward enhanced heavy metal remediation: Interlayer expanded Mg-Al layered double hydroxide by intercalation with L-cysteine[J]. Journal of Hazardous Materials, 2022, 439: 129693.

[48] Ge S, Zhao Q, Liu Y, et al. Ultrathin 2D–2D MXene-LDH Interlayer with High Polysulfide

Adsorption Ability for Advanced Li–S Batteries[J]. ACS Applied Materials & Interfaces, 2024, 16(38): 50650-50658.

[49] Wang X, Chang L, Zhao H, et al. Theoretical study on the swelling mechanism and structural stability of Ni_3Al-LDH based on molecular dynamics[J]. ACS omega, 2023, 8(3): 3286-3297.

[50] Lai C, Guo Z, Nie L, et al. Sulphur-and nitrogen-codoped layered double hydroxides with expanded interlayer distance for enhanced overall water splitting[J]. Journal of Electroanalytical Chemistry, 2023, 944: 117640.

Chapter 4

Facile and cost-effective synthesis of CoP anchored N doped carbon with high catalytic performance for electrochemical hydrogen evolution reaction

In Chapter 3, chemical vapor deposition (CVD) method was employed to synthesize transition metal phosphides (TMPs) and carbon-coated transition metal (TM) catalysts. However, this method has several drawbacks, including complex synthesis process, generation of dangerous PH_3 gases, and challenges in scaling up production. To overcome these problems, we developed a facile and eco-friendly strategy to synthesis carbon based TMPs catalyst. More specifically, we used phytic acid as both the phosphorus and carbon source, leveraging its potent metal-chelating capability to anchor cobalt species, thereby achieving the dispersion of nanoscale CoP on a carbon substrate. Furthermore, we utilised amino acids as the nitrogen source, which chelated with phytic acid to generate a three-dimensional carbon network, significantly increasing the specific surface area of the carbon substrate. Furthermore, NH_3 produced from amino acid pyrolysis and phosphoric acid from phytic acid pyrolysis enable self-etching of the carbon substrate. This process increases microporosity while successfully doping P and N atoms into the carbon network. The heteroatom-doped carbon substrate provides excellent conductivity for the integrated catalyst. Notably, phytic acid can be obtained from biomass at low cost, enabling economical large-scale synthesis. Crucially, the entire synthesis process avoids the generation of highly toxic PH_3 gas, ensuring a green and environmentally sound synthesis pathway.

4.1 Introduction

Hydrogen is widely accepted as a potential alternative to fossil fuels as a renewable and environmentally friendly energy carrier with high energy density. [1,2] Currently, the most commonly used strategy to produce hydrogen is natural gas cracking, which results in a certain amount of CO_2 emissions. Consequently, the production of green hydrogen is of great importance for meeting the ever-increasing demand for carbon neutrality. Water splitting provides a CO_2-free hydrogen production process with superb energy efficiency and ultrahigh purity products. [3–5] The hydrogen evolution reaction (HER) is a pivotal semi-reaction that determines the efficiency of water splitting. Indeed, the overpotential of the HER is extremely high, resulting in sluggish reaction kinetics. Accordingly, the manufacture of efficient and low-cost HER catalysts will be the heart of the matter in the long term [6–10].

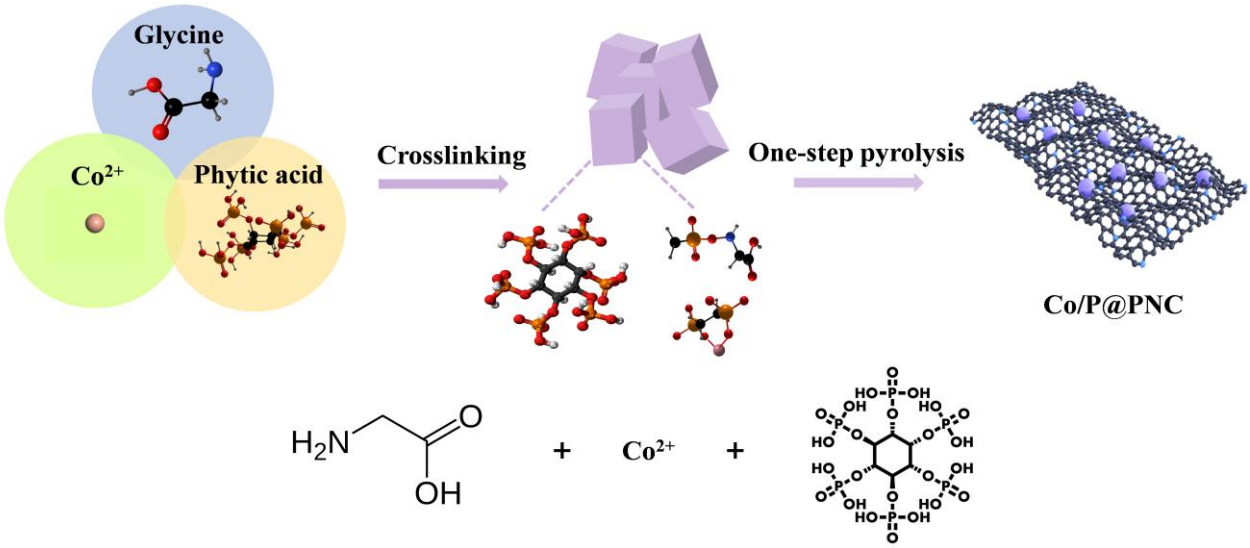

Scheme 4.1 Schematic illustration of the synthesis strategy

The existing optimum HER catalysts are derived from expensive and scarce precious metals such as Pt, which is inconsistent with the initial intention of low-cost preparation technology. Hence, it is essential to fabricate inexpensive HER catalysts.[11–16] Transition metal compounds have regular electronic structures and controllable components, making them competitive candidates to replace precious metals.[17] Furthermore, CoP has been distinguished as a research focus because of its prominent HER activity and stability.[18–24] Liu et al.[25] synthesized a hollow polyhedral cobalt phosphide with a large specific surface area and high porosity, which generated a wide range of active sites and excellent HER activity. Zhang et al. [26] reported a porous ultra-slim CoP nanosheet by phosphorylating Co_3O_4 precursors, which demonstrated decent activity and impressive stability. Nevertheless, the HER activity of CoP still can be improved. First, the conductivity of CoP is deficient, inducing tardy electron transfer and inhibiting hydrogen generation.[27] Second, the excessively negative ΔG_{H^*} of CoP reveals that the chemical bond between protons and CoP is very strong, which prevents protons from detaching from the catalyst surface.[28] Finally, the major preparation strategy for CoP is cumbersome and is mostly based on the phosphorylation process using NaH_2PO_2 as the phosphorus source. Dangerous PH_3 gases are generated during this process, which prevents large-scale production.

The construction of heteroatom-doped carbon substrates has been recognized as a feasible scheme for improving the conductivity of CoP and optimizing its ΔG_{H^*}.[29,30] Heteroatom doped carbon materials exhibit excellent charge-transfer capability, which accelerates the transfer of electrons to the active sites and boosts the desorption/adsorption process of hydrogen protons. In addition, heteroatom-doped carbon materials have a positive ΔG_{H^*}, which may neutralize the negative energy of CoP, resulting in a more moderate ΔG_{H^*} for the active sites. In particular, the doping of nitrogen atoms into carbon materials significantly changes the electronic structure and electrical conductivity of the original substrate, thereby optimizing its electrocatalytic properties.[31,32] As the electronegativity of nitrogen atoms is much greater than that of carbon atoms, the doping of N atoms increases the electron affinity of the substrate and results in electron transfer from the CoP to the nitrogen-doped carbon substrate, which means that ΔG_{H^*} will be optimized. More deeply, CoP nanoparticles will more easily deposit on

Table 4.1 Mass ratio of starting materials.

Changing species	Sample name	Mass ratio [-]		
		$Co(NO_3)_2 \cdot 6H_2O$	Phytic acid	Glycine
Co^{2+}	Co/P@NC=0.05:0.3	0.05	0.3	1
	Co/P@NC=0.1:0.3	0.1	0.3	1
	Co/P@NC=0.15:0.3	0.15	0.3	1
	Co/P@NC=0.2:0.3	0.2	0.3	1
	Co/P@NC=0.3:0.3	0.3	0.3	1
50% Phytic acid	Co/P@NC=0.15:0.2	0.15	0.2	1
	Co/P@NC=0.15:0.35	0.15	0.35	1
	Co/P@NC=0.15:0.4	0.15	0.4	1
-	w/o P	0.15	-	1
	w/o Gly	0.15	0.3	-
	only Co	0.15	-	-

the substrate, and their agglomeration is reduced owing to the altered electron distribution on the substrate surface has been changed.

In this study, we developed a simple fabrication method for a CoP-based nitrogen-doped carbon catalyst via one-step pyrolysis, as shown in Scheme 1. Throughout the synthesis process, no dangerous PH_3 gases are emitted [33] because of the use of phytic acid as a phosphorus and carbon source, and its strong metal-chelating ability could effectively anchor cobalt species, thereby achieving the dispersion of nanoscale CoP on a carbon substrate. Furthermore, glycine was used as nitrogen source, which could chelate with phytic acid to generate a three-dimensional carbon network, significantly increasing the specific surface area of the carbon substrate. Furthermore, NH_3 produced from amino acid pyrolysis and phosphoric acid from phytic acid pyrolysis enable self-etching of the carbon substrate. This process increases microporosity while successfully doping P and N atoms into the carbon network. The heteroatom-doped carbon substrate provides excellent conductivity for the integrated catalyst. Notably, phytic acid can be obtained from biomass at low cost, enabling economical large-scale synthesis. Crucially, the entire synthesis process avoids the generation of highly toxic PH_3 gas, ensuring a green and environmentally sound synthesis pathway.

4.2 Experimental

4.2.1 Materials

Cobaltous nitrate hexahydrate ($Co(NO_3)_2 \cdot 6H_2O$), glycine, and 50% phytic acid were purchased from Wako Pure Chemical Industries Ltd. (Osaka, Japan). Pt/C catalyst (20 wt.%), isopropanol and Nafion (5 wt.%) were purchased from Sigma-Aldrich (Saint Louis, USA). Nitrogen gas (purity 99.99%) was purchased from IWATANI FINE GAS Co., Ltd. All reagents were used as received without purification.

4.2.2 Synthesis of Co/P@NC catalysts

Typically, 0.03 g of $Co(NO_3)_2 \cdot 6H_2O$, 0.2 g of glycine and 0.12 g of 50% phytic acid were dissolved in 1 mL of deionized water. The mixture was then dried at 90°C for 2 h to form the Co/P@NC solid precursor. Other samples with different amounts of Co and P were also synthesized using the same procedure. The other detailed synthetic proportions are listed in Table S1. The as-made precursor was placed in a tube furnace and heated to 900 °C for 3 h under nitrogen flow. The product was denoted as Co/P@NC=0.15:0.3. We also prepared Co/P@NC=0.15:0.3 at different carbonation temperatures. The detailed ratios are listed in **Table 4.1.**

4.2.3 Characterization

The morphology and particle size were observed by transmission electron microscopy (TEM, Hitachi H800). The mass ratio of Co/P was investigated using energy-dispersive X-ray spectroscopy (EDX). The nitrogen content was measured using elemental analyzers (CHN, Perkin Elmer 2400IICHNS/O). Powder X-ray diffraction (XRD, RINT2200 with Cu Kα radiation) was used to determine the crystal structure and composition of the material phases. The element doping and valence states were evaluated using X-ray photoelectron spectroscopy (XPS, JEOL JPS-9000MX) with Mg Kα as the energy source.

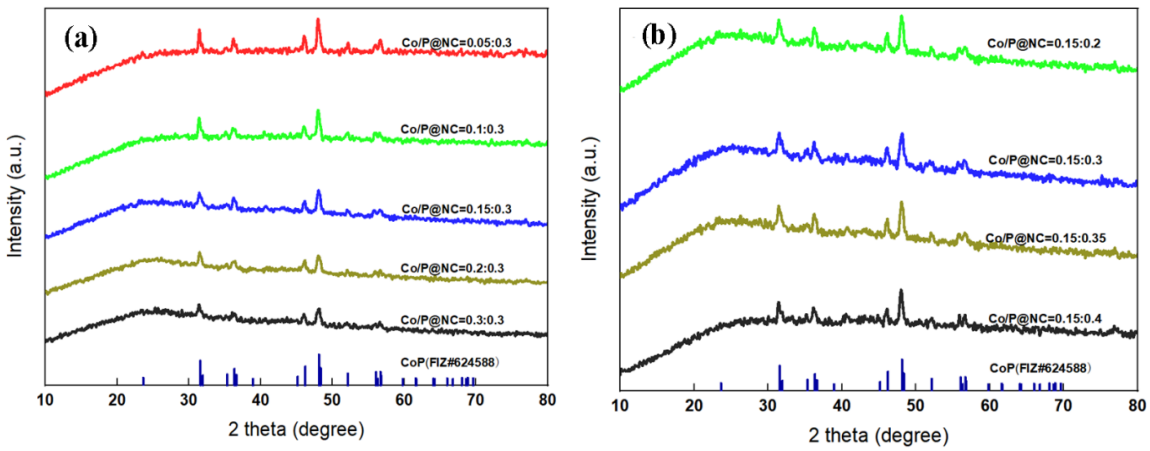

Figure 4.1 (a) XRD patterns of Co/P@NC=0.05:0.3; Co/P @ NC=0.1:0.3; Co/P@NC=0.15:0.3; Co/P@NC=0.2:0.3; Co/P@NC=0.3:0.3. (b)Co/P @ NC=0.15:0.2; Co/P @ NC=0.15:0.35; Co/P @ NC=0.15:0.4.

4.3 Results and discussion

4.3.1 The analysis of crystalline phases for each sample by using XRD measurements

We prepared Co/P@NC samples with different ratios of the starting chemicals. The detailed ratios are listed in **Table 4.1**, and typical synthesis procedures are described in the Experimental Section. The crystal structure and composition of the phases of the samples were investigated using XRD patterns, which are shown in **Figure 4.1**. Amorphous carbon-derived peaks were detected in all the samples at approximately 24.5°. All the samples in Figure 1 show diffraction peaks at 2θ = 31.6°, 35.3°, 36.3°, 46.2°, 48.1°, 56.1°, and 56.7°, corresponding to the (011), (200), (111), (112), (211), (020), and (013) crystalline surfaces of CoP (FIZ#624588), indicating that the main species of Co is CoP. When the heating temperature was below 800° C, the samples showed only broad peaks of amorphous carbon, and no characteristic peaks of CoP were found. This result suggests that CoP particles can be successfully synthesized on a carbon substrate when the heating temperature reaches 800° C and above.

4.3.2 The particle size for each sample

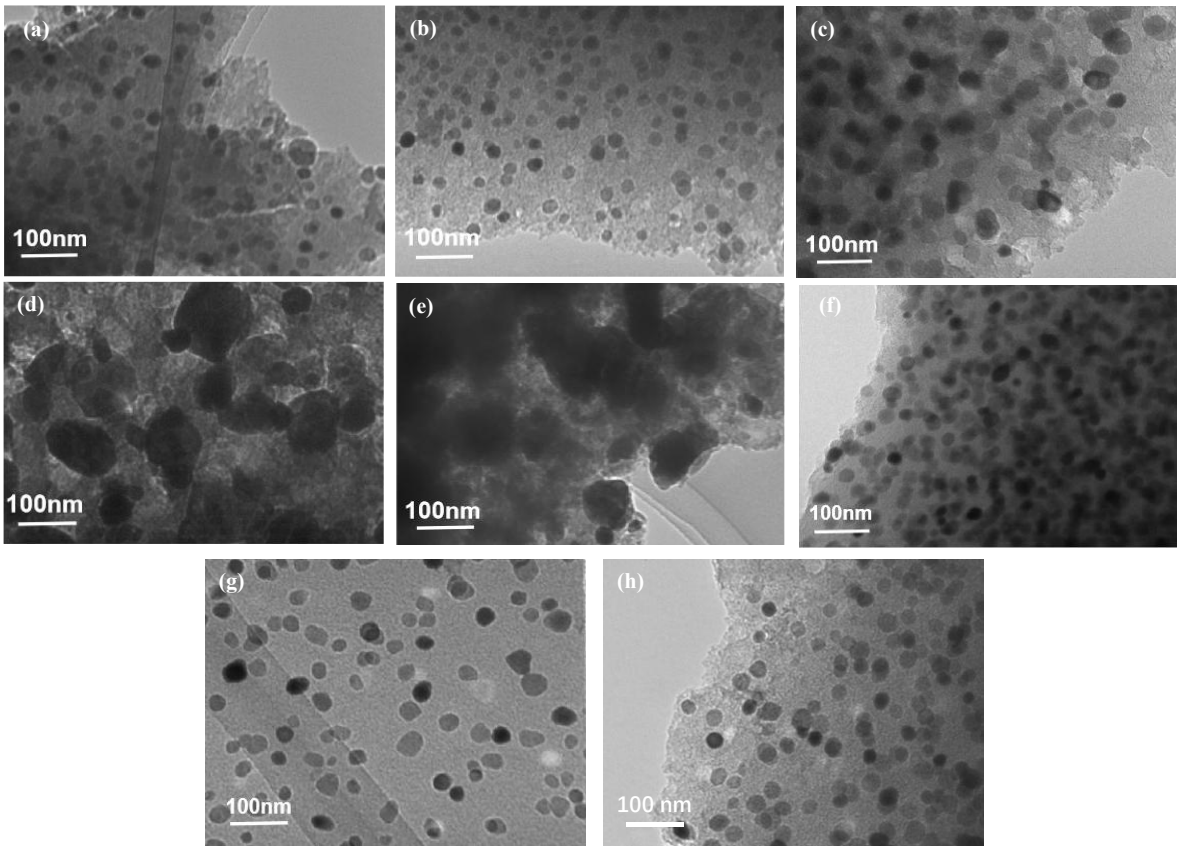

Figure 4.2 XRD patterns of (a) Co/P@NC=0.05:0.3; (b)Co/P @ NC=0.1:0.3; (c)Co/P@ NC=0.2:0.3; (d)Co/P@NC=0.3:0.3. (e)Co/P @ NC=0.15:0.2; (f)Co/P @ NC=0.15:0.35; (g)Co/P @ NC=0.15:0.4 and (h)Co/P@NC=0.15:0.3

Figure 4.2 shows the morphology and particle size distribution of the samples, suggesting that nanosized CoP particles were successfully synthesized on a carbon substrate. The distribution of the

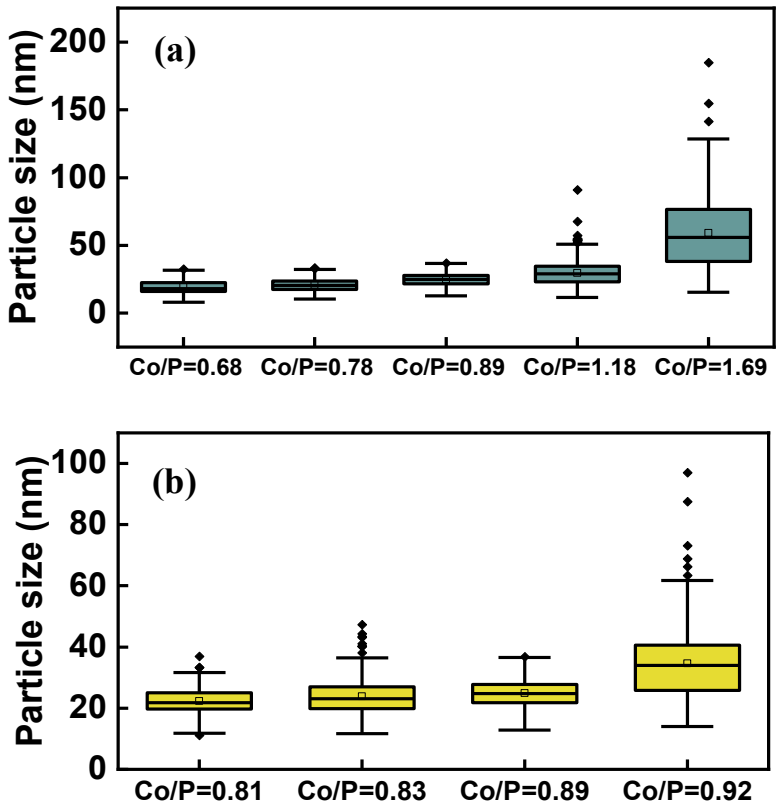

Figure 4.3 (a)Box plot of the nanoparticle size distribution of samples with different Co amounts. (b)Box plot of the nanoparticle size distribution of samples with different P amounts.

CoP particles was extremely homogeneous, and no significant agglomeration was observed. The average size of the nanoparticles was approximately 25 nm, and 90 % of the nanoparticles did not exceed 30 nm. The uniform distribution of nanoparticles ensures adequate exposure of the active sites, and the nanoscale particles allow rapid transfer of electrons and species, enhancing the HER activity of the catalyst. However, it is noteworthy that the sizes of the samples increased when the Co/P ratio increased. When the Co/P ratio reached 1.69, the samples exhibited significant agglomeration, with an average size of 63 nm. To further investigate the relationship between the Co/P ratio and particle size, the particle morphology and distribution of other samples were observed. The results were recorded in **Figure 4.2 (a-g) and Figure 4.3**. Firstly, the samples with a fixed P-adding amount and changing Co-adding amount were observed. The average particle size of the sample increased when the Co/P ratio increased. We noticed that this conclusion also applies to samples with a fixed Co addition amount and changing P addition amount. **Figure 4.3** further shows the size distribution of the CoP particles on the carbon substrates. As shown in **Figure 4.3** (a), the box plots are extremely narrow when the Co/P ratio of the sample is less than 1.18, which suggests that the CoP particles are similar in size and uniformly fixed on the substrate. However, when the Co/P ratio was larger than 0.89, the range of the box plot widened and more outliers existed, which means that the variability in the size of the CoP particles on the carbon substrate was high, and agglomeration was widespread in these samples. **Figure 4.3** (b) shows the same trend, but we observed more outliers in Co/P@NC=0.15:0.4 (Co/P=0.81) and Co/P@NC=0.15:0.35 (Co/P=0.83) than in Co/P@NC=0.15:0.3 (Co/P=0.89), implying that when the total

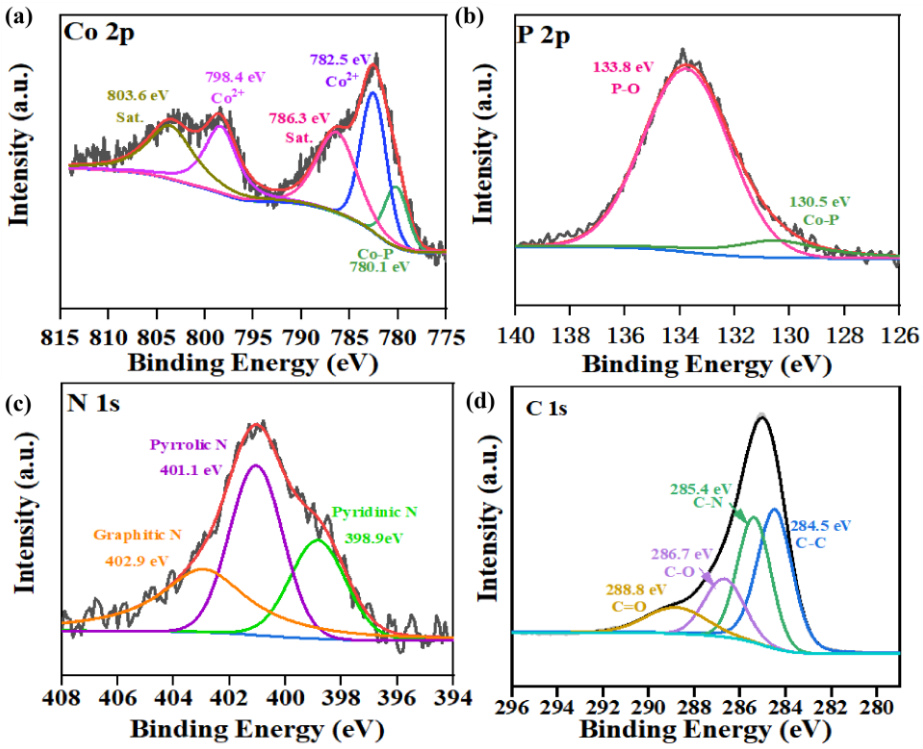

Figure 4.4 The XPS spectra of Co/P@NC=0.15:0.3 :(a) Co 2p, (b) P 2p, (c) N 1s and (d) C1s.

a

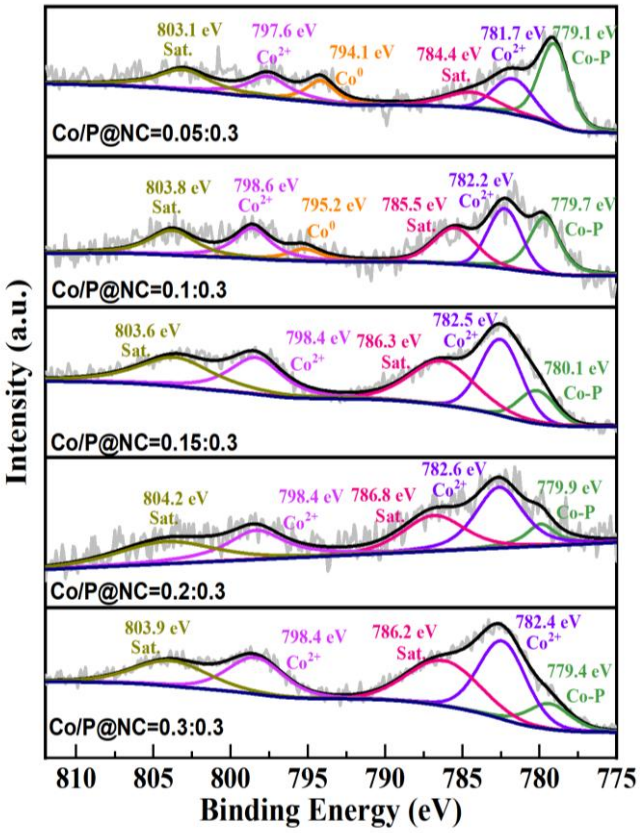

Figure 4.5 The Co 2p XPS spectra of the samples with different Co amounts and fixed P amounts.

4.3.3 The identification of chemical composition for each samples using XPS measurements

X-ray photoelectron spectroscopy (XPS) was performed to evaluate the elemental doping and valence state of the samples. The results are shown in **Figure 4.4**. The Co 2p spectrum was deconvoluted into three characteristic peaks and two satellite peaks. The peaks at 782.5 eV were identified as Co 2p3/2. [36] The peak at 780.1 eV originated from the Co formation of CoP nanoparticles on the N-doped carbon substrates. The peaks at 798.4 eV are assigned to Co 2p1/2. And the peaks located at 786.3 and 803.6 eV are satellite peaks.[40] The N 1s spectrum can be decomposed into three types of N atoms, as shown in **Figure 4.4**(c): Graphitic N (402.9 eV), Pyridinic N (398.9 eV), and Pyrrolic N (401.1 eV).[41] It is well known that these N species are incorporated into a carbon matrix. This result confirmed that almost all N species were incorporated into the carbon skeletons, and N-doped carbon was successfully synthesized. Among the three doped nitrogen types, graphitic nitrogen is formed when nitrogen atoms replace carbon atoms in the graphite carbon layer. Its outer shell has five electrons, where four electrons can form σ bonds and π bonds, while the fifth electron is in the higher-energy π* bond, making graphitic nitrogen an electron donor, thus increasing the material's n type conductivity. The incorporation of pyridinic nitrogen into the carbon framework generates numerous defect sites on the material's surface, effectively anchoring transition metal atoms and restricting the enlargement of CoP crystal size. C-N bonds (285.4 eV) [39] were observed in the XPS spectra of C 1s, which also supported the successful formation of N-doped carbon. **Figure 4.5** shows the Co 2p [40]XPS spectra of the samples with different Co and fixed P amounts. We observed that metallic Co existed in Co/P@NC=0.05:0.3 and Co/P@NC=0.1:0.3, which disappeared when the Co/P ratio increased. This may be because of the following reasons. Carbon materials can be used as reductants; when the amount of Co is low, the reductant concentration is very high, leading to the reduction of Co ions to metallic cobalt. We also found that the binding energy of Co 2p was different when the Co/P ratio was changed. Compared to

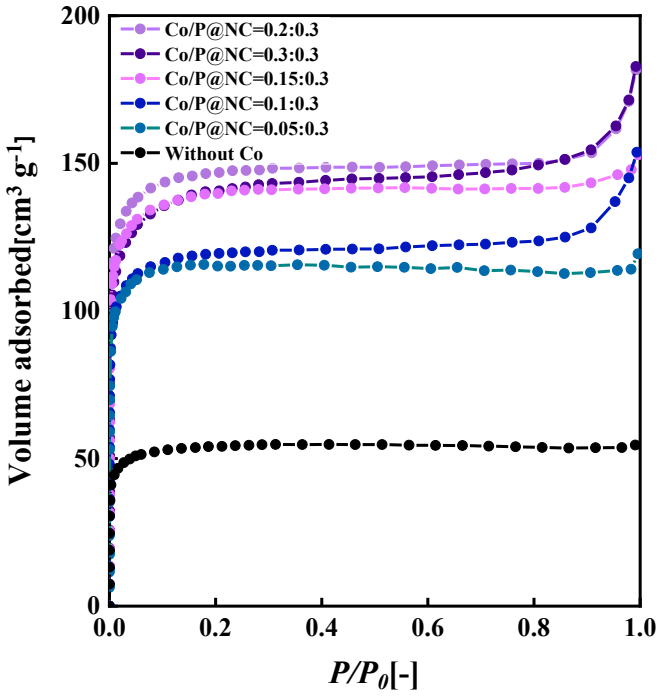

Figure 4.6 N_2 adsorption/desorption isotherms for the various samples.

Co/P@NC=0.1:0.3 and Co/P@NC=0.2:0.3, the binding energy of Co 2p exhibits respectively 0.6 eV and 0.2 eV positive shift for Co/P@NC=0.15:0.3. This indicates that the Co atoms in Co/P@NC=0.15:0.3 are in an electron-deficient state compared to those in Co/P@NC=0.1:0.3 and Co/P@NC=0.2:0.3.

4.3.4 Pore size of the various samples.

The N_2 adsorption isotherms were presented in **Figure 4.6**. Loading CoP nanoparticles on the catalyst's surface resulted in the formation of a significant number of micropores and a small quantity of macropores. The micropores experienced considerable diffusion resistance due to their small size, and the CoP particles could not adhere to the pore walls, resulting in a negligible impact on the catalysts' HER activity. The macropores promoted the enhancement of the mass transfer rate in the catalyst. However, their limited quantity implies that they are not the key factors influencing the material's HER performance. The specific surface areas were calculated according to the BET adsorption isotherm equation. We found that when the nanoparticles were formed on the carbon substrate, the specific surface area of the material was improved. The loading amount of nanoparticles becomes larger with the increasing Co content, which makes the surface area of the catalysts show an upward trend. However, when the ratio of Co/P=1.69, the specific surface area of the sample is reduced compared with Co/P@NC=0.2:0.3, which suggests a serious agglomeration.

4.3.5 The HER activity, stability and other electrical measurements of the catalysts

The HER activity measurement was conducted in a typical three-electrode system containing a 0.5 M

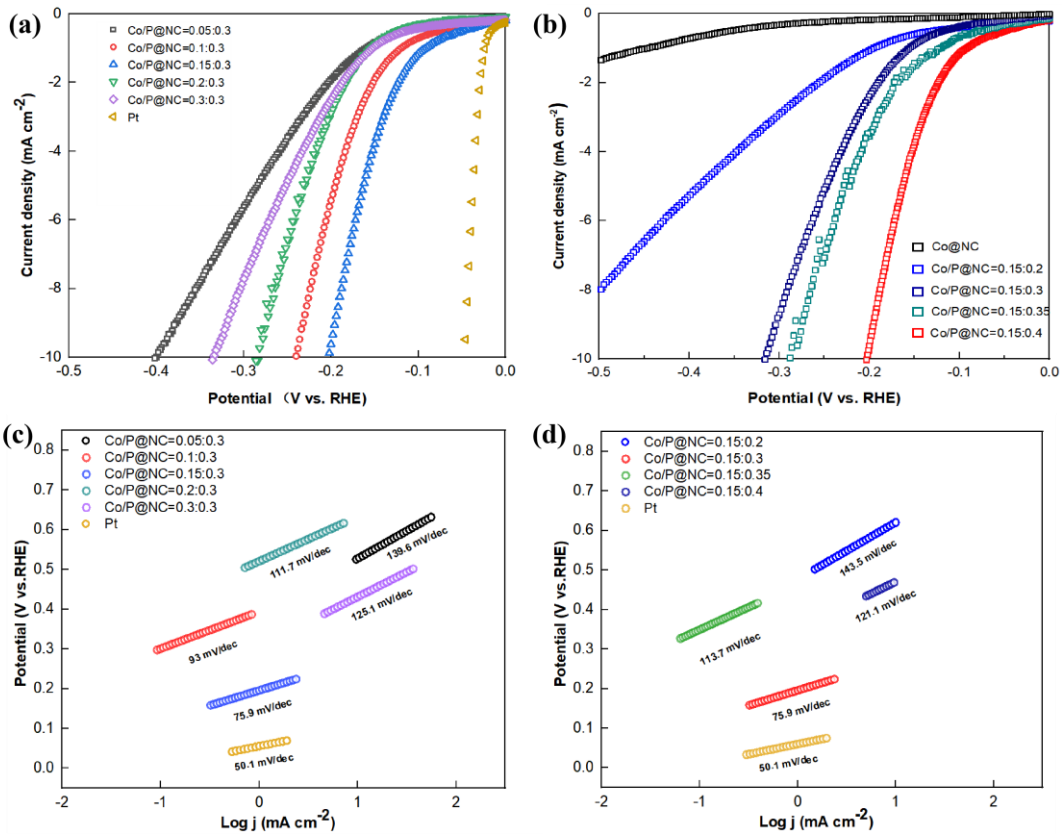

Figure 4.7 (a,b) LSV curves of various samples for HER in 0.5 M H_2SO_4. (c,d) Corresponding Tafel plots.

H_2SO_4 solution. First, we investigated the fatal species that contribute to HER activity. Compared to the N-doped carbon substrate, the Co/P@NC catalysts present a higher catalytic activity, which means that CoP is the crux species providing active sites. It is worth noting that the nitrogen-doped carbon substrate also has HER activity, indicating that it is an indispensable part of the entire catalyst. Hence, we investigated the effects of N-doped carbon substrates on the catalysts. The nitrogen content in each sample was similar, suggesting that the effect of the nitrogen amount can be ignored to boost the HER. Meanwhile, Co/P without NC, which was prepared using only cobalt nitrate and phytic acid without glycine, did not exhibit a higher catalytic activity than Co/P@NC, indicating that the N-doped carbon substrate played an important role in boosting the catalytic activity of CoP. We carbonized Co/P@NC=0.15:0.3 at different temperatures. We observed a significant increase in HER activity when the carbonization temperature was increased. We also noticed that the catalyst has basically no HER activity when the carbonization temperature is below 800 °C, which means that crystalline CoP starts to form at temperatures above 800 °C, and crystalline CoP works as a key active species for the HER. In addition to the formation of crystalline CoP, the conductivity of N-doped carbon substrates should also be an important factor. Generally, a higher carbonization temperature improves the conductivity of N-doped carbons. Thus, higher carbonization temperatures improved the conductivity of the Co/P@NC samples. The rapid transfer of electrons facilitates the rapidity of Heyrovsky reaction. Second, the effect of the Co/P ratio on the HER activity was analyzed. According to **Figure 4.7**(a,b), the catalytic activity of the samples increased and then declined with increasing Co/P ratio. Additionally, w/o P, which was prepared using only Co nitrate and glycine, had no activity for the HER, which also supports that CoP species should be a crucial active species for the HER. Among all the samples, Co/P@NC=0.15:0.3 (Co/P=0.89) exhibited the best HER catalytic activity with an overpotential of 202 mV to achieve a current density of 10 mA cm^{-2}, which is much closer to the performance of Pt than the other samples. To explain the optimal performance of Co/P@NC=0.15:0.3, we analyzed it in two aspects. First, according to the XPS results, the sample has the most suitable Co-P bond strength, which means that this sample has the optimum $\triangle G_{H^*}$. In addition, we believe that the effect of particle size on catalyst activity is critical. According to Figure S5, we found that the binding energy of Co 2p exhibits a 0.2 eV positive shift for Co/P@NC=0.2:0.3 when it is compared to Co/P@NC=0.1:0.3, suggesting that Co/P@NC=0.2:0.3 has more suitable $\triangle G_{H^*}$[41]. However, Co/P@NC=0.1:0.3 exhibited superior catalytic performance compared to Co/P@NC=0.2:0.3, which means that particle size and distribution are also the main factors impeding the HER dynamics. Regarding the effect of particle size on sample performance, we found that when the added amount of P was fixed, the loading amount of CoP particles on the carbon substrate increased with increasing Co/P ratio, thus optimizing the HER catalytic performance. However, when the Co/P ratio becomes too high, agglomeration of CoP nanoparticles occurs, fewer active sites are exposed, and mass transfer is limited, leading to a decrease in the HER catalytic activity. When Co/P reached 0.89, the distribution and loading amount of the CoP nanoparticles were optimal, and therefore exhibited the highest HER activity. To understand the catalytic mechanism in depth, we also investigated the Tafel slopes of the samples. Based on **Figure 4.7**(c, d), the Tafel slope of Co/P@NC=0.15:0.3 is 75.9 mV/dec, approaching the theoretical value of the Heyrovsky step, which means that the catalytic reaction follows the Volmer-Heyrovsky mechanism. The Tafel slope change trend of the as-made samples is consistent with the changing trend of HER activity, which also supports our conclusions.

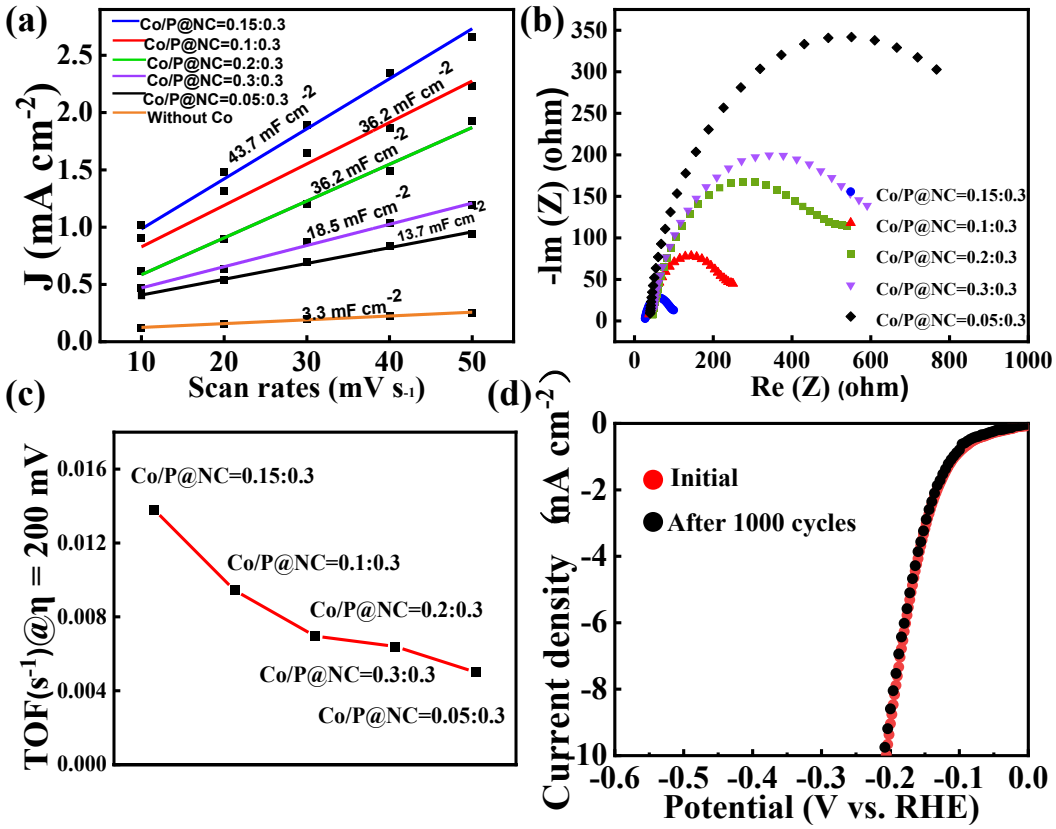

Figure 4.8 (a) Electrochemical active surface areas, (b) EIS curves in 0.5 M H_2SO_4, (c) The turnover frequency per site at η=200 mV and (d)The HER activity between and after 1000 cycles.

To further characterize the electrochemical active surface area (ECSA) of the catalysts, we calculated the double-layer capacitance by cyclic voltammetry (CV), and the results are recorded in **Figure 4.8**(a). All catalysts have larger ECSA compared to the nitrogen-doped carbon substrates without CoP loading, which suggests CoP is the key species that provides active sites. The Cdl value of Co/P@NC=0.15:0.3 is 43.7 mF cm^{-2}, much better than other samples, which indicates that it has the most exposed active sites. The Cdl value of Co/P@NC = 0.05: 0.3 is only 13.7 mF cm^{-2}, which may be caused by the poor loading amount of CoP nanoparticles. Co/P@NC = 0.2: 0.3 and Co/ P@NC = 0.3: 0.3 have higher CoP loadings, but their ECSA is smaller than Co/P@NC = 0.15: 0.3 and Co/P@NC = 0.1: 0.3, which again proved the aggregation of CoP nanoparticles on their surfaces. To research the electrochemical kinetics of the catalysts, we also carried out the electrochemical impedance spectroscopy (EIS) tests. As we can see in **Figure 4.8**(b), Co/ P@NC = 0.15: 0.3 has the lowest charge and mass transfer resistance, which is one of the reasons for the optimal HER activity of this sample. Co/P@NC = 0.2: 0.3 and Co/P@NC = 0.3: 0.3 have sluggish mass transfer kinetics, which is related to the aggregation of CoP nanoparticles on their surfaces. Compared with Co/P@NC = 0.2: 0.3 and Co/P@NC = 0.3: 0.3, sample Co/P@NC = 0.05: 0.3 shows a higher electrochemical impedance, which may be caused by the lack of pore structure.

In addition, the turnover frequency (TOF) and Exchange current density were calculated to characterize the intrinsic activity of the catalysts. Co/P@NC = 0.15: 0.3 has the highest TOF (0.013) due to its fastest mass transfer kinetics and optimum $\triangle G_{H^*}$ compared to other samples. Although Co/P@NC = 0.2: 0.3 has a more suitable $\triangle G_{H^*}$ than Co/P@NC = 0.1: 0.3, its TOF is still lower, which is due to its sluggish mass transfer kinetics. This again proves that the size of CoP nanoparticles is also a key factor affecting

the HER activity of the catalysts. The value exchange current density has the same variation trend as the TOF value, which also helps to prove our points.

Furthermore, the durability of the best sample is investigated. A similar LSV curve was obtained even after 1000 cycles of CV in the range of 0 V to 0.5 V vs. RHE. This result indicates that the best sample has high durability.

4.4 Conclusion

In conclusion, a CoP-anchored nitrogen-doped carbon catalyst was successfully fabricated by one-step pyrolysis of a mixture of glycine, phytate, and cobalt salts. Glycine was used as the nitrogen and carbon source because of its ability to form stable complex precursors with phytic acid. After pyrolysis at 900 °C, the above precursor turned into a nitrogen atom-doped carbon substrate, applying excellent conductivity to the whole catalyst, allowing the Heyrovsky reaction step to proceed rapidly. In addition to forming a carbon framework, phytic acid has been used as a phosphorus source. It chelates Co ions to form a stable chelate ring precursor, generating a highly catalytically active CoP species after pyrolysis at temperatures above 800 °C. The CoP particle size was controlled by adjusting the amount of Co and P in the precursor. The nanoscale size and uniform distribution ensured adequate exposure of the active sites, allowing the catalysts to exhibit excellent HER activity. Notably, this synthesis method is facile and cost-effective, avoids the generation of dangerous PH_3 gas, and provides a reference for the large-scale production of CoP-based catalysts. This work opens a new avenue for sustainable catalyst design for hydrogen evolution reactions.

Reference

[1] Ding J, Yang H, Zhang S, et al. Advances in the electrocatalytic hydrogen evolution reaction by metal nanoclusters-based materials[J]. Small, 2022, 18(52): 2204524.

[2] Li Y, Li Y, Li X, et al. Microreactor platform for continuous synthesis of electronic doped quantum dots[J]. Nano Research, 2022, 15(10): 9647-9653.

[3] Atchudan R, Perumal S, Edison T N J I, et al. Facile synthesis of novel molybdenum disulfide decorated banana peel porous carbon electrode for hydrogen evolution reaction[J]. Chemosphere, 2022, 307: 135712.

[4] Chen M, Kitiphatpiboon N, Feng C, et al. Recent progress in transition-metal-oxide-based electrocatalysts for the oxygen evolution reaction in natural seawater splitting: A critical review[J]. EScience, 2023, 3(2): 100111.

[5] Li Y, Zhou L, Guo S. Noble metal-free electrocatalytic materials for water splitting in alkaline electrolyte[J]. EnergyChem, 2021, 3(2): 100053.

[6] Feng Y, Guan Y, Zhou E, et al. Nanoscale double-heterojunctional electrocatalyst for hydrogen evolution[J]. Advanced Science, 2022, 9(18): 2201339..

[7] Yang C, Wang Z, Li Z, et al. Nitrogen disturbance awakening the intrinsic activity of nickel phosphide for boosted hydrogen evolution reaction[J]. ChemSusChem, 2022, 15(16): e202200072.

[8] Niknazar S, Ensafi A A, Heydari-Soureshjani E, et al. Green application of trimetallic nickel-cobalt-molybdenum nanocomposites on 3D graphene oxide as a powerful electrocatalyst for hydrogen evolution reaction[J]. Chemosphere, 2022, 294: 133670.

[9] Xue Y, Xu Y, Yan Q, et al. Coupling of Ru nanoclusters decorated mixed-phase (1T and 2H) MoSe2 on biomass-derived carbon substrate for advanced hydrogen evolution reaction[J]. Journal of Colloid and Interface Science, 2022, 617: 594-603.

[10] Jia H, Shang N, Chen J, et al. Facile synthesis of N-doped carbon nanoframes encapsulated by CoP nanoparticles for hydrogen evolution reaction[J]. Journal of Colloid and Interface Science, 2021, 601: 338-345.

[11] Pei L, Qiao H, Chen B, et al. Pt Edge-Doped MoS2: Activating the Active Sites for Maximized Hydrogen Evolution Reaction Performance[J]. Small, 2021, 17(52): 2104245.

[12] Zheng Y, Jiao Y, Zhu Y, et al. Hydrogen evolution by a metal-free electrocatalyst[J]. Nature communications, 2014, 5(1): 3783.

[13] Zhu Q, Xu Z, Qiu B, et al. Emerging cocatalysts on g-C3N4 for photocatalytic hydrogen evolution[J]. Small, 2021, 17(40): 2101070.

[14] Li Y, Zou Y, Bai Y, et al. A novel worm-like micelles@ MOFs precursor for constructing hierarchically porous CoP/N-doped carbon networks towards efficient hydrogen evolution reaction[J]. Journal of Colloid and Interface Science, 2021, 600: 872-881.

[15] Lai Z, Ma Q, Zhang H. Novel structured transition metal dichalcogenide nanosheets[J]. 2018.

[16] Zhang A, Liang Y, Zhang H, et al. Doping regulation in transition metal compounds for electrocatalysis[J]. Chemical Society Reviews, 2021, 50(17): 9817-9844.

[17] Jin H, Liu X, Chen S, et al. Heteroatom-doped transition metal electrocatalysts for hydrogen evolution reaction[J]. ACS Energy Letters, 2019, 4(4): 805-810.

[18] Liu T, Li P, Yao N, et al. CoP-doped MOF-based electrocatalyst for pH-universal hydrogen

evolution reaction[J]. Angewandte Chemie, 2019, 131(14): 4727-4732.

[19] Zhang L, Zhang J, Fang J, et al. Cr-doped CoP nanorod arrays as high-performance hydrogen evolution reaction catalysts at high current density[J]. Small, 2021, 17(28): 2100832.

[20] Yang H, Zhang Y, Hu F, et al. Urchin-like CoP nanocrystals as hydrogen evolution reaction and oxygen reduction reaction dual-electrocatalyst with superior stability[J]. Nano letters, 2015, 15(11): 7616-7620.

[21] Wang X, Fei Y, Chen J, et al. Directionally in situ self-assembled, high-density, macropore-oriented, CoP-impregnated, 3D hierarchical porous carbon sheet nanostructure for superior electrocatalysis in the hydrogen evolution reaction[J]. Small, 2022, 18(2): 2103866.

[22] Liu H, Ma X, Hu H, et al. Robust NiCoP/CoP heterostructures for highly efficient hydrogen evolution electrocatalysis in alkaline solution[J]. ACS applied materials & interfaces, 2019, 11(17): 15528-15536.

[23] Li H, Zhao X, Liu H, et al. Sub-1.5 nm Ultrathin CoP Nanosheet Aerogel: Efficient Electrocatalyst for Hydrogen Evolution Reaction at All pH Values[J]. Small, 2018, 14(41): 1802824.

[24] Zeng Y, Wang Y, Huang G, et al. Porous CoP nanosheets converted from layered double hydroxides with superior electrochemical activity for hydrogen evolution reactions at wide pH ranges[J]. Chemical Communications, 2018, 54(12): 1465-1468.

[25] Liu Q, Tang C, Lu S, et al. Rationally tuning the atomic ratio of electrodeposited NiP for greatly enhanced hydrogen evolution in alkaline media[J]. Chemical Communications, 2018, 54(87): 12408-12411.

[26] Zhang C, Huang Y, Yu Y, et al. Sub-1.1 nm ultrathin porous CoP nanosheets with dominant reactive {200} facets: a high mass activity and efficient electrocatalyst for the hydrogen evolution reaction[J]. Chemical Science, 2017, 8(4): 2769-2775.

[27] Zhou Z, Mahmood N, Zhang Y, et al. CoP nanoparticles embedded in P and N co-doped carbon as efficient bifunctional electrocatalyst for water splitting[J]. Journal of energy chemistry, 2017, 26(6): 1223-1230.

[28] Zhu R, Chen F, Wang J, et al. Multi-channel V-doped CoP hollow nanofibers as high-performance hydrogen evolution reaction electrocatalysts[J]. Nanoscale, 2020, 12(16): 9144-9151.

[29] Liu B, Cao B, Cheng Y, et al. Ultrafine CoP/Co2P nanorods encapsulated in janus/twins-type honeycomb 3D nitrogen-doped carbon nanosheets for efficient hydrogen evolution[J]. Iscience, 2020, 23(7).

[30] Cai H, Xiong L, Wang B, et al. N-doped CNT as electron transport promoter by bridging CoP and carbon cloth toward enhanced alkaline hydrogen evolution[J]. Chemical Engineering Journal, 2022, 430: 132824.

[31] Li Y, Zhang B, Wang W, et al. Selective-etching of MOF toward hierarchical porous Mo-doped CoP/N-doped carbon nanosheet arrays for efficient hydrogen evolution at all pH values[J]. Chemical Engineering Journal, 2021, 405: 126981.

[32] Ma J, Chi X, Huang Y, et al. Biomass-based protic ionic liquid derived N, P, co-doped porous carbon-coated CoP nanocrystals for efficient hydrogen evolution reaction[J]. Journal of Materials Science, 2021, 56(32): 18188-18199.

[33] Pu Z, Amiinu I S, Kou Z, et al. RuP2-based catalysts with platinum-like activity and higher durability for the hydrogen evolution reaction at all pH values[J]. Angewandte Chemie

International Edition, 2017, 56(38): 11559-11564.

[34] Sun D, Lin S, Yu Y, et al. One-pot synthesis of N and P Co-doped carbon layer stabilized cobalt-doped MoP 3D porous structure for enhanced overall water splitting[J]. Journal of Alloys and Compounds, 2022, 895: 162595.

[35] Gong Y, Xu L H, Zhang X J, et al. Phytic acid-assisted hollow Fe_2P/NC nanoshuttle derived from NH_2MIL: Synthesis strategy and electrochemical application for hydrogen evolution[J]. Journal of Alloys and Compounds, 2023, 947: 169418.

[36] Duan Z, Zhao D, Sun Y, et al. Bifunctional Fe-doped CoP@ Ni_2P heteroarchitectures for high-efficient water electrocatalysis[J]. Nano Research, 2022, 15(10): 8865-8871.

[37] Ma Y, Liu X, Tang M, et al. Waste eggshell-derived N, P, S tri-doped core-shell catalysts for efficient Fenton-like catalysis[J]. Chemical Engineering Journal, 2022, 440: 135879.

[38] Xu M, Han L, Han Y, et al. Porous CoP concave polyhedron electrocatalysts synthesized from metal–organic frameworks with enhanced electrochemical properties for hydrogen evolution[J]. Journal of Materials Chemistry A, 2015, 3(43): 21471-21477.

[39] Wang X, Zhou X, Li C, et al. Asymmetric $Co_{@}$ N_3P_1 Trifunctional Catalyst with Tailored Electronic Structures Enabling Boosted Activities and Corrosion Resistance in an Uninterrupted Seawater Splitting System[J]. Advanced Materials, 2022, 34(34): 2204021.

[40] Wang C, Chen W, Yuan D, et al. Tailoring the nanostructure and electronic configuration of metal phosphides for efficient electrocatalytic oxygen evolution reactions[J]. Nano Energy, 2020, 69: 104453.

[41] Liu M, Liu J, Song Y, et al. Mononuclear iron-dependent electrocatalytic activity of metal-nitrogen-carbon catalysts for efficient oxygen reduction reaction[J]. Applied Catalysis A: General, 2019, 583: 117120.

[42] Ouyang B, Zhang Y, Wang Y, et al. Plasma surface functionalization induces nanostructuring and nitrogen-doping in carbon cloth with enhanced energy storage performance[J]. Journal of Materials Chemistry A, 2016, 4(45): 17801-17808.

[43] Wang X, Fei Y, Li W, et al. Gold-incorporated cobalt phosphide nanoparticles on nitrogen-doped carbon for enhanced hydrogen evolution electrocatalysis[J]. ACS Applied Materials & Interfaces, 2020, 12(14): 16548-16556.

Chapter 5

Straightforward synthesis of S-doped Co_2P nanoparticles on a P, S co-doped carbon substrate by using ion exchange resin for hydrogen evolution reaction

In Chapter 4, we developed a green and straightforward synthetic approach to prepare the CoP/NC catalyst. However, the experimental results indicate that the prepared CoP catalyst still exhibits a certain gap in HER activity compared to Pt-based catalysts. Therefore, in this chapter, we will employ other precursors with strong chelating capabilities to further reduce the size of CoP particles on the carbon substrate. Concurrently, we introduce heteroatoms to modulate the electron density of CoP species, thereby optimizing their ΔG_{H^*} More specifically, we developed a facile method to synthesize an S-doped Co_2P anchored P,S co-doped carbon catalyst via an ion-exchange process and one-step pyrolysis. Through prolonged ion exchange, cobalt ions were uniformly immobilized onto the organic carbon framework, ensuring a uniform distribution of Co_2P nanoparticles and robust interactions between the resultant product and carbon substrate. The agglomeration of the Co_2P nanoparticles during pyrolysis was prevented, thus generating a larger number of exposed active sites. In addition, doping with S can efficiently regulate the electronic states of the Co sites, resulting in an improved ΔG_{H^*}.

5.1 Introduction

In recent years, the misuse of fossil fuels has led to severe environmental problems, increasing the urgency to find renewable energy sources [1–3]. Among all the possible options, hydrogen stands out because of its considerable energy density and non-polluting combustion products [4–8]. While various methods for producing hydrogen, only water splitting is truly carbon-free [9–11]. However, the implementation of this method has been hindered by its enormous energy barrier, which has plagued scientists over several decades. The hydrogen evolution reaction (HER), an essential half-reaction for water splitting, is a critical factor in determining the water splitting efficiency [12–15]. The best HER catalysts are currently Pt-based, but their high cost and scarcity limit their use. Therefore, developing affordable catalysts with high HER efficiency to replace Pt-based materials is crucial [16–19].

Cobalt phosphides, particularly CoP and Co_2P, are cost-effective and increasingly researched as HER catalysts [20–24]. Co_2P, in particular, shows promise as an excellent HER catalyst but has received less attention than CoP in this field [25,26]. Zhaoyu Jin et al. combined electrochemical impedance spectroscopy (EIS) tests with DFT calculations to conclude that the metallic properties of Co_2P result in

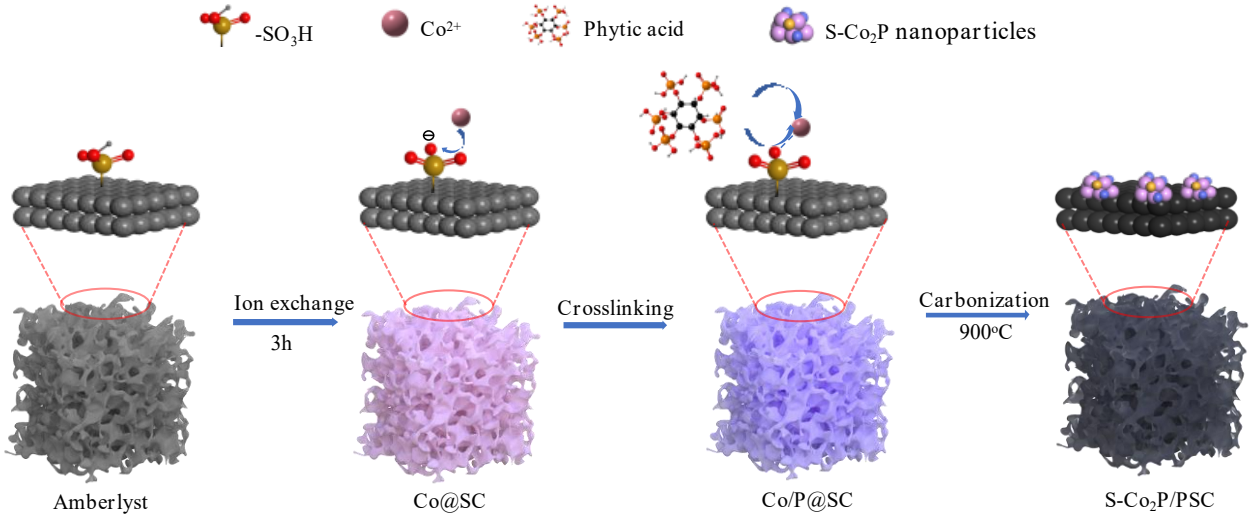

Scheme 5.1 Schematic representation of synthetic method for S-Co2P/PSC.

a lower conductivity compared to CoP, which accelerates the HER rate [27]. Additionally, Co_2P has a high Co content and Co sites are crucial for providing HER activity, indicating that Co_2P has great potential as a HER catalyst. However, the current HER activity of Co_2P is still lower than that of the Pt-based catalysts. It is well known that the enhancement mechanism of cobalt phosphides is that phosphorus, possessing higher electronegativity, extracts electrons from cobalt atoms, rendering the cobalt atoms in a state of electron deficiency, thus weakening their ability to adsorb hydrogen ions and enhancing HER activity. Co_2P has a cobalt-rich and phosphorus-poor structure, implying that its hydrogen adsorption free energy (ΔG_{H^*}) is not nearly zero.

At present, the main methods to regulate the ΔG_{H^*} of HER catalyst include interface engineering, heteroatom doping, phase engineering and heterostructure construction [28–33]. Although many reports have been published for heteroatom doping Co_2P, most of them focused on the area of N doping, few reports related to use S atoms for doping. For example, Yana Men et al. successfully synthesized N-doped Co_2P nanorod arrays and found that after doping with N atoms, the electronic structure of the Co active sites was changed, resulting in a superior HER activity compared to Co_2P [34]. Xiaohao Ji et al. reported a flakelike Co_2P catalyst supporting on $NiCo_2O_4$ nanorods array. They found that after doping N atoms, the charge will transfer from Co to N and lowers the d-band center of Co. These literatures demonstrate that the introduction of heteroatoms with greater electronegativity (compare to P atom) can effectively modulate ΔG_{H^*} of the active site [35]. Besides, the agglomeration of transition metal phosphides at high temperatures is also a fatal issue that affects the catalytic performance of Co_2P. With increasing temperature, the migration speed of the particles accelerates, and the agglomeration phenomenon becomes more severe. Such agglomeration inevitably leads to the loss of active surface area, resulting in the deactivation of the catalyst. Therefore, it is crucial to propose strategies to restrict the growth of transition-metal phosphide crystals and promote their uniform distribution. Apart from the influence of particle dispersion, the conductivity of the catalyst is also a significant factor that affects HER efficiency [36–38].

In this study, we developed S-doped Co_2P nanoparticle-anchored carbon catalysts using an ion-exchange method (**Scheme 5.1**). Amberlyst, a sulfur and carbon source, can exchange and immobilize

Co^{2+} on carbon-based resin [39]. The strong interaction between the carbon-based resin and Co^{2+} ensures a uniform distribution of cobalt species, prevents the agglomeration of Co_2P nanoparticles during pyrolysis, and ensures a larger number of exposed active sites. The Cdl of the sample subjected to ion exchange was elevated from 9 mF cm^{-2} to 22 mF cm^{-2}, compared to sample subjected to physical mixing only. The loading amount of Co was also improved. (From 1.6% to 2.9%). Scheme 1 Schematic representation of synthetic method for S-Co_2P/PSC. Apart from that, the TOF (η = 250 mV) fo the sample performed ion exchange was elevated from 0.034 s^{-1} to 0.085 s^{-1}, compared to physical mixing sample. Phytic acid was used as the phosphorus source. This crosslinks with Co^{2+} in the carbon-based resin to generate stable chelation. The pyrolysis and reduction of the -SO_3^{2-} group in Amberlyst occurred simultaneously with the formation of Co_2P nanoparticles, allowing the smooth introduction of S atoms into the Co_2P lattice. The S atom was choosing for the following reasons. Firstly, the S atoms (rs=1.04 Å) is smaller than P (rp=1.30 Å) atoms, suggesting a stronger electronegativity. As a results, the S atom obtains a fraction of electrons from the Co species, allowing the Co active center to exhibit a stronger electron-deficient state, indicating a optimized ΔG_{H^*}. Through experiment, we found that the overpotential at 10 mA cm^{-2} of the sample subjected to S doped samples was elevated from 161 to 352 mV, compared to sample without S element. Secondly, some P and S atoms are doped into the carbon substrate, which makes the carbon substrate more conductive and thus accelerates the Volmer-Tafel/Heyrovsky reaction process.

Table 5.1 Mass ratio of starting materials.

Sample name	Mass ratio [-]			
	$CoSO_4 \cdot 7H_2O$	Amberlyst	50% Phytic acid	Amberlite
0.12 S-Co_2P/PSC	0.0506	1.5	1	/
0.24 S-Co_2P/PSC	0.1012	1.5	1	/
0.36 S-Co_2P/PSC	0.1518	1.5	1	/
0.48 S-Co_2P/PSC	0.202	1.5	1	/
Co_2P/PC	0.1012	/	1	1.5
wo ion exchange	0.1012	1.5	1	/
wo phytic acid	0.1012	1.5	/	/
wo Co species	/	1.5	1	/
Amb	/	1.5	/	/

5.2 Experimental

5.2.1 Materials

Cobalt sulfate heptahydrate ($CoSO_4·7H2O$), 50% phytic acid isopropanol, and Nafion (5 wt%) were procured from Wako Pure Chemical Industries, Ltd. (Osaka, Japan). Amberlyst (dry, hydrogen form), Amberlite (hydrogen form) and Pt/C catalyst (20 wt%) were acquired from Sigma-Aldrich (Saint Louis, USA). Nitrogen gas with a purity of 99.99% was obtained from IWATANI FINE GAS Co., Ltd. All the reagents were used without further purification.

5.2.2 Synthesis of Co/Amb

Typically，1.5 g of Amberlyst was dispersed in deionized water (60 ml deionized water to form a suspension. Next, 0.24 mmol of $CoSO_4·6H_2O$ was dissolved in 30 ml of deionized water and added dropwise into the above suspension. The mixture was stirred constantly for 3 h to ensure that all Co^{2+} ions were exchanged with Amberlyst. The resulting materials were washed with deionized water and dried at 90 ℃ for 2 h. This sample was named as "0.24 Co/Amb". Using the same method, samples with different amounts of Co^{2+} were obtained with a fixed mass of Amberlyst (1.5 g). These samples were donated as "x Co/Amb"(x = 0.12, 0.36 and 0.48), where x means the adding mole of Co^{2+}. The detailed synthetic proportions are listed in **Table 5.1**.

5.2.3 Synthesis of S doped Co2P/PSC and Co2P/PC

Firstly, 0.15 g of x Co/Amb was spread on a mortar. Secondly, 0.1 g of 50 % phytic acid was dissolved in 1 mL of deionized water and added dropwise onto the above x Co/Amb. The mixture was then ground for 5 min to ensure complete contact of all components. After drying at 90 ℃ for 2 h, the precursor was placed in a tube furnace and heated to 900 ℃ for 3 h under a nitrogen flow. The resulting sample was denoted as "x S-Co_2P/PSC". To explore the effect of S, we synthesized "Co_2P/PC" by the same procedure using Amberlite instead of Amberlyst. In addition, we also synthesized samples by the same procedure without Co and phytic acid, respectively. Those samples were donated as 'wo Co species' and 'wo phytic acid', respectively. To confirm the effect of ion exchange step, we mixed CoSO4·6H2O with phytic acid and added Amberlyst into the mixture, followed by drying at 90 ℃ and calcining at 900 ℃ for 3 h under a nitrogen flow. The sample was donated as 'wo ion exchange'.

5.2.4 Characterization

The examination of morphology and particle dimensions was conducted through the utilization of transmission electron microscopy (TEM, Hitachi H800). The mass ratio of cobalt and phosphorus (Co/P) was analyzed via energy-dispersive X-ray spectroscopy (EDX). In addition, the amounts of Co and P were determined by Inductively Coupled Plasma (ICP) measurements. Powder X-ray diffraction (XRD, RINT2200 with Cu Kα radiation) was used to determine the crystal structures and compositional phases. For an exhaustive investigation into element doping and the discernment of valence states, we used X-ray photoelectron spectroscopy (XPS, JEOL JPS-9000MX) with Mg Kα as the energy source.

5.2.5 Characterization

To evaluate the hydrogen evolution reaction (HER) activity of the samples, we employed an ALS 2325

bi-potentiostat equipped with a standard three-electrode system. Hg/Hg_2Cl_2 served as the reference electrode for the 0.5 M H_2SO_4 electrolyte, while a graphite rod functioned as the counter electrode. To prepare the working electrode, the following procedure was followed: 8 mg of catalyst powder was dispersed in a solution containing 1 ml of isopropanol, 5 wt% Nafion, and deionized water ($V_{isopropanol}$: V_{Nafion}: $V_{Deionized\ water}$ = 1:1:8). The mixture was ultrasonicated to obtain homogeneous catalyst ink. Subsequently, a suspension (4 μg) of the catalyst ink was evenly coated onto a carbon cloth (with an area of 0.1256 cm^2) of a rotating ring-disk electrode, forming a thin and uniform carbon layer. The working electrode was thoroughly dried under ambient conditions for 30 min to complete its preparation. The measurement potentials were referenced to the reversible hydrogen electrode (RHE) as determined by the following equation: $E_{RHE} = E_{Hg/Hg_2Cl_2} + 0.244\ (0.5\ M\ H_2SO_4)$

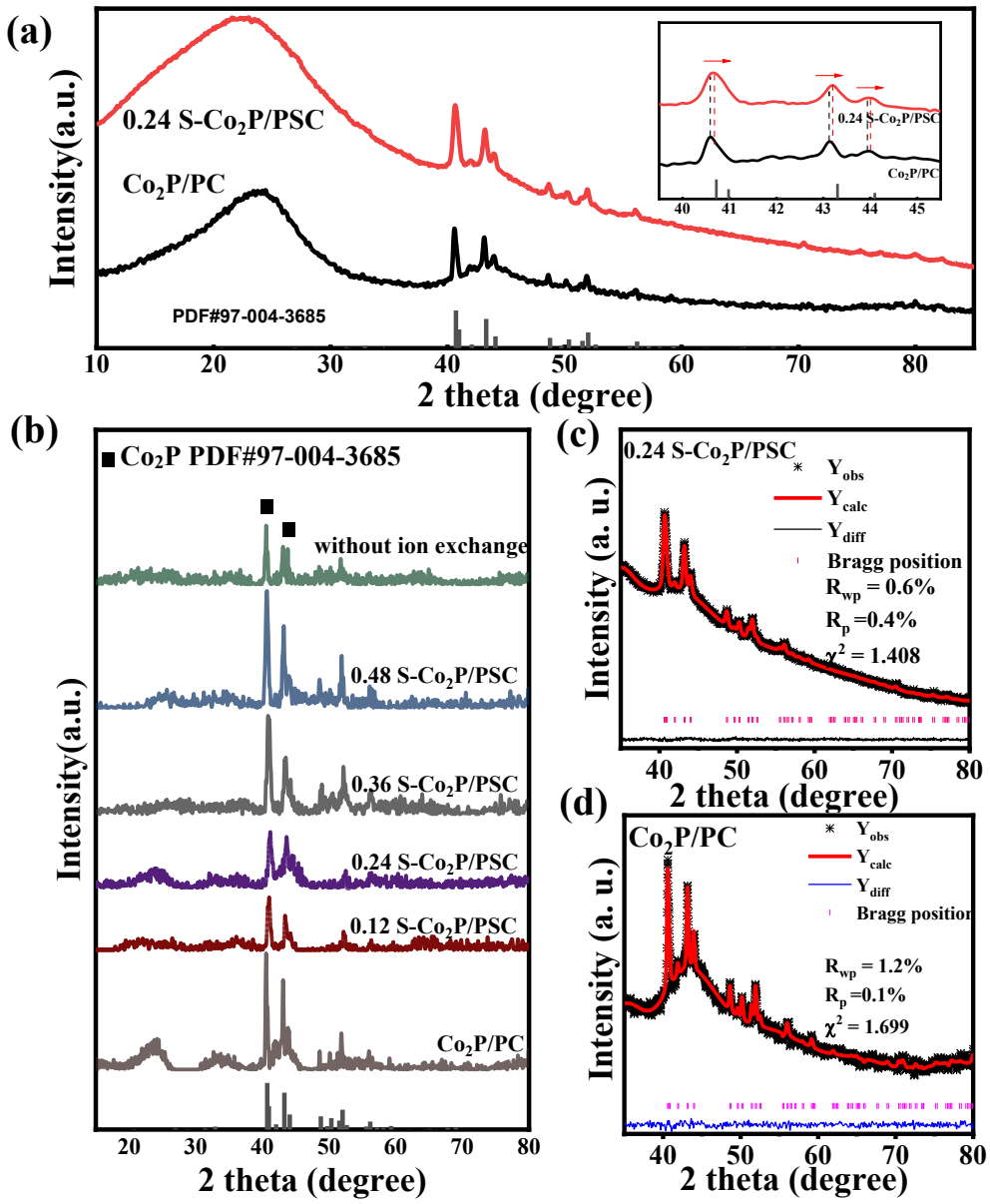

Figure 5.1 (a) XRD patterns of 0.24 S-Co_2P/PSC and Co_2P/CC, (b) XRD patterns of other samples, (c) Rietveld refinement of XRD patterns for Co_2P/PC, and (d) rietveld refinement of XRD patterns for 0.24 S-Co_2P/PSC.

To assess the HER activity of the samples, linear sweep voltammetry (LSV) was conducted at a sweep rate of 5 mV s^{-1} and a rotation speed of 1600 rpm under a N_2 flow at 80 mL/min. The electrochemical impedance spectroscopy (EIS) measurements were recorded in the frequency range from 200,000 to 10 Hz.

5.3 Results and discussion

5.3.1 The analysis of crystalline phases for each sample by using XRD measurements

Table 5.2 The lattice information of the samples.

Sample	Space group	Lattice constants	D(112)/Å	Volume/Å	Rwp
Co_2P/PC	Pnma	a=5.655 b=3.512 c=6.610	2.50	131.257	1.2 %
S-Co_2P/PSC	Pnma	a=5.655 b=3.512 c=6.610	2.72	130.81	0.6 %

Powder X-ray diffraction (XRD) patterns are shown in **Figure 5.1(a,b).** All of the samples show an

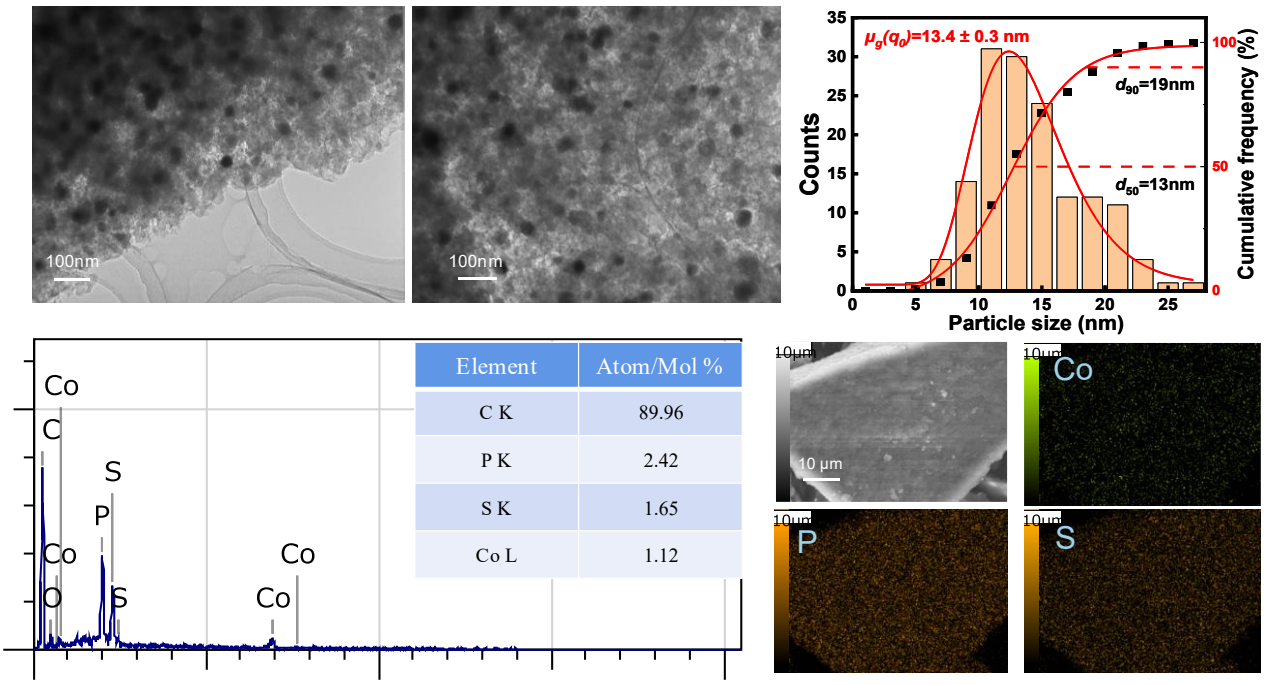

Figure 5.2 TEM images and EDS–SEM elemental compositions of 0.24 S-Co2P/PSC.

amorphous carbon-derived peak was detected at 23-25 °, which confirms the presence of the carbon substrate. All samples exhibited characteristic peaks similar to those of the pure orthorhombic Co2P nanocrystals (Pnma). Sample Co2P/CC shows diffraction peaks at 2θ=40.6 °, 40.7 °,43.1 °, 44 °, 48.6 °, 50.1 o, and 51.9 ° corresponding to the (112), (210), (211), (103), (013), (301) and (020) crystalline surfaces of Co2P(ICSD#624592). The peaks corresponding to (112), (210), (211) and (103) facets of Co2P/PC and 0.24 S-Co2P/PSC were blown up to figure out the influence of adding S. It is noticed that the diffraction peaks of 0.24 S-Co2P/PSC shifted to larger angles, which indicates the reduction of the crystalline lattice. To obtain accurate lattice constants, the samples were scanned at a rate of 1 °/min and the XRD patterns were refined using the Rietveld method. The refinement results are presented in **Figure 5.1(c,d)** and **Table 5.2**. The volume of 0.24S-Co2P/PSC (V=130.81 Å) was decreased by 0.34 % compared to Co2P (V=131.26 Å). This phenomenon may suggest some amount of P (rp=1.30 Å) atoms in the Co2P lattice were replaced by S atoms (rs=1.04 Å).

5.3.2 The morphology and particle distribution of each sample.

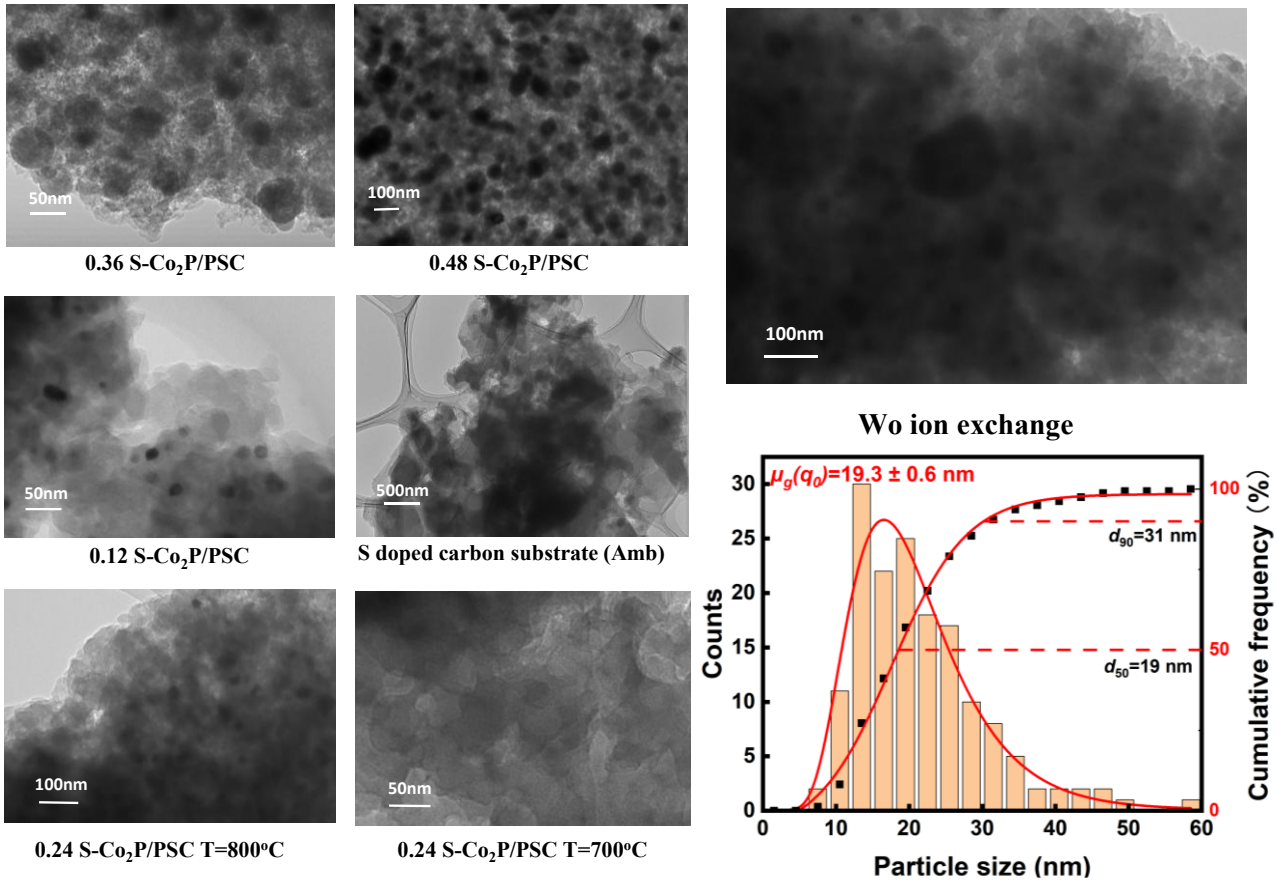

Figure 5.3 TEM images of various samples.

According to **Figure 5.2**, a significant number of nanoparticles with diameters ranging from 5-30 nm (The average particle size =13 nm) were successfully anchored on the surface of the carbon substrate. Combined with the XRD results, these nanoparticles were considered to be S-doped Co2P. Their small size and even distribution are advantageous for exposing active sites, thereby creating favorable conditions for the rapid HER reaction. In order to investigate the effect of the ion exchange process, we compared the particle dispersion of 0.24 S-Co2P/PSC and wo ion exchange. The results were recorded in **Figure 5.3**. When the ion-exchange step was not performed, obvious aggregation occurred in the

Table 5.3 The ICP results the samples.

Sample	Co content (%)	P content (%)
0.24S-Co_2P/PSC	2.9	3.5
Wo ion exchange	1.6	1.5
Co_2P/PC	1.5	1.2

sample. Even though sample wo ion exchange has a smaller loading of Co element, its particle range of the sample expanded compared to 0.24 S-Co_2P/PSC (the average particle size changed from 13 to 19 nm). This result demonstrates the ion-exchange step is effective in immobilizing cobalt species and preventing agglomeration. Besides, as the amount of Co introduced into the precursor increases, the grain size of Co_2P becomes larger. In sample 0.36 S-Co_2P/PSC, the average particle size is approximately 37 nm. In sample 0.48 S-Co_2P/PSC, noticeable grain aggregation is observed. It is also noteworthy that without the ion-exchange step, significant agglomeration was observed in the TEM images. Furthermore, in conjunction with the EDX energy spectrum, the relative atomic contents of P, S, and Co atoms have been determined, which are 2.42, 1.65, and 1.12, respectively. This suggests that P and S elements may not only exist within the Co_2P lattice but also be doped into the carbon substrate. The EDX energy spectrum has also confirmed the even distribution of P, S, and Co elements. This implies the uniform dispersion of Co_2P nanoparticles and the homogeneous doping of P and S elements. In order to gain the catalyst loading, we performed ICP testing on several samples, the results were recorded in **Table 5.3**. For sample 0.24 S-Co_2P/PSC, the loading of Co ions was 2.9%. Although equal amounts of Co and P atoms were added to the precursor, sample wo ion exchange and Co_2P/PC contained less Co than 0.24 S-Co_2P/PSC. This indicates that the sample with only mechanical mixing may anchor fewer cobalt ions.

5.3.3 The identification of chemical composition for each samples using XPS measurements

The X-ray photoelectron spectroscopy (XPS) was carried out to investigate the S doping and the valence states of different elements. According to **Figure 5.4 (a)**, sample 0.24 S-Co_2P/PSC mainly contains carbon, cobalt, sulfur, phosphorus and oxygen, with binding energy peaks at 784.4, 532.6, 284.9, 164.6,133.1 eV corresponding to Co 2p, O 1s, C 1s, S 2p, and P 2p, respectively [40,41]. **Figure 5.4 (b)** shows the Co 2p XPS spectra of 0.24 S-Co_2P/PSC and Co_2P/PC. For sample 0.24 S-Co_2P/PSC, the characteristic peaks located at 782.4eV and 798.4eV are assigned to Co $2p_{3/2}$ and Co $2p_{1/2}$ of cobalt oxide, as they have consistent half-peak widths and their area ratio is close to 2:1. The two satellite peaks located at 786.7 and 804.9 eV originate from the vibrational excitation of high-spin Co^{2+} ions[42]. According to the binding energy manual, the characteristic peak at 778.4 eV is considered to be the Co $2p_{3/2}$ of Co-P in Co_2P[43]. The Co $2p_{1/2}$ of Co-P was not found at the corresponding position for the reason that the catalyst has a certain thickness of carbon layer, yet the XPS could only obtain the surface elements information. The integral area of the characteristic peak originated from Co $2p_{3/2}$ in Co-P is tiny, and the corresponding

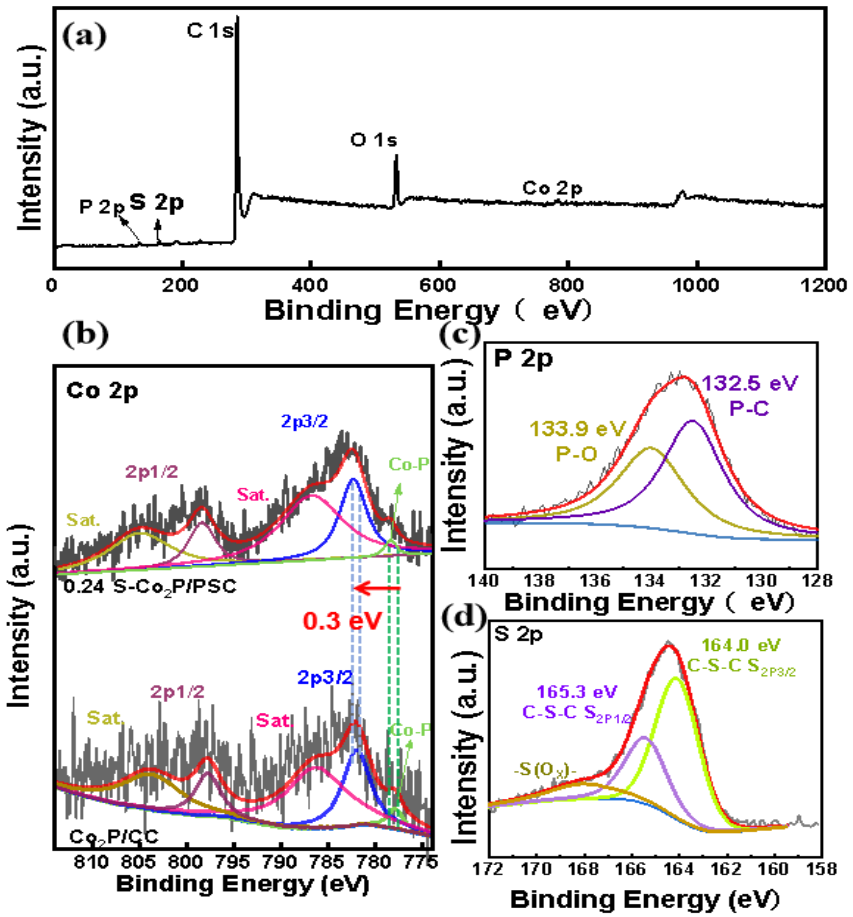

Figure 5.4 The high-resolution XPS spectra of (a) (0.24 S-Co_2P/PSC). (b)Co 2p (0.24 S-Co_2P/PSC and Co_2P/PC) (c)P 2p (0.24 S-Co_2P/PSC) and (d) S 2p (0.24 S-Co_2P/PSC).

characteristic peak of Co $2p_{1/2}$ is even smaller, which makes it impossible for us to identify it in the XPS spectrum. Notably, the binding energy of Co 2p for 0.24 S-Co_2P/PSC exhibits a positive shift compared with Co_2P/PC. Particularly, the Co $2p_{3/2}$ of Co-P in 0.24 S-Co_2P/PSC (778.4 eV) shows a 0.3 eV positive shift compared to that in Co_2P/PC (778.1eV), which indicates the electrons of the Co element are transferred to the doping element [44]. Combined with the volume reduction mentioned in XRD analysis, this result is considered to be strong evidence to prove that the S atoms have been successfully doped into the Co_2P lattice. **Figure 5.4 (c)** shows the P 2p spectrum of 0.24 S-Co_2P/PSC, which could be separated into two subpeaks (132.5 eV for P-C and 133.9 eV for P-O) [45]. It is worth noting that the peak at 132.5 eV for P-C reveals that P atoms were successfully doped into the carbon substrate. The peak at 133.9 eV for P-O was caused by the inevitable oxidation when the sample was exposed to air. It should be noted that no characteristic peaks for Co-P were found in the P 2p spectrum. The P element, which has been detected by XPS mostly exists in the carbon layer, resulting in a weak signal of Co-P bond and therefore it is not shown in the spectrum of P 2p. According to **Figure 5.4 (d)**, the S 2p XPS spectra were divided into three subpeaks located at 164.0 eV, 165.3 eV and 168.9 eV, respectively. The characteristic peaks located at 164.0 eV, 165.3 eV are ascribed to S $2p_{3/2}$ and S $2p_{1/2}$ of -C-S-C-, which proves that the S atoms are successfully doped into the carbon framework [46]. The peak at 168.9 eV was assigned to the -SOx-, which is caused by air oxidation. For the same reason that the characteristic peaks for Co-P were not observed in P 2p XPS spectra, we did not find obvious peaks for Co-S in the XPS spectrum of S 2p.

5.3.4 The HER activity, stability and other electrical measurements of the catalysts

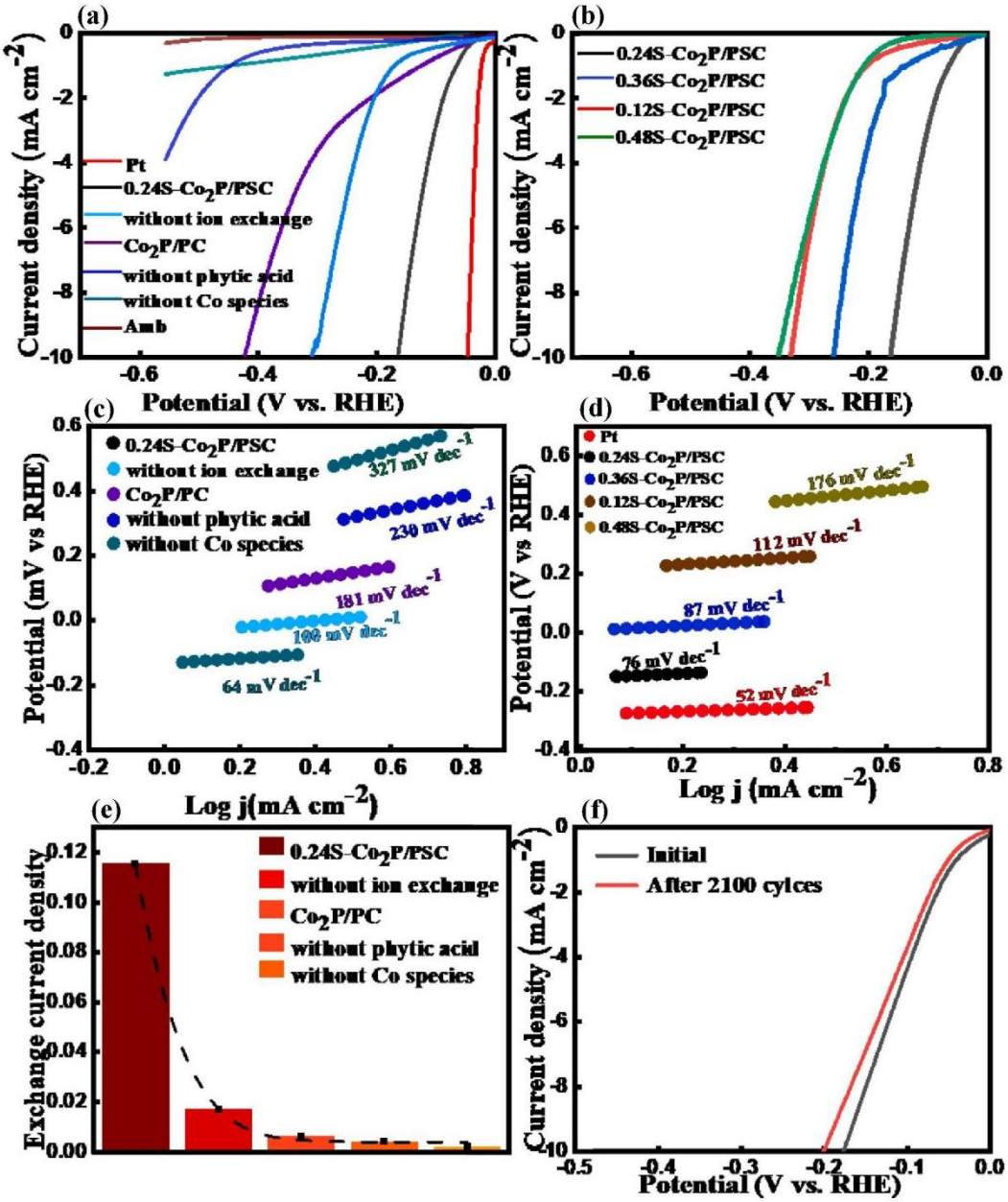

Figure 5.5 (a,b) LSV curves of various samples for HER in 0.5 M H_2SO_4. (c,d) Corresponding Tafel plots.(e)Exchange current density of the various catalysts and (f) LSV curves of 0.24 S-Co_2P/PSC before and after 2100 cycles.

The activity of hydrogen evolution reaction (HER) was measured using a typical three-electrode system consisting of a 0.5 M H_2SO_4 solution. The results were summarized in **Figure 5.5**. To compare, 20 wt% Pt/C electrode was also tested. As shown in **Figure 5.5(a)**, the LSV curves of the samples reveal the superior catalytic activity of the 0.24 S-Co_2P/PSC catalyst with an overpotential (η) of 161 mV to drive a urrent density of 10 mA cm^{-2}.

The 0.24 S-Co_2P/PSC catalyst showed superior catalytic performance compared with the results of previous reports regarding HER over Co_2P-based catalysts. In order to figure out the catalytic mechanism, we examined the fatal species that contribute to the performance of the catalyst. According

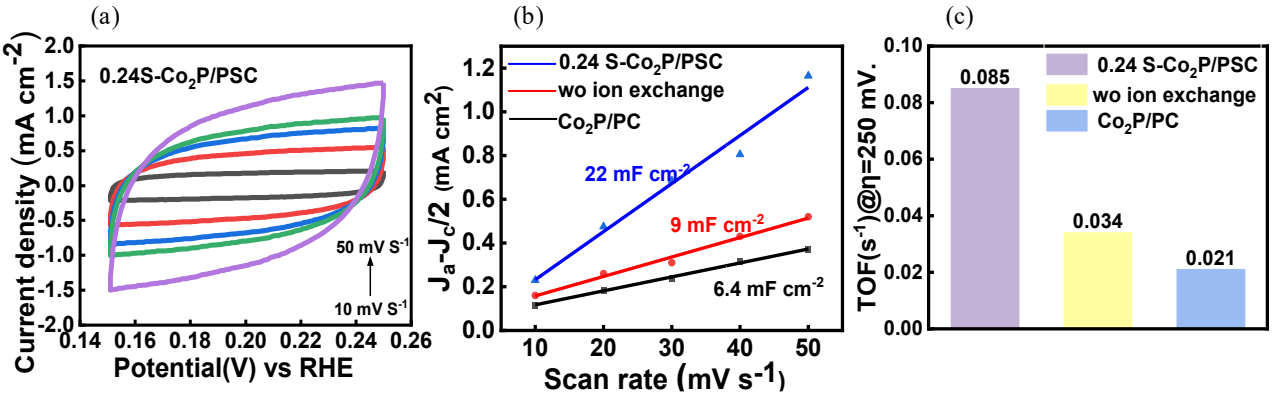

Figure 5.6 (a) CV curves of 0.24 S-Co_2P/PSC in 0.5 M H_2SO_4, (b) electrochemical active surface areas of various samples and (c) Turnover frequency per site at η=250 mV.

Table 5.4 The intrinsic activity of the samples.

Sample	ESCA	TOF*(s^{-1})(η = 250 mV)	j_0*(mA cm^{-2})
0.24S-Co_2P/PSC	550	0.085	0.115
wo ion exchange	225	0.034	0.017
Co_2P/PC	160	0.021	0.006

to **Figure 5.5(a)**, the S-doped carbon substrate as well as the carbon materials co-doped with P and S did not exhibit HER catalytic activity. Moreover, when phytic acid is not added and the Co/Amb precursor is directly pyrolyzed, the sample exhibits poor HER activity. We also noticed that the catalyst has basically no HER activity when the carbonization temperature is below 800 ℃ and there are no particles to be found on the carbon substrate, suggesting that the CoP particles began to form over 800 ℃. These results imply that Co_2P nanoparticles of transition metal phosphides loaded on the carbon substrate serve as the key species providing catalytic sites.

In order to investigate the influence of S dopants, the HER activity of Co_2P/PC was also tested. It is worth noting that the electrocatalytic activity of Co_2P/PC decreases a lot compared with the 0.24 S-Co_2P/PSC, which indicates that the introduction of S species is crucial. The impact of introducing S species on sample performance can be analyzed from two perspectives. Firstly, S atoms possess a higher electronegativity compared to P atoms. When S species replace P atoms within the Co_2P lattice, in order to maintain overall charge conservation, some electrons are transferred from Co sites to S sites. This means the Co sites become more electron-deficient after doping, thereby possessing a more suitable $\triangle G_{H^*}$, which accelerates the kinetics of HER. Secondly, the incorporation of S dopants into carbon support enhances the adhesion strength at the interface between the metal phosphide and the substrate. This is advantageous for the uniform distribution of Co_2P nanoparticles, facilitating rapid mass transport in the HER process. In addition, we found that although the addition of each element in the precursors of 0.24 S-Co_2P/PSC and sample wo ion exchange was consistent, the performance of the

sample without ion exchange steps decreased. This suggests that the ion exchange process could effectively fix the Co species onto the carbon skeleton, expanding the distance between each Co species, and thus limiting the grain reunion. The result is consistent with the phenomenon observed in TEM.
According to **Figure 5.5(b)**, we found that sample 0.24 S-Co_2P/PSC still exhibited the best HER activity, indicating a most suitable Co/P adding ratio. Compared with 0.24 S-Co_2P/PSC, the HER activity of 0.36 S-Co_2P/PSC and 0.48 S-Co_2P/PSC decreased, which may be caused by the aggregation of the nanoparticles. The decline of the activity of sample 0.12 S-Co_2P/PSC may be caused by the lower loading amount of Co_2P. To better understand the catalytic mechanism, we investigated the Tafel slopes of various samples. Based on **Figure 5.5 (c,d)**, the Tafel slope of 0.24 S-Co_2P/PSC is 64 mV/dec, approaching the theoretical value of the Heyrovsky step, indicating the HER process occurred on the surface of the catalyst follows the Volmer-Heyrovsky mechanism. The changing trend of Tafel slope of the as-made catalysts is consistent with the changing trend of HER activity, which again proves our conclusions. The exchange current density (ECD) was also calculated to characterize the intrinsic activity of the catalysts, the related results were recorded in **Figure 5.5 (e)**. Consistent with the results of Tafel slope, sample 0.24 S-Co_2P/PSC has the highest ECD (0.116), again proving its excellent catalytic activity. The stability of 0.24 S-Co_2P/PSC was evaluated by repeated CV sweeps. According to **Figure 5.5 (f)**, a similar LSV curve was obtained after 2100 cycles of CV in the range of 0.3 V to 0.4 V vs. RHE, suggesting the excellent stability of 0.24 S-Co_2P/PSC.
To investigate the intrinsic activities of the catalysts, the electrochemically active surface area (ECSA) of each catalyst was inferred from their double-layer capacitance (C_{dl}), determinable through the cyclic voltammetry (CV). The corresponding turnover frequency (TOF) was also calculated to reveal the intrinsic activity of the catalysts. According to **Figure 5.6**, the C_{dl} value of 0.24 S-Co_2P/PSC is 22 mF cm^{-2}, much better than other catalysts, suggesting the largest exposed active area. It should be noted that although samples without ion exchange and 0.24 S-Co_2P/PSC used the same starting materials with the same mass ratio, its C_{dl} was still much lower than 0.24 S-Co_2P/PSC. This result demonstrates that the ion exchange step could effectively inhibit the migration of Co species, and prevent the agglomeration of Co_2P particles. Thus, the adequate exposure to active sites is ensured. 0.24 S- Co_2P/PSC also has the largest TOF, which is calculated to be 0.085 s^{-1} at η=250 mV. This result is 4 times higher than that of Co_2P/PC (0.021 s^{-1}). The sample without ion exchange showed a larger TOF value (0.034 s^{-1}) than Co_2P/PC. The results indicate that S doping can effectively modulate the electronic structure of the nano-active center, the ΔG_{H^*} of Co sites could be optimized and thus enhancing the intrinsic activity of the catalyst.

5.4 Conclusion

We anchored S-doped Co_2P on a P,S co-doped carbon substrate by ion exchange method. As the cobalt ions were fixed onto the macroporous carbon skeleton, the migration and agglomeration of cobalt species were suppressed. The sintering phenomenon of transition metal phosphides under high temperatures were reduced, ensuring the utmost exposure of active sites. The ESCA of the sample subjected to ion exchange is 2.4 times higher compared to sample subjected to physical mixing only. In addition, the introduction of S species can grab extra electrons from the Co site and regulate the electronic structure of the active center, so that the hydrogen adsorption free energy (ΔG_{H^*}) of the

catalyst is closer to the thermo-neutral state, which improves the HER activity. The TOF (η = 250 mV) fo the sample doping S atoms was elevated from 0.021 s^{-1} to 0.085 s^{-1}, compared to sample without S element, suggesting there is 4-fold increase in intrinsic activity of the catalyst after doping S atoms. Moreover, the co-doping of P, S atoms into the carbon lattice provided the catalyst with excellent electrical conductivity, accelerating both the Volmer and Tafel/Heyrovsky reactions. The best catalyst exhibited outstanding HER activity, with an extraordinarily low overpotential of 161mV at 10 mA cm^{-2} and long-term stability. This method is very facile and the the synthesized catalyst exhibits excellent HER activity, providing a reference for the development of Co_2P-based catalysts.

Reference

[1] Zeng M, Li Y. Recent advances in heterogeneous electrocatalysts for the hydrogen evolution reaction[J]. Journal of Materials Chemistry A, 2015, 3(29): 14942-14962.

[2] Dubouis N, Grimaud A. The hydrogen evolution reaction: from material to interfacial descriptors[J]. Chemical Science, 2019, 10(40): 9165-9181.

[3] Yao J, Huang W, Fang W, et al. Promoting electrocatalytic hydrogen evolution reaction and oxygen evolution reaction by fields: effects of electric field, magnetic field, strain, and light[J]. Small Methods, 2020, 4(10): 2000494.

[4] Sun Z, Hong J, Zhang T, et al. Hydrogen engine operation strategies: Recent progress, industrialization challenges, and perspectives[J]. International Journal of Hydrogen Energy, 2023, 48(1): 366-392.

[5] Morya R, Andrianantenaina F H, Singh S, et al. Exploring rice straw as substrate for hydrogen production: critical challenges and opportunities[J]. Environmental Technology & Innovation, 2023, 31: 103153.

[6] Xu H, Fei B, Cai G, et al. Boronization-induced ultrathin 2D nanosheets with abundant crystalline–amorphous phase boundary supported on nickel foam toward efficient water splitting[J]. Advanced Energy Materials, 2020, 10(3): 1902714.

[7] Aminudin M A, Kamarudin S K, Lim B H, et al. An overview: Current progress on hydrogen fuel cell vehicles[J]. International Journal of Hydrogen Energy, 2023, 48(11): 4371-4388.

[8] Ren J T, Yao Y, Yuan Z Y. Fabrication strategies of porous precious-metal-free bifunctional electrocatalysts for overall water splitting: Recent advances[J]. Green Energy & Environment, 2021, 6(5): 620-643.

[9] Li T, Yin J, Sun D, et al. Manipulation of Mott− Schottky Ni/CeO_2 heterojunctions into N-doped carbon nanofibers for high-efficiency electrochemical water splitting[J]. Small, 2022, 18(13): 2106592.

[10] Chen D, Lu R, Pu Z, et al. Ru-doped 3D flower-like bimetallic phosphide with a climbing effect on overall water splitting[J]. Applied Catalysis B: Environmental, 2020, 279: 119396.

[11] Sun H, Zhang W, Li J G, et al. Rh-engineered ultrathin NiFe-LDH nanosheets enable highly-efficient overall water splitting and urea electrolysis[J]. Applied Catalysis B: Environmental, 2021, 284: 119740.

[12] Wang Y, Yan D, El Hankari S, et al. Recent progress on layered double hydroxides and their derivatives for electrocatalytic water splitting[J]. Advanced Science, 2018, 5(8): 1800064.

[13] Pei Y, Yang Y, Zhang F, et al. Controlled electrodeposition synthesis of Co–Ni–P film as a flexible and inexpensive electrode for efficient overall water splitting[J]. ACS applied materials & interfaces, 2017, 9(37): 31887-31896.

[14] McCrory C C L, Jung S, Ferrer I M, et al. Benchmarking hydrogen evolving reaction and oxygen evolving reaction electrocatalysts for solar water splitting devices[J]. Journal of the American Chemical Society, 2015, 137(13): 4347-4357.

[15] Tsai F T, Deng Y T, Pao C W, et al. The HER/OER mechanistic study of an FeCoNi-based electrocatalyst for alkaline water splitting[J]. Journal of Materials Chemistry A, 2020, 8(19): 9939-9950.

[16] Li Z, Ge R, Su J, et al. Recent progress in low Pt content electrocatalysts for hydrogen evolution reaction[J]. Advanced Materials Interfaces, 2020, 7(14): 2000396.

[17] Liu L, Wang Y, Zhao Y, et al. Ultrahigh Pt-mass-activity hydrogen evolution catalyst electrodeposited from bulk Pt[J]. Advanced Functional Materials, 2022, 32(20): 2112207.

[18] Zhu J, Tu Y, Cai L, et al. Defect-assisted anchoring of Pt single atoms on MoS2 nanosheets produces high-performance catalyst for industrial hydrogen evolution reaction[J]. Small, 2022, 18(4): 2104824.

[19] Li J, Li F, Guo S X, et al. PdCu@ Pd nanocube with Pt-like activity for hydrogen evolution reaction[J]. ACS Applied Materials & Interfaces, 2017, 9(9): 8151-8160.

[20] Luo S, Hei P, Wang R, et al. Facile synthesis of cobalt phosphide nanoparticles as highly active electrocatalysts for hydrogen evolution reaction[J]. Colloids and Surfaces A: Physicochemical and Engineering Aspects, 2020, 600: 124925.

[21] Jia H, Shang N, Chen J, et al. Facile synthesis of N-doped carbon nanoframes encapsulated by CoP nanoparticles for hydrogen evolution reaction[J]. Journal of Colloid and Interface Science, 2021, 601: 338-345.

[22] Wang Z, Shen K, Chen L, et al. Scalable synthesis of multi-shelled hollow N-doped carbon nanosheet arrays with confined Co/CoP heterostructures from MOFs for pH-universal hydrogen evolution reaction[J]. Science China Chemistry, 2022, 65(3): 619-629.

[23] Cai H, Xiong L, Wang B, et al. N-doped CNT as electron transport promoter by bridging CoP and carbon cloth toward enhanced alkaline hydrogen evolution[J]. Chemical Engineering Journal, 2022, 430: 132824.

[24] Men Y, Li P, Yang F, et al. Nitrogen-doped CoP as robust electrocatalyst for high-efficiency pH-universal hydrogen evolution reaction[J]. Applied Catalysis B: Environmental, 2019, 253: 21-27.

[25] Callejas J F, Read C G, Popczun E J, et al. Nanostructured Co_2P electrocatalyst for the hydrogen evolution reaction and direct comparison with morphologically equivalent CoP[J]. Chemistry of Materials, 2015, 27(10): 3769-3774.

[26] Gao Y, Lang Z, Yu F, et al. A Co_2P/WC Nano-Heterojunction Covered with N-Doped Carbon as Highly Efficient Electrocatalyst for Hydrogen Evolution Reaction[J]. ChemSusChem, 2018, 11(6): 1082-1091.

[27] Jin Z, Li P, Xiao D. Metallic Co_2P ultrathin nanowires distinguished from CoP as robust electrocatalysts for overall water-splitting[J]. Green Chemistry, 2016, 18(6): 1459-1464.

[28] Chen S, Xu J, Chen J, et al. Current progress of Mo-based metal organic frameworks derived electrocatalysts for hydrogen evolution reaction[J]. Small, 2024, 20(1): 2304681.

[29] Zhu Z, Luo L, He Y, et al. High-performance alkaline freshwater and seawater hydrogen catalysis by sword-head structured Mo_2N-Ni_3Mo_3N tunable interstitial compound electrocatalysts[J]. Advanced Functional Materials, 2024, 34(8): 2306061.

[30] Li J, Hou C, Chen C, et al. Collaborative interface optimization strategy guided ultrafine RuCo and MXene heterostructure electrocatalysts for efficient overall water splitting[J]. ACS nano, 2023, 17(11): 10947-10957.

[31] Wang M, Ma W, Tan C, et al. Designing Efficient Non-Precious Metal Electrocatalysts for High-Performance Hydrogen Production: A Comprehensive Evaluation Strategy[J]. Small, 2024, 20(14): 2306631.

[32] Chen L, Ren J T, Yuan Z Y. Enabling internal electric fields to enhance energy and environmental catalysis[J]. Advanced Energy Materials, 2023, 13(11): 2203720.

[33] Ma W, Zhang X, Li W, et al. Advanced Pt-based electrocatalysts for the hydrogen evolution reaction in alkaline medium[J]. Nanoscale, 2023, 15(28): 11759-11776.

[34] Men Y, Li P, Zhou J, et al. Tailoring the electronic structure of Co_2P by N doping for boosting hydrogen evolution reaction at all pH values[J]. ACS Catalysis, 2019, 9(4): 3744-3752.Y

[35] Ji X, Chen X, Zhang L, et al. Anchoring nitrogen-doped Co2P nanoflakes on NiCo2O4 nanorod arrays over nickel foam as high-performance 3D electrode for alkaline hydrogen evolution[J]. Green Energy & Environment, 2023, 8(2): 470-477.

[36] Peng X, Yan Y, Jin X, et al. Recent advance and prospectives of electrocatalysts based on transition metal selenides for efficient water splitting[J]. Nano Energy, 2020, 78: 105234.

[37] Xiao W, Liu P, Zhang J, et al. Dual-functional N dopants in edges and basal plane of MoS_2 nanosheets toward efficient and durable hydrogen evolution[J]. Advanced Energy Materials, 2017, 7(7): 1602086

[38] Li H, Yu K, Li C, et al. Charge-transfer induced high efficient hydrogen evolution of MoS_2/graphene cocatalyst[J]. Scientific reports, 2015, 5(1): 18730.

[39] Moroto K, Miyake K, Shu Y, et al. Fabrication of NiSx/C with a tuned S/Ni molar ratio using Ni^{2+} ions and Amberlyst for hydrogen evolution reaction (HER)[J]. International Journal of Hydrogen Energy, 2020, 45(46): 24567-24572.

[40] Gao F, Qu J, Zhao Z, et al. Efficient synthesis of graphene/sulfur nanocomposites with high sulfur content and their application as cathodes for Li–S batteries[J]. Journal of Materials Chemistry A, 2016, 4(41): 16219-16224.

[41] Li X, Zhu X, Li J, et al. Phytic acid-derived Co_2P/N-doped carbon nanofibers as flexible free-standing anode for high performance lithium/sodium ion batteries[J]. Journal of Alloys and Compounds, 2020, 846: 156256.

[42] Natile M M, Glisenti A. Study of surface reactivity of cobalt oxides: interaction with methanol[J]. Chemistry of materials, 2002, 14(7): 3090-3099.

[43] Anjum M A R, Bhatt M D, Lee M H, et al. Sulfur-doped dicobalt phosphide outperforming precious metals as a bifunctional electrocatalyst for alkaline water electrolysis[J]. Chemistry of Materials, 2018, 30(24): 8861-8870.

[44] Wu Y, Liu X, Han D, et al. Electron density modulation of $NiCo_2S_4$ nanowires by nitrogen incorporation for highly efficient hydrogen evolution catalysis[J]. Nature communications, 2018, 9(1): 1425.

[45] Pu Z, Amiinu I S, Kou Z, et al. RuP_2-based catalysts with platinum-like activity and higher durability for the hydrogen evolution reaction at all pH values[J]. Angewandte Chemie International Edition, 2017, 56(38): 11559-11564.

[46] Hu X, Chen S, Chen M, et al. Facile synthesis of nitrogen/sulfur co-doped three-dimensional holey graphene hydrogels for high supercapacitive performance[J]. Energy & Fuels, 2022, 36(12): 6468-6475.

[47] H. J. Cui, H. M. Yu, J. F. Zheng, Z. J. Wang, Y. Y. Zhu, S. P. Jia, J. Jia, Z. P. Zhu. N-Doped graphene frameworks with superhigh surface area: excellent electrocatalytic performance for oxygen reduction. Nanoscale, 2016, 8, 2795–2803.

[48] J.-T. Ren, Z.-Y. Yuan. A universal route to N-coordinated metals anchored on porous carbon nanosheets for highly efficient oxygen electrochemistry. J. Mater. Chem. A, 2019, 7, 13591–13601.

[49] X. Wang, X. Fan, H. Lin, H. Fu, T. Wang, J. Zheng, X. Li. An efficient Co–N–C oxygen reduction catalyst with highly dispersed Co sites derived from a ZnCo bimetallic zeolitic imidazolate framework. RSC Adv., 2016, 6, 37965–37973.

Chapter 6

Undemanding synthesis of N, P co-doped carbon nanosheets for hydrogen evolution reaction: Combining experimental quantitative analysis and DFT calculation corroboration

We developed N, P co-doped carbon-based catalysts based on the crosslinking interaction mentioned in Chapter 4. By modulating precursors concentration, ultrathin heteroatom-doped carbon nanosheets were successfully prepared. Building on this, further optimization of precursor ratios and carbonization temperature yielded a series of products with gradient variations in N and P doping type and content. The synergistic doping mechanisms were investigated through experimental characterization and density functional theory (DFT) calculations. Crucially, for the inherent oxidation susceptibility of the C_3P structure, a synergistic model between C_3PO and nitrogen atoms was first constructed, effectively enhancing the adaptability of the doping system in practical applications.

6.1 Introduction

Hydrogen stands as a promising energy carrier for supplanting fossil fuels in the future[1–5]. It is differentiated into gray, blue, and green hydrogen, depending on its production methods. Of these varieties, green hydrogen, produced via water electrolysis, is acknowledged as the most effective method for reaching carbon neutrality in the future. Nonetheless, this process encounters a

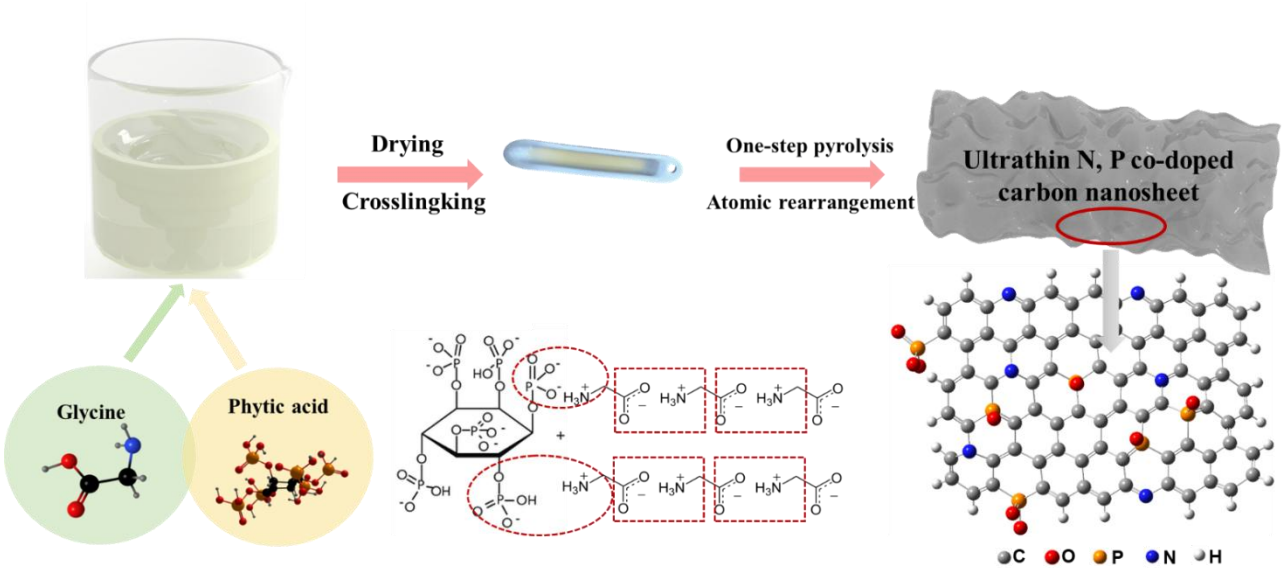

Scheme 6.1 Schematic representation of synthetic method for CNP.

considerable challenge due to the high energy barrier associated with the hydrogen evolution reaction (HER), which significantly hinders progress. Therefore, the development of efficient and cost-effective HER catalysts is urgently needed[6–9]. At present, the leading HER catalysts are categorized into noble metal and transition metal-based catalysts[10–13]. Noble metal catalysts are known for their minimal overpotential yet are limited by their rarity and high cost, rendering them impractical for an economy-driven approach[14–16]. In contrast, transition metal-based catalysts are economic-friendly, but their application for HER is hinders by their low conductivity and tendency to aggregate at elevated temperatures, which compromises their suitability for HER tasks[17,18]. In the realm of hydrogen evolution reaction (HER) catalysts, carbon-based materials have emerged as a focal point of research due to their distinctive advantages. These materials are expected for their adjustable pore structures, which amplify the exposure of catalytic active sites and expedite the transfer of reactant species[19–24]. Additionally, their superior electrical conductivity facilitates rapid electron transfer, while their exceptional corrosion resistance ensures durability in both acidic and alkaline electrolytic environments over prolonged periods. However, a notable challenge with carbon materials is their suboptimal hydrogen adsorption free energy(ΔG_{H^*}), which can impede the efficient adsorption of hydrogen atomsat the active sites[25–29]. Recent advancements suggest that doping carbon materials with heteroatoms can significantly alter the electron cloud density around carbon atoms, thereby potentially optimizing the ΔG_{H^*} towards more favorable conditions[30–35]. Pioneering work by Qu et al[36]. has shown that co-doping carbon materials with heteroatoms not only multiplies the active sites on their surface but also promotes a "cooperative coupling" effect. This synergistic interaction markedly boosts the activity of the carbon-based catalysts. Similarly, Sergio et al[37] utilized P-rich biomass precursor systems to develop P-doped carbon-based catalysts for HER. Their research proposes that the P-C bonds, formed at high carbonization temperatures, could serve as the primary active species facilitating HER. Furthering this line of inquiry, Li et al.[38] crafted N-doped vertical graphene (N-VG) arrays through plasma-enhanced chemical vapor deposition, showing exceptional HER performance. Through a combination of experimental observations and theoretical calculations, they identified that all three forms of N doping (graphitic, pyridinium, and pyrrole) contribute positively to the catalyst's HER activity. This series of studies demonstrates the potential of carbon-based materials to serve as highly efficient and durable HER catalysts.

Despite the potential of carbon materials as robust contenders for HER catalysts, the literature predominantly features transition metal-based catalysts, with non-metallic alternatives being vastly underrepresented. Moreover, among the studies on heteroatom-doped non-metallic catalysts, there is a paucity of detailed examinations into the distinct enhancement mechanisms of various heteroatom species on HER activity, as well as the collaborative effects of dual-heteroatom co-doping. N doping serves as a case, graphitic N, pyridinic N, and pyrrolic N doped in carbon exhibit varied influences on the electron cloud density around neighboring carbon atoms. Such differences necessitate an insight into their density of states, orbital energy level and electron cloud densities to elucidate their doping effect. Apart from that, in the research of P atom doping graphene, most scholars constructed the graphitic P (C_3-P) doping model. However, although the P atoms in graphitic P have high chemical activity, they have high formation energy and are easily oxidized in air. This implies that the preparation conditions of the C_3P structure are harsh and unfavorable for long-term preservation[39]. On the contrast, C_3PO has a lower binding energy, and is more stable compared to C_3P, indicating that

Table 6.1 Mass ratio of starting materials and carbonized temperature.

Sample name	Mass ratio [-]		Carbonized temperature [℃]
	Glycine	50% Phytic acid	
CNP0.2	0.2	0.12	900
CNP0.4	0.2	0.16	900
CNP0.6	0.2	0.24	900
CNP0.8	0.2	0.32	900
NC	0.2	/	900
PC	/	0.16	900
T=600℃	0.2	0.16	600
T=700℃	0.2	0.16	700
T=800℃	0.2	0.16	800
T=900℃	0.2	0.16	900
T=1000℃	0.2	0.16	1000

C_3PO is more likely to exist in P-doped graphene. Since the P atom in C_3PO and C_3P have completely different chemical states, the effect produced by their doping is different. This means that we must include a discussion of C_3PO.

Herein, we developed N, P co-doped carbon-based catalysts by facile one-step pyrolysis process (Scheme 1). Phytic acid, an environmentally friendly and inexpensive biomass raw material with strong chelating ability, was chosen as a P and C source. Glycine was used as a N source because it is economically friendly, easy to dissolve in water, and could crosslink with phytic acid to form a stable N, P co-doped carbon network. The synergistic effects of doping with different heteroatoms were thoroughly investigated by combining experimental results with density functional theory (DFT) calculations. To better understand the effect of N and P species on HER, the catalysts were thus carbonized at different temperatures to modulate the chemical state of N and P in the resultant carbon materials. This approach identified the optimal active components within the catalyst system. Combining X-ray photoelectron spectroscopy (XPS) results and DFT calculations, we found that the C_3PO structure and graphitic N are the key active species in this catalyst. In particular, C_3PO has the most suitable hydrogen adsorption free energy (ΔG_{H^*}=0.13) when it is interstitially doped with graphitic N.

6.2 Experimental

6.2.1 Materials

Glycine, and 50 % phytic acid were purchased from Wako Pure Chemical Industries Ltd. (Osaka, Japan). Pt/C catalyst (20 wt.%), isopropanol and Nafion (5 wt.%) were purchased from Sigma-Aldrich (Saint

Louis, USA). N_2 gas (purity 99.99 %) was purchased from IWATANI FINE GAS Co., Ltd. All reagents were used as received without purification.

6.2.2 Synthesis of CNP

Typically, 0.2 g of glycine and 0.16 g of 50 % phytic acid were dissolved in 1 mL of deionized water. The mixture was then dried at 90 °C for 2 h to form the C/N/P solid precursor. Other samples with different amounts of N and P were also synthesized using the same procedure. The other detailed proportions of raw materials are listed in **Table 6.1**. The as-made precursor was placed in a tube furnace and heated to 900 °C with a ramp of 5 °C /min and kept for 3 h under N_2 flow (60 ml/min). The product was denoted as "CNP0.4", where 0.4 represents the added ratio of phytic acid to glycine. We also prepared CNP0.4 at different carbonation temperatures to investigate the structural and changes in heteroatom-doped carbon layers during carbonization processes.

6.2.3 Characterizations

The morphology was conducted by transmission electron microscopy (TEM, Hitachi H800). The atomic force microscope (AFM) was used to check the thickness of the nanosheets. The mass ratio of carbon and P was investigated using energy-dispersive X-ray spectroscopy (EDX). The N content was measured using elemental analyzers (CHN, Perkin Elmer 2400IICHNS/O). Powder X-ray diffraction (XRD, RINT2200 with Cu Kα radiation) was used to determine the structure of the carbon layers. The element doping and valence states were evaluated using XPS (JEOL JPS-9000MX) with Mg Kα as the energy source. Raman spectra of the samples were recorded using a confocal Raman microscope (LabRAM HR-800, Horiba, Ltd., Kyoto, Japan).

6.2.4 Electrochemical measurements

To evaluate the hydrogen evolution reaction (HER) activity of the samples, we employed an ALS 2325 bi-potentiostat equipped with a standard three-electrode system. Hg/Hg_2Cl_2 served as the reference electrode for the 0.5 M H_2SO_4 electrolyte, while a graphite rod functioned as the counter electrode. To prepare the working electrode, the following procedure was followed: 8 mg of catalyst powder was dispersed in a solution containing 1 ml of isopropanol, 5 wt% Nafion, and deionized water ($V_{isopropanol}$: V_{Nafion}: $V_{Deionized\ water}$ = 1:1:8). The mixture was ultrasonicated to obtain homogeneous catalyst ink. Subsequently, a suspension (4 μg) of the catalyst ink was evenly coated onto a carbon cloth (with an area of 0.1256 cm^2) of a rotating ring-disk electrode, forming a thin and uniform carbon layer. The working electrode was thoroughly dried under ambient conditions for 30 min to complete its preparation.

To assess the HER activity of the samples, linear sweep voltammetry (LSV) was conducted at a sweep rate of 5 mV s^{-1} and a rotation speed of 1600 rpm under a N_2 flow at 80 mL/min. The electrochemical impedance spectroscopy (EIS) measurements were recorded in the frequency range from 200,000 to 10 Hz.

6.2.5 DFT calculation

The Density functional theory (DFT) calculations were performed using Gaussian 16W. The B3LYP

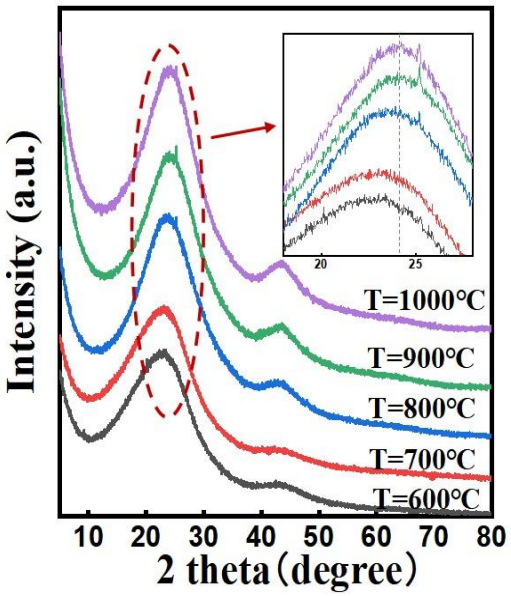

Figure 6.1 The XRD patterns of the various samples.

hybrid density functional in combination with the 6-31g(d,p) and the dispersion correction (keywords: em = gd3bj) were used. The basis set was used in the calculations because it has been shown to be a reliable approach for this type of organic chemical reaction.

6.3 Results and discussion

6.3.1 The analysis of crystalline phases for each sample by using XRD measurements

The XRD patterns of the N, P co-doped carbon materials synthesized at different temperatures are shown in **Figure 6.1**. All samples exhibit an XRD pattern with a broad (002) diffraction peak centered at around 2θ = 23◦ (Amorphous carbon peak) and a (101) diffraction broad peak appears centered at around 2θ = 43◦, which relates to the formation of graphitic domains in the carbon structure. The enhancement of the signals at two peaks is attributed to the increased graphitization of the carbon material, which leads to a more orderly arrangement of carbon atoms. Additionally, we observed that with the increase in temperature, both diffraction peaks shift towards higher angles, indicating a contraction in the carbon lattice volume. We believe this may be influenced by two factors. Firstly, as the heat treatment temperature increases, the degree of graphitization of the carbon material increases, leading to changes in the binding structure and a decrease in the interlayer spacing of the carbon lattice. Secondly, with the rise in temperature, the total doping amount of N and P atoms decreases, resulting in a reduction in the volume of the carbon lattice. Furthermore, when the carbonized temperature is over 800 °C, small but sharp diffraction peaks were detected at around 2θ = 25◦, which is related to the sp^2 hybridized carbon, suggesting an increasing number of C=C bonds[40]. To obtain more penetrating insight into the variation of the interlayer spacing within carbon materials, we have executed a quantitative analysis of the lattice constant for samples prepared under disparate carbonization temperatures. As the temperature ascends, the interlayer spacing of carbon materials manifests a descending tendency, thereby corroborating that the graphitization degree of the catalyst escalates synchronously with the increasing temperature. It is noteworthy that there is a marginal difference in

Table 6.2 The CHN results of the various samples (mass ratio).

Temperature	**C[%]**	**N[%]**	**N/C**
T=600℃	45.07	16.85	0.37
T=700℃	45.26	17.14	0.38
T=800℃	52.19	6.75	0.13
T=900℃	59.6	3.33	0.56
T=1000℃	68.33	2.26	0.033
Ratio	**C[%]**	**N[%]**	**N/C**
CNP0.2	66.53	2.73	0.041
CNP0.4	59.6	3.33	0.056
CNP0.6	55.46	3.4	0.063

the interlayer spacing between sample T=900 ℃ and T=1000 ℃, which might be imputed to the insertion of oxygen atoms under high temperature ambience.

6.3.2 The analysis of elements amount for each sample by using CHN measurements

Table 6.2 lists the changes in N content in the products under different temperatures and raw material mixing ratios According to the CHN analysis results, the N content in the products decreases with an increase in temperature. This could be due to the competitive reaction between the formation of C=C bonds and C-N bonds. Pyrolysis at high temperatures induces structural changes in carbon materials, where an increase in temperature leads to the transformation of defective carbon structures into sp^2 hybridized carbon atoms, forming regular hexagonal ring graphite structures. Therefore, at high temperatures, the formation of C=C bonds is favored, and the inner N atoms gradually eliminate leading to a decrease in the overall N content of the material. Additionally, in conjunction with the XRD patterns, when the heat treatment temperature is between 600-900 ℃, the interlayer spacing of the carbon lattice becomes narrower with increasing temperature. Notably, when the amount of phytic acid added increases, the doping level of N elements in the product actually increases.

Table 6.3 Height distributions of CNP0.4 at the scale of nanometers.

Area	**Average height (nm)**	**Maximum height (nm)**	**Surface area (nm^2)**
Polygon 1	1.9	2	20300
Polygon 2	1.3	1.6	8568
Polygon 3	0.8	1.2	21400
Polygon 4	1.8	2	17860
Polygon 5	2.4	2.6	30104

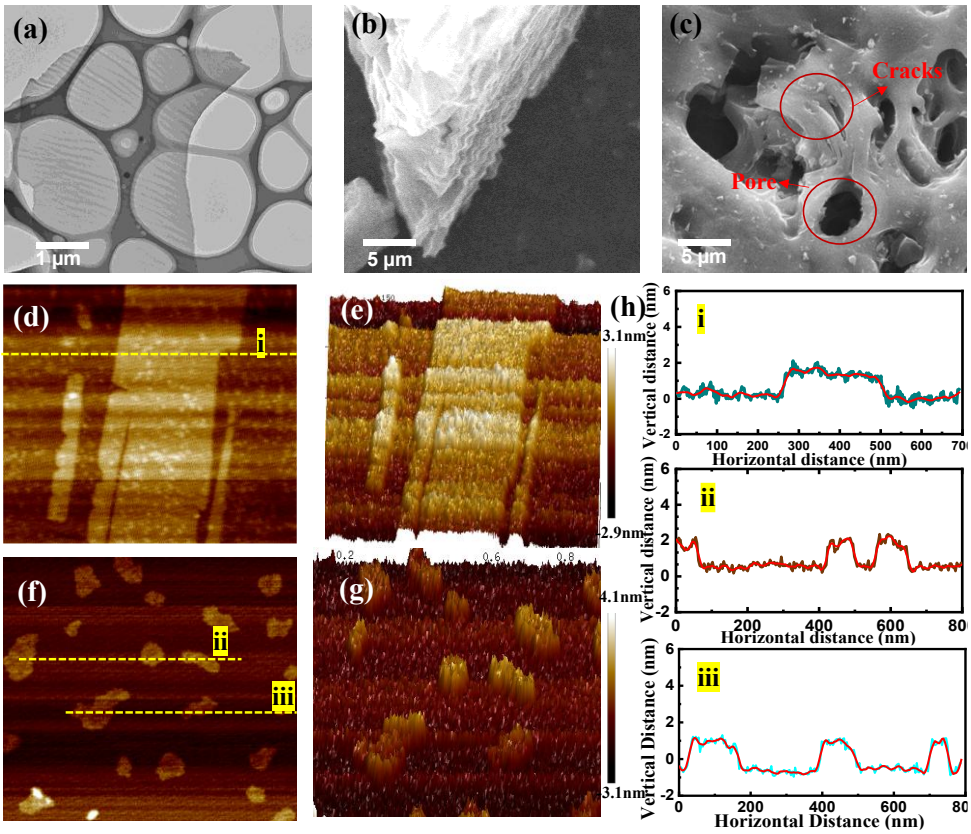

Figure 6.2 (a) The TEM image of sample CNP0.4. (b) The SEM image of sample CNP0.4 from the side view. (c) The SEM image of sample CNP0.4 from the top view. (d) AFM image of CNP0.4 at micro meter scale and (e) The corresponding 3D height distribution. (f) AFM image of CNP0.4 at nano meter scale and (g) the corresponding 3D height distribution. (h) The height of line i,ii and iii in AFM images.

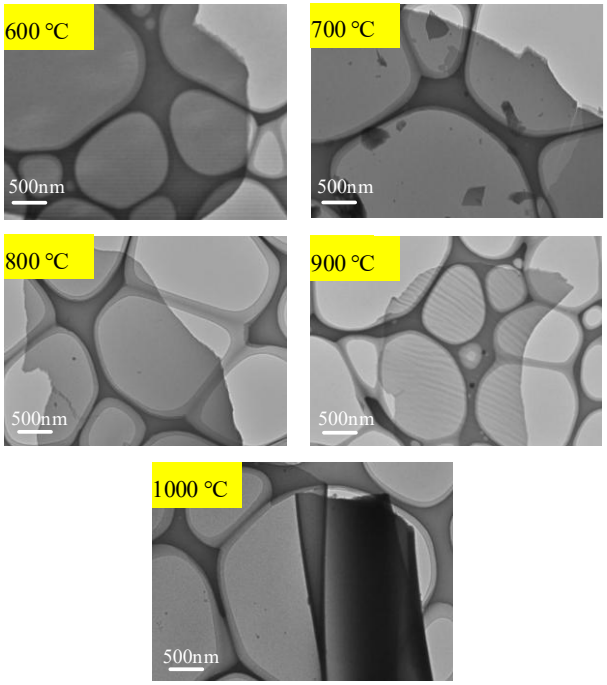

Figure 6.3 TEM images of the various samples.

Figure 6.2 displays the morphology of CNP0.4. According to **Figure 6.2**(a), the homogeneous carbon nanosheets were successfully synthesized. The SEM images were obtained and **Figure 6.2** (b) shows a side view of the carbon block, which reveals that the sample consists of stacked layers of nano-meter-sized sheets in the undispersed state. From the top view of the carbon block, channels with diameters ranging from 1 μm to 5 μm were observed. Additionally, some surface cracks were found, indicating the presence of tensile stress within the carbon layers. The numerous channels formed on the surface of the carbon block are due to the decomposition of phytic acid at high temperatures. The phosphoric acid will generate, which has a certain activating effect on the carbon materials. To verify this, the sample with different added phytic acid amount and various heating temperatures were tested using SEM. According to **Figure 6.3**, it was observed that as the added amount of phytic acid increased, the number and size of the surface pores on the carbon block also increased. Moreover, no pores were present on the sample surface at 700 °C. As the temperature increased, no significant changes in the surface pores were observed. Combined with the result of CHN, the increasing amount of added phytic acid will enhance the activation effect of phosphoric acid and make the carbon atom content decrease. The ultra-thin carbon layer ensures adequate exposure of active sites, allowing rapid transfer of electrons and species, enhancing the HER activity of the catalyst.

The AFM images were carried out to investigate the thickness of the carbon layer. The results were recorded in **Figure 6.2**(d,f) and **Table 6.3**. We found that the thickness of all nanoplates in **Figure 6.2**(d,f) and **Table 6.3** is no more than 2 nm, and the aspect ratios (area-to-thickness) are more than 4000:1, confirming the formation of nanosheet. To verify the uniformity of nanosheet thickness distribution in CNP0.4, we plotted the cumulative distribution frequency curve of thickness. In samples with a

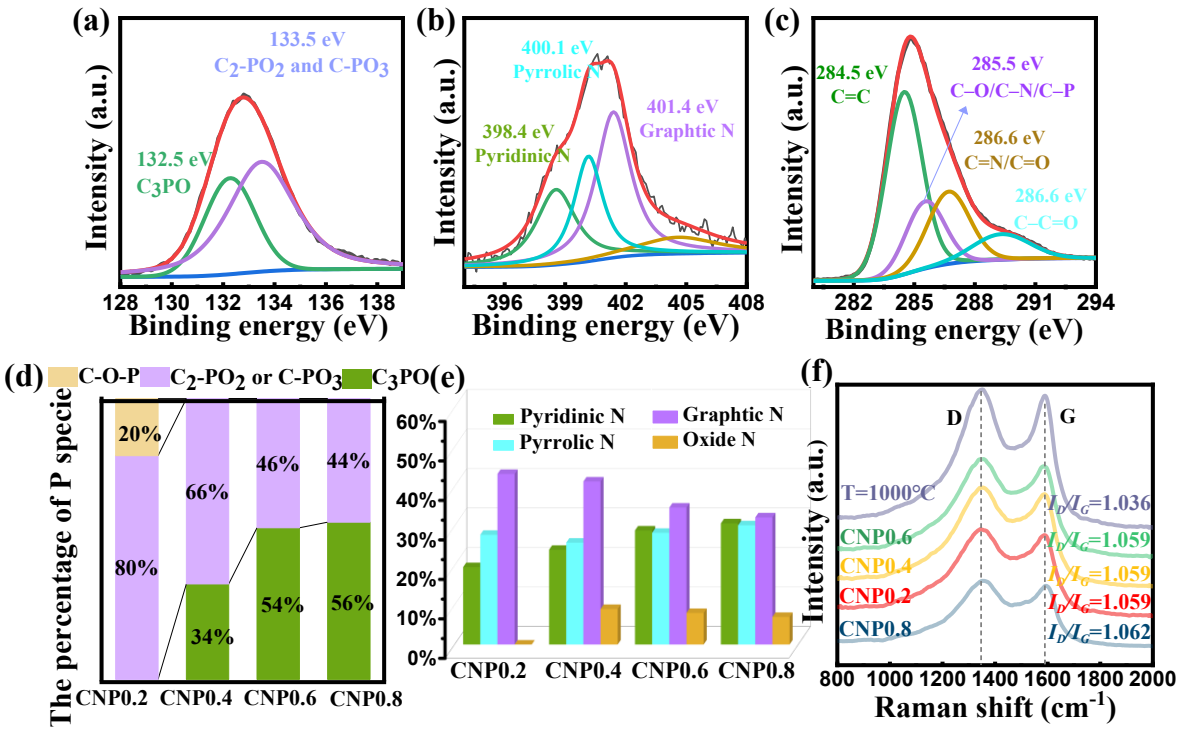

Figure 6.4 (a) The P 2p spectrum of CNP0.4. (b) the N 1s spectrum of CNP0.4. (c) the C 1s spectrum of CNP0.4. (d) The P species percentage of CNP0.2, CNP0.4, CNP0.6 and CNP0.8. (e)The N species percentage of CNP0.2, CNP0.4, CNP0.6, CNP0.8 and (f) Raman spectra of various samples.

diameter of less than 800 nm, 90% of the nanosheets had a thickness below 2.4 nm, and 50% had a thickness below 1.9 nm.

6.3.3 The identification of chemical composition for each samples using XPS measurements

Figure 6.4(a) shows the P 2p spectrum of CNP0.4, which could be separated into two subpeaks (132.5 eV for C_3-PO and 133.5 eV for C-PO_3 or C_2PO_2)[41–44]. It is worth noting that the peak at 132.5 eV for C_3PO reveals that P atoms were successfully doped into the carbon skeleton and replaced some carbon atoms. The peak at 133.5 eV for C-PO_3 or C_2PO_2 represents the bonding of P atoms with edge carbon. To investigate the effect of different added phytic acid amount on the chemical state of doped P, we compared the changes in the C_3PO content of the product at different raw materials ratios. As shown in the **Figure 6.4** (d), the percentage of C_3PO in the product increased when the amount of phytic acid increased. In contrast, the percentage of C_2-PO_2 and C-PO_3 decreases at high phytic acid concentrations, suggesting the promoted conversion of C-O-P, C_2-PO_2 and C-PO_3 bonds to C_3PO bonds at high phosphate molecule concentrations. Furthermore, the percentage of different P species in the samples were also investigated. C_2PO_2 and C-PO_3 were the main P species presented when the heating temperature was 700 °C. The C_3PO structure appeared at 800°C and its content increased with increasing temperature. When the heating temperature exceeds 1000 °C, C_2PO_2 and C-PO_3 are converted to more highly valent oxides. The N 1s spectrum can be decomposed into three types of N atoms, as shown in **Figure 6.4** (b). Graphitic N (401.4 eV), pyrrolic N (400.1 eV), and pyridinic N (398.4 eV)45. This result confirmed that almost all N species were incorporated into the carbon skeletons. To investigate the effect of different added phytic acid amount on the chemical state of doped N, we compared the change of N species content in the products at different raw materials ratios. As shown in the figure, the percentage of pyridinic N in the product increase when the addition of phytic acid increases, which may imply the activation of phytic acid led to the appearance of more edge sites in the carbon material, resulting in the transformation of graphitic N into pyridinic N. Moreover, the variations in the contents of N species during different carbonization temperature processes were documented to determine their high temperature stability. We found that the pyridinic N and pyrrolic N content decrease under high temperature while graphitic N content increase. This result reveals that pyridinic N and pyrrolic N display suboptimal stability under high temperatures. They are inclined to migrate towards the interior of the carbon layers and will convert into graphitic N. When the temperature reaches 900 °C, NOx species start to emerge. When the temperature reaches 1000 °C, the pyrrolic N is predominantly converted into NO_x species[46]. In conjunction with XRD results, the carbon materials exhibit a certain degree of oxidation at 1000 °C, accompanied by an increase in the lattice spacing.

To investigate the carbon crystallinity of the catalyst using different phytic acid/glycine ratio, we have carried out Raman spectra for various samples. According to **Figure 6.4** (f), all samples contain typical D and G bands at 1347 and 1589 cm^{-1} [47]. The I_D/I_G ratios of various samples were calculated to figure out the carbonized degree of the products. For the samples carbonized under 900 °C, their I_D/I_G ratios are all close to 1.06. This suggests similar graphitization levels of the samples carbonized under 900 °C, excluding any influence of different graphitization levels in these samples. However, the catalyst carbonized at 1000 °C exhibit a higher I_D/I_G ratio than the samples carbonized at 900 °C, suggesting its higher graphitization degree.

6.3.4 The HER activity, stability and other electrical measurements of the catalysts

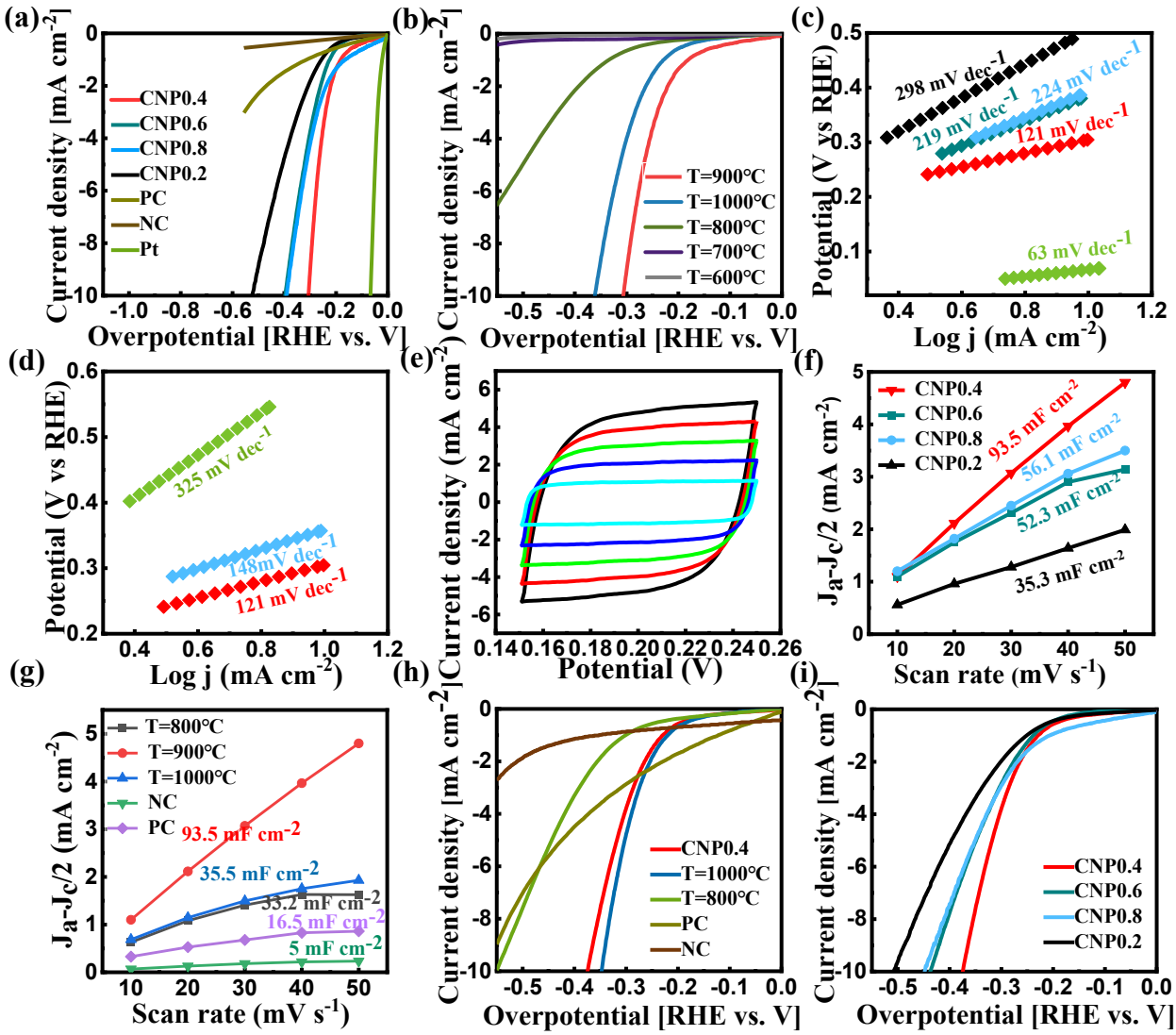

Figure 6.5 (a,b) The LSV curves of the various samples. (c,d) The corresponding tafel slopes. (e) The CV curves of CNP0.4 in 0.5M H_2SO_4 with the sweep rate changed from 10 mV s^{-1} to 50 mV s^{-1}. (f) The ESCA of sample CNP0.2, CNP0.4, CNP0.6 and CNP0.8. (g) The ESCA of sample T=800 ℃, 900 ℃, 1000 ℃, PC and NC. (h) The normalized current density of sample T=800 ℃, 900 ℃, 1000 ℃, PC and NC. (f) The normalized current density of CNP0.2, CNP0.4, CNP0.6 and CNP0.8.

The activity of hydrogen evolution reaction (HER) was measured using a typical three electrode system consisting of a 0.5 M H_2SO_4 solution. The results were summarized in **Figure 6.5**. To compare, 20 wt% Pt/C electrode was also tested. In order to figure out the catalytic mechanism, we examined the fatal species that contribute to the performance of the catalyst. According to Fig. 4(a) and Table S5, the P-doped carbon as well as the N-doped carbon did not exhibit HER catalytic activity, implying that the HER activity of the catalyst derives from the synergistic promotion of N, P atoms. To be continued, we investigate the HER activity of the samples heated at different temperatures. As shown in **Figure 6.5** (b), the performance of the catalyst increases first and then decreases with the increasing carbonization temperature. When the carbonization temperature is 900 °C, the catalyst exhibits the best activity, with an overpotential (η) of 306 mV to drive a current density of 10 mA cm^{-2}, which is much closer to

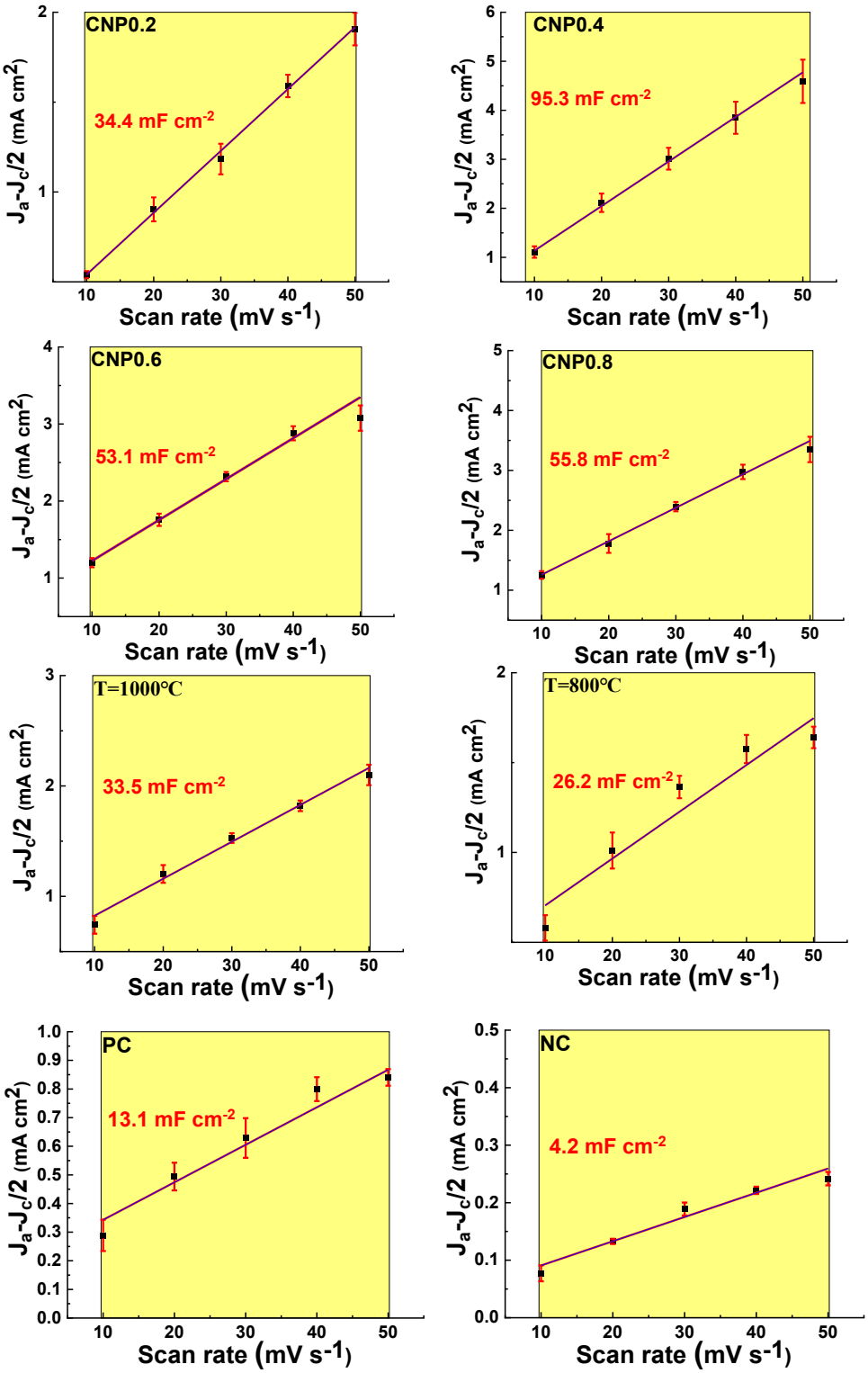

Figure 6.6 Error bars of the ESCA of three independent samples.

the activity of commercial Pt/C catalyst than other catalysts.

The increase in catalyst performance up to 900 °C could be attributed to the increasing graphitization degree of the carbon materials and the increasing percentage of C_3PO. When the temperature is higher than 900 °C, the HER performance decreases despite the higher graphitization degree at the elevated temperature. This is probably due to the aggregation of carbon nanosheets under high temperature. In

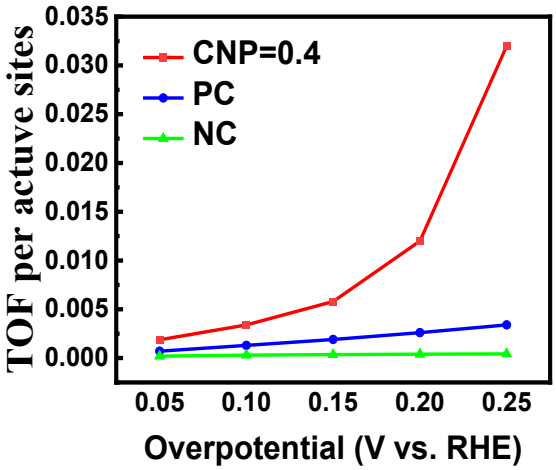

Figure 6.7 TOF per active sites of sample CNP0.4, PC and NC.

addition, we noticed that samples with carbonation temperatures below 800 °C are not catalytically active. Combined with XPS, we found that C_3PO is generated at 800 °C, which suggests C_3PO may be the key species providing HER activity. To verify the changing trend of HER performance of samples at different carbonization temperatures, we carbonized samples with other glycine/phytic acid ratios at different temperatures. By comparison, we found that regardless of the ratio of the starting materials, the correlation between the HER performance and the carbonization temperature is similar. In addition, we investigated the effect of the added amount of phytic acid on catalyst performance. We found that the performance of the catalyst increased and then decreased with the increasing amount of phytic acid. Combined with CHN results, we found that the total concentration of both N and P atoms increased with the increase of phytic acid incorporation. Although samples CNP0.6 and CNP0.8 have greater N, P content, their HER activities are still lower than that of sample CNP0.4. This result implies that the total N, P elemental content is not a decisive factor for HER activity. Combined with XPS, we suggest that the determining factor is the percentage of different N and P species. According to **Figure 6.5** (a), the P-doped carbon, as well as the N-doped carbon did not exhibit HER catalytic activity, implying that the HER activity of the catalyst derives from the synergistic promotion of N, P atoms. This result implies that the total N, P elemental content is not a decisive factor for HER activity. Combined with XPS, we suggest that the determining factor is the percentage of different N species (graphitic N, pyridinic N and pyrrolic N) and different P species (C-O-P, C_2PO_2, C_3PO and C-PO_x). According to **Figure 6.4**(a), we found that as the phytic acid concentration increased, the percentage of graphitic N, pyridinic N, C_3PO and C_2PO_2 showed a monotonically increasing or monotonically decreasing trend while the performance of the catalysts is not monotonically increasing or decreasing. We believe that there are at least two active species. Since samples CNP0.4, CNP0.6 and CNP0.8 had similar percentages of nitrogen oxide, we excluded the possibility of nitrogen oxide. The content of pyrrolic N and C_2PO_2 is highest in CNP0.2, but they do not exhibit good HER activity, which means that pyrrolic N and C_2PO_2 do not have a good synergistic effect. In addition, in samples CNP0.4, CNP0.6, and CNP0.8, the content of pyrrolic N and C_3PO increased monotonically. However, the HER activity of these three samples monotonically decreases, so we believe that these two structures do not exhibit a good catalytic synergy effect, either. In addition, we found no C-O-P bond in samples CNP0.4, CNP0.6 and CNP0.8, which implies that C-

O-P is also not a key active component. In summary, we believe that there are two possibilities for an optimal synergistic system: (1) graphite N and C_3PO (2) Pyridinic N and C_2PO_2.

To better understand the catalytic mechanism, we investigated the Tafel slopes of various samples. Based on **Figure 6.5** (c), the Tafel slope of CNP0.4 is 121 mV/dec, approaching the theoretical value of the Heyrovsky step, indicating the HER process follows the Volmer-Heyrovsky mechanism. The changing trend of Tafel slope of the as-made catalysts is consistent with the changing trend of HER activity, which again proves our conclusions. It is noteworthy that although sample CNP0.6 and sample CNP0.8 have similar overpotentials, sample CNP0.6 exhibits a lower tafel slope, which implies that CNP0.6 has superior catalytic activity compared with CNP0.8.

To investigate the intrinsic activities of the catalysts, the electrochemically active surface area (ECSA) of each catalyst was inferred from their double-layer capacitance (Cdl), determinable through the cyclic voltammetry (CV). According to **Figure 6.5** (f), the Cdl value of CNP0.4 is 93.5 mF cm^{-2}, much better than other catalysts, suggesting the largest exposed active area. The large active surface area provides a terrific basis for promoting HER. The excellent HER performance of this sample can be clearly proved by comparison with other reported carbon materials. However, when the heat treatment temperature is 1000 °C, the active surface area is reduced, which might be caused by the agglomeration under high temperatures or the decreases in the content of the active species within the catalyst. To be continued, P-doped carbon materials have a larger active surface area than N-doped carbon materials, which are 16.5 mF cm^{-2} and 5 mF cm^{-2} respectively. The error bars of ESCA over 3 separately prepared samples were also tested to reflect the variability in the measurements. According to **Figure 6.6**, the revised ESCA of CNP 0.2, CNP0.4, CNP0.6, CNP0.8, T=1000°C, PC and NC are 34.4 mF cm^{-2}, 95.3 mF cm^{-2}, 35.5 mF cm^{-2}, 33.2 mF cm^{-2}, 33.5 mF cm^{-2}, 13.1 mF cm^{-2} and 4.2 mF cm^{-2}, respectively. Upon comparison with other literatures, we found that the catalysts prepared by this economical and

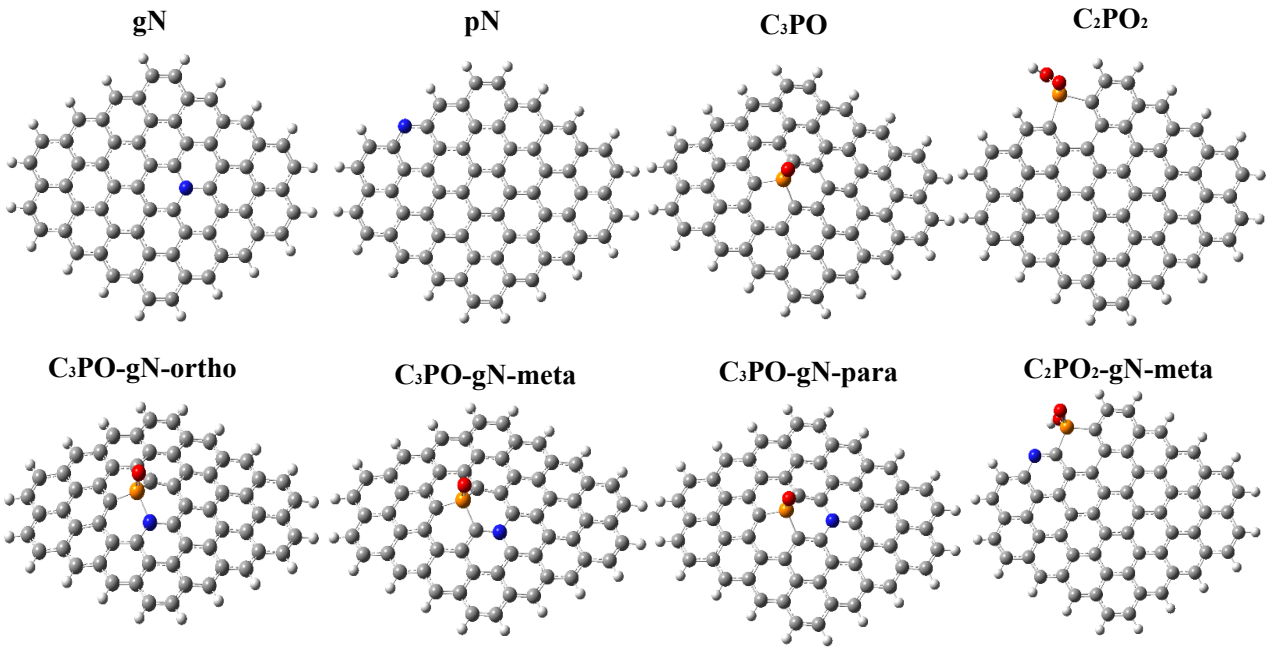

Figure 6.8 8 optimized models for the heteroatoms doped graphene.

convenient synthesis method exhibited outstanding active surface area compared to other carbon materials with special structure (CNT, nanosheet and Plasma-etched graphene).

To investigate the N, P co-doped effect on active sites, we studied the Turnover frequency (TOF) of CNP0.4. As a comparison, the TOF of PC and NC were also calculated and the results were recorded in Fig S13. We found that N and P co-doping can effectively change the ΔG_{H^*} of the active sites. According to **Figure 6.7**, the N, P co-doped samples exhibited far more catalytic activity than PC and NC. When the overpotential is 250 mV, its TOF was 9 times higher than that of PC and 64 times higher than NC. In comparison, PC has a larger active surface area and better intrinsic activity than NC. This implies that the P atoms adjust the electronic structure of the carbon material more efficiently.

6.3.5 DFT calculations

The DFT model was used to explore the role of each component of the N, P co-doped carbon material in the modulation of the graphene electron cloud as well as to analyze the role of different potential sites that may be present on the surface of doped graphene in the HER. The spatial structure as well as

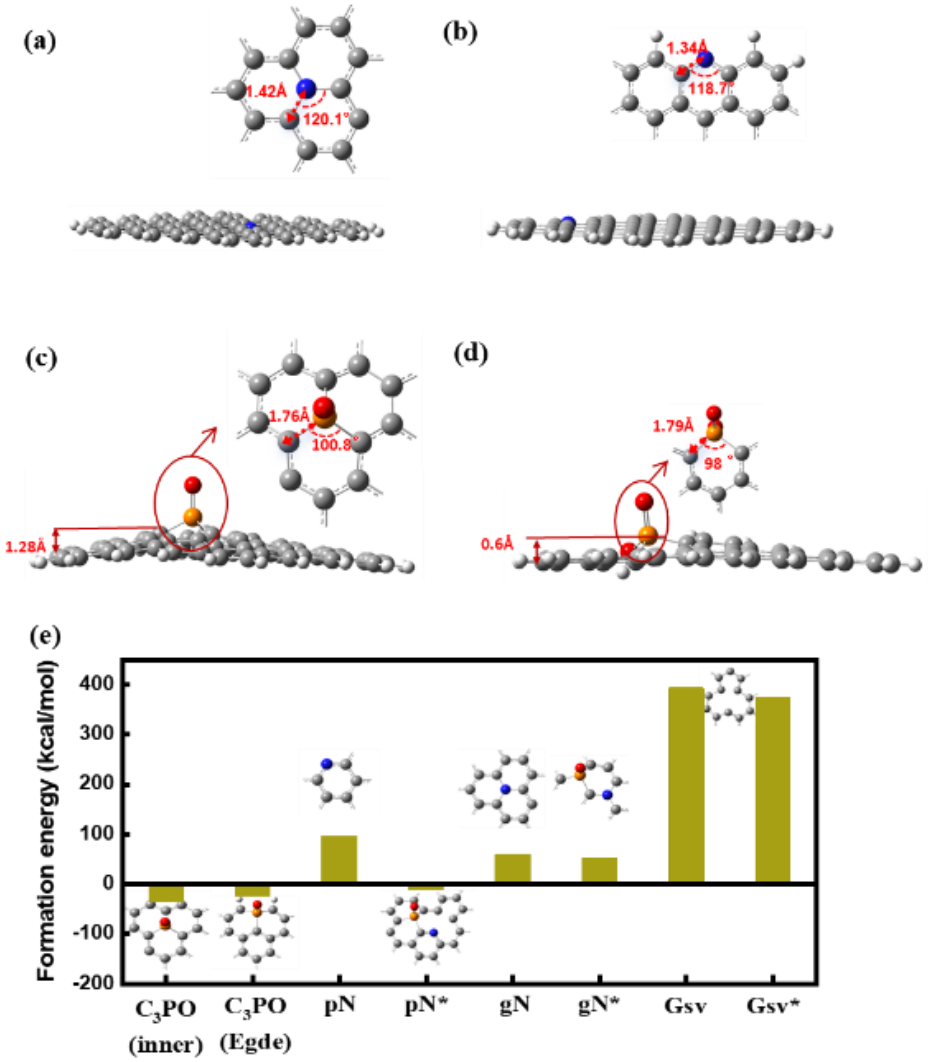

Figure 6.9 (a)Optimized models for graphitic N doped graphene. (b) Optimized models for pyridinic N doped graphene. (c) Optimized models for C_3PO doped graphene. (d) Optimized models for C_2PO_2 doped graphene. (e) The formation energy of the various structures. * represents the generation energy of the structure in the presence of C_3PO.

the electronic structure of doped graphene was investigated using a clustering model. The examined graphene surface was constructed with 23 benzene rings including 64 carbon and 20 hydrogen atoms. The 84 atoms of graphene ensure that the dimensions of the model are adequate to avoid excessive edge effects that can cause the results to deviate significantly from the actual values. The terminal H atoms were fixed to avoid interactions like those that may occur in a periodic that may occur in a periodic model of plane-wave coding and focus on the chemical interaction and electron transfer at the active site ensemble. All atoms are set to allow relaxation in order to optimize the structure.

Combining the results of XPS and LSV, we believe that the enhancement effect of N, P co-doped graphene should be due to the synergistic effect of C_3PO & graphitic N or C_2PO_2 & pyridinic N. Therefore, we focus on these two co-doping models. In order to better deconstruct the contribution of each component to the overall catalytic active species we also constructed four single atom doping models, GN (Graphitic N doped graphene), PN (Pyridinic N doped graphene), C_3PO-G and C_2PO_2-G, respectively. For the possible doping sites and geometry of heteroatom-doped graphene, we calculated the formation energies of the C_3PO structure at the edges of graphene and the C_3PO structure inside graphene to confirm the main doping site of P (**Figure 6.9** (e)). By comparison, we found that two energies are very close to each other, which means that both structures can exist stably. Since we used in-situ doping method and the prepared samples are 2D structures, we think it is more general to explore the C_3PO structure inside graphene[48]. The C_2PO_2 structure has a large spatial structure, which makes it difficult to exist stably inside the carbon lattice,

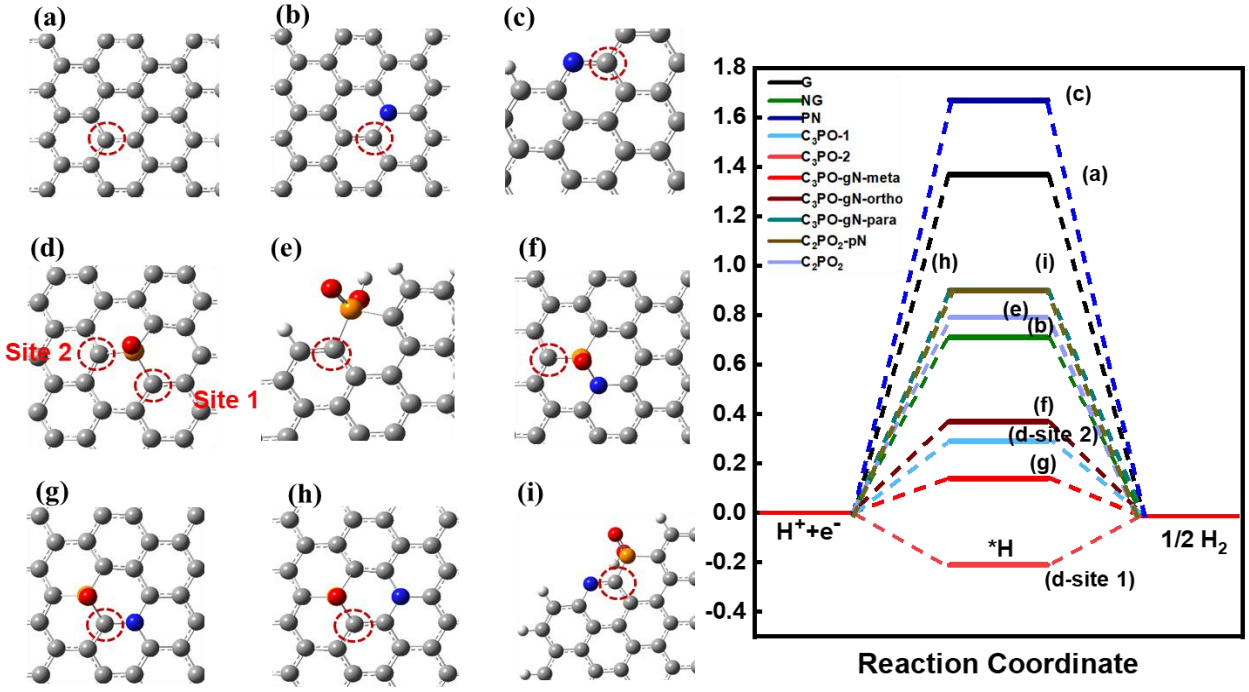

Figure 6.10 ΔG_{H^*} of (a) Graphene(G), (b) Graphitic N (NG), (c) Pyridinic N (PN), (d) Graphene doped with C_3PO, (e) Graphene doped with C_2PO_2 (f) Graphene doped with C_3PO and graphitic N in ortho site(C_3PO-gN-ortho). (g) Graphene doped with C_3PO and graphitic N in meta site(C_3PO-gN-meta). (h) Graphene doped with C_3PO and graphitic N in para site(C_3PO-gN-para). (i) Graphene doped with C_2PO_2 and graphitic N (C_2PO-pN).

so we focused on the C_2PO_2 structure at the edges of graphene. It should be noted that the P-N bond was not detected in XPS, thus the C_3PO-gN-ortho structure may not exist in the catalyst. However, we have included this configuration for the purpose of discussing the synergistic effect of the N and P atoms. The following are the eight models mainly discussed in this paper. **Figure 6.9** (a) and (b) display the optimized configuration of doped graphitic N and pyridinic N. The C-N bond length between graphitic N and surrounding carbon atoms is 1.41 Å, very close to the sp^2 C=C bond length (1.42 Å) in graphene. Furthermore, the C-N bond angle is 120.1°, almost identical to the sp^2 C=C bond angle (120.7°) in pure graphene, indicating that graphitic N doping has minimally altered the spatial configuration of the original graphene. The bond length between pyridinic N and lower chemical activity. **Figure 6.9** (c) illustrates the optimized configuration of C_3PO-doped graphene. The P atom exhibits sp^3 hybridization with a bond angle of 100.8°. The three C-P bonds are all 1.76 Å in length, forming an overall triangular pyramid structure. Due to the significant difference in radius between P and C atoms, the doped graphene undergoes noticeable deformation. The C-P bond length is 23.9 % longer than the sp^2 C=C double bond in pure graphene, causing the carbon network to protrude 1.28 Å in the Z direction. This implies a significant expansion of the interlayer spacing of carbon layers. This result is beneficial for preventing carbon layer stacking in 3D space, reducing graphene agglomeration, and offering possibilities for preparing 2D carbon materials. The optimized
configuration of the C_2PO_2 structure is shown in Fig. 6(d). The average bond length between P atoms and surrounding carbon atoms is 1.79 Å, with a bond angle of 98°. Unlike the C_3PO structure, the tensile stress of P atoms on graphene forms an angle with the Z direction, resulting in the graphene plane protruding only 0.4 Å along the Z-axis.

It has been proved that the Gibbs free-energy (ΔG_{H^*}) for the surface adsorption of H atoms is a crucial indicator of the acidic HER activity[49–50]. Therefore, we calculated the ΔG_{H^*} (Fig 7) for the possible active sites in 9 models. According to Sabatier's principle, the interaction force between the HER active site and the H atom should not be too weak or too strong.

Therefore, when the ΔG_{H^*} value of the catalyst is close to 0, the catalyst is considered to have superior catalytic activity. According to **Figure 6.10**, the ΔG_{H^*} of pure graphene is 1.37 eV (**Figure 6.10** (a)). In the N atom singly doped system, the ΔG_{H^*} of the C carbon atom adjacent to the pyridine N is 1.67 eV (**Figure 6.10** (c)), which is more positive than that of the ΔG_{H^*} of pure graphene, exhibiting inertness to HER. The neighboring C atom of graphitic N has a ΔG_{H^*} of 0.71 eV (**Figure 6.10** (b)), showing high catalytic activity for HER than pure graphene. This result proves that pyridine N and graphitic N have different modulation effects on the electronic structure of graphene. For the P single-doped system, the two

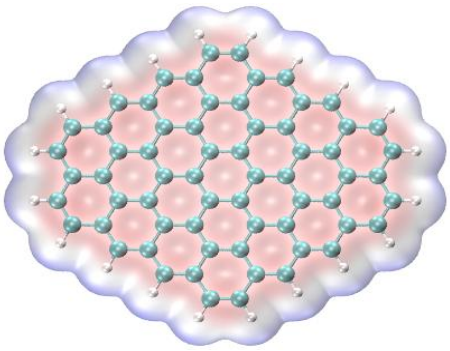

Figure 6.11 ESP of pure graphene**.**

neighboring C of C_3PO exhibit different ΔG_{H^*}. The ΔG_{H^*} of site 1 is 0.29 eV and that of site 2 is -0.21 eV.

Table 6.4 Mulliken charges and ESP of pure graphene.

ESP		Cluster	Mulliken charges
NG	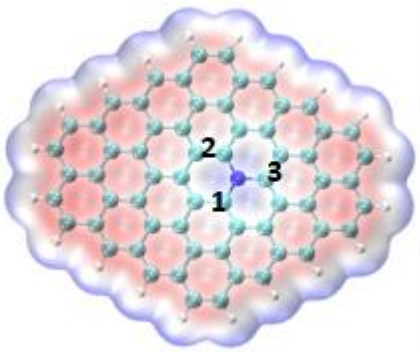	C1	0.362
		C2	0.367
		C3	0.392
		N	-0.8
PN	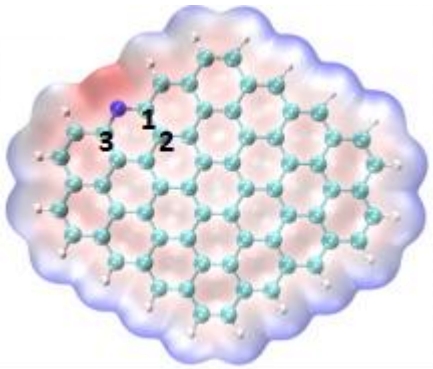	C1	0.129
		C2	-0.142
		C3	0.109
		N	-0.382
C_3PO-G	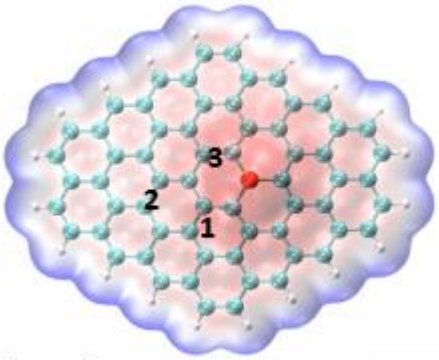	C1	-0.45
		C2	-0.391
		C3	-0.45
		P	1.183
		O	-0.535
C_2PO_2-G	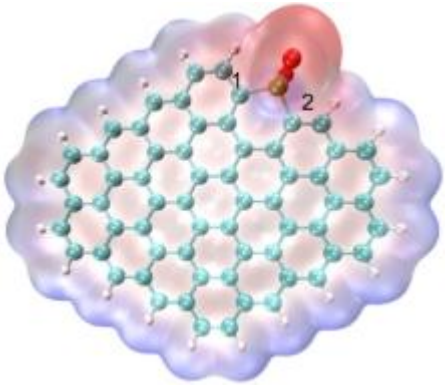	C1	-0.485
		C2	-0.494
		P	1.262
		O(H)	-0.528
		O(P)	-0.55

It can be seen that the electronic structure of site 2 is greatly adjusted, strong interaction with hydrogen atoms, to exhibit a good HER catalytic activity (**Figure 6.10** (d)). The electronic structure of graphene has a greater effect on the ΔG_{H^*} of sites 1 and 2. The difference of ΔG_{H^*} of 1 and 2 site implies that the charge transfer from P sites to site 1and 2 is different. In contrast, although the C_2PO_2 structure (**Figure 6.10**(e)) also promotes HER activity, the neighboring carbons have a more positive ΔG_{H^*}(0.79) compared to C_3PO. In addition, we have investigated the ΔG_{H^*} of the possible active sites when C_3PO is co-doped with graphitic N (neighboring, meta and para). When the graphitic N is in the meta position of the P atom, the ΔG_{H^*} of the 1-site is 0.37 eV (**Figure 6.10** (f)), which shows an enhancement of 0.58 eV compared with that of the ΔG_{H^*} before doping with N atoms. These results indicate that the addition of graphitic N in the neighboring position of the P atom has a synergetic effect on the HER of 2-site. When

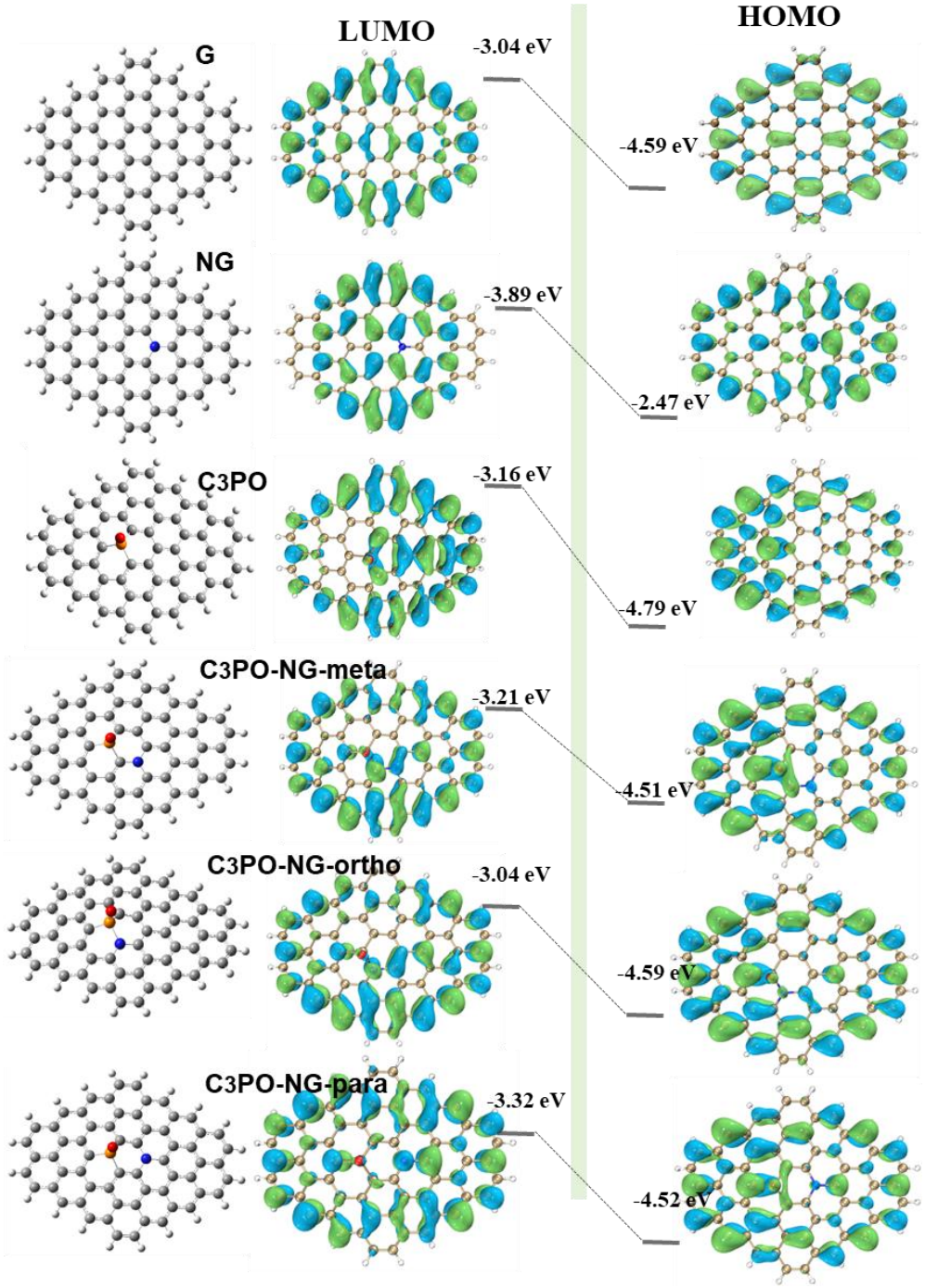

Figure 6.12 The HOMO and LUMO orbitals of the various models.

the graphitic N is located in the interstitial position of the P atom, the ΔG_{H^*} of the 1-site is 0.13 eV (**Figure 6.10** (g)), which is 0.16 eV lower than that before graphitic N doping, much closer to 0 than other active sites. This result indicates that when graphitic N is located in the interstitial site of the C_3PO structure, they have a good synergistic effect, resulting in an optimal HER catalytic activity of the intermediate C. For **Figure 6.10 (**h), the ΔG_{H^*} of the 1-site is 0.9 eV, which is 0.61 eV higher than that before doping, which implies that the para-doped graphitic N is able to weaken the interaction of the 1-site with H atoms. Above, we get an interesting conclusion that when graphitic N is present in the neighborhood of a C atom around C_3PO, the interaction of the C atom with H will be enhanced. In contrast, when graphitic N is present in its meta site, the interaction of C with the H atoms will be weakened. Furthermore, the synergistic doping effect of C_2PO_2 with pyridine N has also been considered. The carbon atom located between C_2PO_2 and the pyridinic N has a ΔG_{H^*} 0.79 eV (**Figure 6.10**(i)). The addition of pyridine N makes the interaction between the hydrogen atom and the surrounding carbon atoms weaker than in the C_2PO_2 doped system.

The analysis of electronic structure is crucial for understanding the mechanism of co-doping system The enhancement mechanism of N, P co-doped graphene was first analyzed using electrostatic potential (ESP) energy spectra. The atomic charges and electrostatic potential map of the optimized pristine graphene model are presented in **Figure 6.11**. It is observed that the atomic charges in graphene alternate between positive and negative values, with the outermost carbon atoms displaying a slight negative charge due to hydrogen passivation. In graphene, the p orbitals of each carbon atom overlap with the p orbitals of the three adjacent carbon atoms, forming a large π-bond conjugated structure. Therefore, the ESP distribution on the surface of pristine graphene is remarkably uniform, indicating that all delocalized electrons in the π system are inert. Due to the higher electronegativity of N (3.06) compared to carbon (2.5), the introduction of N creates an electron-withdrawing inductive effect, causing polarization of the C-N bond and shifting the electron density towards the N atom. According to the results in **Table 6.4**, the atomic charge of graphitic N is -0.8, while the atomic charges of the adjacent carbon atoms are 0.362, 0.367, and 0.392, respectively. In contrast, the atomic charge of pyridinic N is -0.382, with the atomic charges of its two neighboring carbon atoms being 0.129 and 0.109, respectively, confirming the presence of the electron-withdrawing inductive effect. Compared to pyridinic N, graphite N exhibits a greater difference in electronegativity with the surrounding carbon atoms, resulting in a stronger polarity of the C-N bond and increased chemical activity. In addition to the electron-withdrawing inductive effect, graphitic N also exhibits electron-donating conjugation effects. This is because the lone pair of electrons on the graphitic N is parallel to the p-orbitals of the surrounding carbon atoms and can be delocalized into the adjacent π-bonds, leading to an increase in the electron density of graphene. Notably, the electrostatic potential around the N is positive in the ESP (Electrostatic Potential) map of graphitic N, indicating a decrease in electron density around the N atom. Thus, in the graphene model doped with graphitic N, the electron-donating conjugation effect of the graphitic N prevails over the electron-withdrawing inductive effect. This results in an enhancement of electron density on the neighboring and para-position carbon atoms, which subsequently favors hydrogen adsorption. Pyridinic N, being sp^2 hybridized, has its lone pair of electrons perpendicular to the π-bonds and thus does not participate in conjugation but resides in the sp^2 hybridized orbital. Consequently, pyridinic N only exhibits an electron-withdrawing inductive effect, leading to a decrease in the electron density of the graphene plane. This is reflected in the ESP diagram of the pyridinic N,

where the electrostatic potential above the pyridinic N is negative, which hinders hydrogen adsorption on the adjacent carbon atoms. The electronegativity of the oxygen atom in the C_3PO structure (3.5) is significantly greater than that of the P atom (2.19), resulting in a high polarity of the P=O bond with an electron-withdrawing inductive effect. As observed in Fig S16 the atomic charge of the central P atom is 1.183, while the atomic charges of the surrounding carbon atoms are -0.45, -0.391, and -0.45, respectively. Combined with the ESP the influence of the oxygen atom causes the atomic charge of the P atom to become more positive. Additionally, the difference in electronegativity between P and C becomes more pronounced, which enhances the polarity of the P-C bonds. Consequently, the electron density shifts towards the neighboring carbon atoms. Combined with the calculations of ΔG_H, we find that the interaction strength between carbon atoms and H atoms does not depend on the magnitude of the charge of its central atom, but on the electron cloud density of the orbitals around the C atom. To summarize, the conjugation effect and the induced effect need to be considered together. When dopant atoms exhibit the overall effect of electron-donation, their neighboring and opposite sites are favorable for hydrogen adsorption, while their interstitial sites are relatively unfavorable for hydrogen adsorption. When the overall effect of dopant atoms is an electron-withdrawing effect, the neighboring and opposite sites are unfavorable for hydrogen adsorption, while the interstitial sites are relatively suitable for hydrogen adsorption. In the C_3PO structure, the electron-withdrawing effect of the O atom is dominant, and the interstitial carbon shows better HER activity. For the co-doped system, when graphitic N is located in the neighboring position, the electron cloud density of its neighboring P atoms increases, and the electron cloud density on the interstitial C atom (site 2) decreases compared to that before N atom doping, and thus and provides a fast electron channel for the HER. The opposite is true when the graphitic N is in the para position. In this case, the C atom is located in the interstitial position of graphitic N, and has a lower interaction with the hydrogen atom. The P atom is located in the para-position of graphitic N, and the charge of the atom will become more negative. So, the C-P polarity is weakened, and the electron density that was originally shifted towards the neighboring C position is weakened, which is not conducive to the adsorption of H atoms. It is worth noting that, because the graphitic N is an electron-donating group and P = O is an electron-withdrawing group, the electrons would transfer from graphitic N to P atom of P=O via neighboring C. The presence of electron push power from graphitic N and electron pull power from C_3PO leads to regional polarization, which accelerates the transfer of electrons and favors the adsorption towards H atoms. When the graphite is located in an intermediate site, its neighboring C atom electron cloud density increases, enhancing its interaction with H atoms.

Highest Occupied Molecular Orbital (HOMO) and Lowest Unoccupied Molecular Orbital (LUMO) together constitute the frontier orbitals of a molecule. The electrons in these orbitals play a crucial role in chemical reactions. The value of E(LUMO) minus E(HOMO) represents the HOMO-LUMO orbital energy gap, which is an important indicator of the stability, chemical reactivity, conductivity, and electrophilic/nucleophilic capabilities of reactive molecules. Therefore, we analyzed the HOMO and LUMO orbital structures of various doped graphene types. According to the **Figure 6.12**, the LUMO and HOMO values of pure graphene are -3.05 eV and -4.6 eV respectively, with a HOMO-LUMO energy gap of 1.545 eV. Heteroatom doping significantly altered the LUMO and HOMO values of pure graphene. Among the four models containing only one type of dopant, only graphitic N injected electrons into the HOMO orbital of pure graphene, increasing its energy value by 15 %. The E(HOMO)

values for pyridinic N, C_3PO, and C_2PO_2 are -4.76, -4.78 and -4.73, respectively, reducing the HOMO orbital energy by 3 %, 4 %, and 2 %. This result demonstrates that graphitic N has an electron-donating conjugation effect, enhancing the electron cloud density of graphene and making it more nucleophilic. The other three structures are electron-withdrawing groups, reducing the overall electron cloud density of graphene. The differences in E(LUMO)-E(HOMO) are recorded in the figure. The energy gaps for NG, PN, C_3PO, and C_2PO_2 structures are 1.416, 1.55, 1.635, and 1.71, respectively. Compared to pure graphene, these gaps decreased by 8 %, and increased by 0.3 %, 5 %, and 10 %, respectively. This observation indicates that graphitic N doping is beneficial for reducing the energy gap of graphene, resulting in faster electron transfer on the graphene surface and improved conductivity. For NG and C_3PO co-doped graphene, graphitic N can inject electrons into the HOMO orbital, while the P=O group can effectively lower the E(LUMO) of graphene. The synergistic effect of these two leads to a further reduction in graphene's energy gap, accelerating electron transfer on the graphene surface and facilitating adsorption reactions. According to the figure, we found that the energy gaps of ortho-, meta-, and para-position co-doped graphene are 1.31, 1.33, and 1.19, respectively, which are 18 %, 14 %, and 23 % smaller than that of pure graphene.

6.4 Conclusion

In summary, the chain-like amino acid structure intersected and liaised with the six-membered ring of phytic acid to produce a carbon network. An ultrathin nanocarbon layer was prepared by one-step pyrolysis, which ensured the full exposure of the active sites. The effect of phytic acid addition on the content of different N, P species in the product was investigated by adjusting the ratio of input materials. Combining experiments and calculations, the interaction strength between C atoms and H atoms is mainly affected by the electron density distribution on the surface of graphene. Specifically, the induced effect and conjugation effect of the dopant atoms should be both considered. The ortho and para sites of the electron-donating groups have milder ΔG_{H^*} compared to the meta site. In contrast, the meta sites of the electron-absorbing atoms have more appropriate ΔG_{H^*} than ortho site and para site. As a result, when the graphitic N co-doped at the meta site of C3PO, they have a synergistic effect and optimal hydrogen adsorption free energy (ΔGH^*=0.13). In addition, the graphitic N can inject the lone electron into the large π bond, so that the HOMO orbital energy of graphene is enhanced and the HOMO-LUMO spacing is reduced, which accelerates the charge transfer rate and facilitates the adsorption reaction. The best catalyst exhibited outstanding HER activity, with an extraordinarily low overpotential of 306 mV at 10 mA cm^{-2}.

Reference

[1] H. Li, M. Eddaoudi, M. O'Keeffe, O. M. Yaghi. Design and synthesis of an exceptionally stable and highly porous metal-organic framework. Nature, 1999, 402, 276–279.
[2] Dubouis N, Grimaud A. The hydrogen evolution reaction: from material to interfacial descriptors[J]. Chemical Science, 2019, 10(40): 9165-9181.
[3] A. E. Baumann, D. A. Burns, B. Liu, V. S. Thoi. Metal-organic framework functionalization and design strategies for advanced electrochemical energy storage devices. Commun Chem, 2019, 2, 86.
[4] Zeng M, Li Y. Recent advances in heterogeneous electrocatalysts for the hydrogen evolution reaction[J]. Journal of Materials Chemistry A, 2015, 3(29): 14942-14962.
[5] Zheng Y, Jiao Y, Jaroniec M, et al. Advancing the electrochemistry of the hydrogen-evolution reaction through combining experiment and theory[J]. Angewandte Chemie International Edition, 2015, 54(1): 52-65.
[6] Wang H, Fu W, Yang X, et al. Recent advancements in heterostructured interface engineering for hydrogen evolution reaction electrocatalysis[J]. Journal of materials chemistry A, 2020, 8(15): 6926-6956.
[7] Olivares-Ramírez J M, Campos-Cornelio M L, Godínez J U, et al. Studies on the hydrogen evolution reaction on different stainless steels[J]. International Journal of Hydrogen Energy, 2007, 32(15): 3170-3173.
[8] Bender J T, Petersen A S, Østergaard F C, et al. Understanding cation effects on the hydrogen evolution reaction[J]. ACS Energy Letters, 2022, 8(1): 657-665.
[9] Li Y, Wang H, Xie L, et al. MoS_2 nanoparticles grown on graphene: an advanced catalyst for the hydrogen evolution reaction[J]. Journal of the American Chemical Society, 2011, 133(19): 7296-7299.
[10] Wei J, Zhou M, Long A, et al. Heterostructured electrocatalysts for hydrogen evolution reaction under alkaline conditions[J]. Nano-micro letters, 2018, 10(4): 75.
[11] Cao X, Han Y, Gao C, et al. Highly catalytic active PtNiCu nanochains for hydrogen evolution reaction[J]. Nano Energy, 2014, 9: 301-308.
[12] Sheng W, Myint M N Z, Chen J G, et al. Correlating the hydrogen evolution reaction activity in alkaline electrolytes with the hydrogen binding energy on monometallic surfaces[J]. Energy & Environmental Science, 2013, 6(5): 1509-1512.
[13] Shi Y, Zhang B. Recent advances in transition metal phosphide nanomaterials: synthesis and applications in hydrogen evolution reaction[J]. Chemical Society Reviews, 2016, 45(6): 1529-1541.
[14] Ďurovič M, Hnát J, Bouzek K. Electrocatalysts for the hydrogen evolution reaction in alkaline and neutral media. A comparative review[J]. Journal of Power Sources, 2021, 493: 229708.
[15] Vesborg P C K, Seger B, Chorkendorff I B. Recent development in hydrogen evolution reaction catalysts and their practical implementation[J]. The journal of physical chemistry letters, 2015, 6(6): 951-957.
[16] Sun F, Tang Q, Jiang D. Theoretical advances in understanding and designing the active sites for hydrogen evolution reaction[J]. ACS Catalysis, 2022, 12(14): 8404-8433.
[17] Sun H, Yan Z, Liu F, et al. Self-supported transition-metal-based electrocatalysts for hydrogen and oxygen evolution[J]. Advanced materials, 2020, 32(3): 1806326.
[18] Kibsgaard J, Tsai C, Chan K, et al. Designing an improved transition metal phosphide catalyst for hydrogen evolution using experimental and theoretical trends[J]. Energy & Environmental Science,

2015, 8(10): 3022-3029.
[19] Saini R, Naaz F, Bashal A H, et al. Recent advances in nitrogen-doped graphene-based heterostructures and composites: mechanism and active sites for electrochemical ORR and HER[J]. Green Chemistry, 2024, 26(1): 57-102.
[20] Li S, Yu Z, Yang Y, et al. Nitrogen-doped truncated carbon nanotubes inserted into nitrogen-doped graphene nanosheets with a sandwich structure: a highly efficient metal-free catalyst for the HER[J]. Journal of Materials Chemistry A, 2017, 5(14): 6405-6410.
[21] Fung V, Hu G, Wu Z, et al. Descriptors for hydrogen evolution on single atom catalysts in nitrogen-doped graphene[J]. The Journal of Physical Chemistry C, 2020, 124(36): 19571-19578.
[22] Ye S, Luo F, Xu T, et al. Boosting the alkaline hydrogen evolution of Ru nanoclusters anchored on B/N–doped graphene by accelerating water dissociation[J]. Nano Energy, 2020, 68: 104301.
[23] Tian Y, Ye Y, Wang X, et al. Three-dimensional N-doped, plasma-etched graphene: Highly active metal-free catalyst for hydrogen evolution reaction[J]. Applied Catalysis A: General, 2017, 529: 127-133.
[24] Zhou S, Yang X, Pei W, et al. Heterostructures of MXenes and N-doped graphene as highly active bifunctional electrocatalysts[J]. Nanoscale, 2018, 10(23): 10876-10883.
[25] Thirumal V, Yuvakkumar R, Kumar P S, et al. Nitrogen and nitrogen-sulfur doped graphene nanosheets for efficient hydrogen productions for HER studies[J]. International Journal of Hydrogen Energy, 2022, 47(98): 41461-41467.
[26] Deng B, Wang D, Jiang Z, et al. Amine group induced high activity of highly torn amine functionalized nitrogen-doped graphene as the metal-free catalyst for hydrogen evolution reaction[J]. Carbon, 2018, 138: 169-178.
[27] Qu Y, Ke Y, Shao Y, et al. Effect of curvature on the hydrogen evolution reaction of graphene[J]. The Journal of Physical Chemistry C, 2018, 122(44): 25331-25338.
[28] Zhang J, Dai L. Nitrogen, phosphorus, and fluorine tri-doped graphene as a multifunctional catalyst for self-powered electrochemical water splitting[J]. Angewandte Chemie, 2016, 128(42): 13490-13494.
[29] Duan J, Chen S, Jaroniec M, et al. Heteroatom-doped graphene-based materials for energy-relevant electrocatalytic processes[J]. Acs Catalysis, 2015, 5(9): 5207-5234.
[30] Ito Y, Cong W, Fujita T, et al. High catalytic activity of nitrogen and sulfur co-doped nanoporous graphene in the hydrogen evolution reaction[J]. Angewandte Chemie International Edition, 2015, 54(7): 2131-2136.
[31] Zhou J, Qi F, Chen Y, et al. CVD-grown three-dimensional sulfur-doped graphene as a binder-free electrocatalytic electrode for highly effective and stable hydrogen evolution reaction[J]. Journal of Materials Science, 2018, 53(10): 7767-7777.
[32] Zhang X, Wang Y, Wang K, et al. Active sites engineering via tuning configuration between graphitic-N and thiophenic-S dopants in one-step synthesized graphene nanosheets for efficient water-cycled electrocatalysis[J]. Chemical Engineering Journal, 2021, 416: 129096.
[33] Li X, Duan X, Han C, et al. Chemical activation of nitrogen and sulfur co-doped graphene as defect-rich carbocatalyst for electrochemical water splitting[J]. Carbon, 2019, 148: 540-549.
[34] Zhao J, Liu Y, Quan X, et al. Nitrogen and sulfur co-doped graphene/carbon nanotube as metal-free electrocatalyst for oxygen evolution reaction: the enhanced performance by sulfur doping[J]. Electrochimica Acta, 2016, 204: 169-175.

[35] Lee S J, Theerthagiri J, Nithyadharseni P, et al. Heteroatom-doped graphene-based materials for sustainable energy applications: A review[J]. Renewable and Sustainable Energy Reviews, 2021, 143: 110849.

[36] Qu K, Zheng Y, Zhang X, et al. Promotion of electrocatalytic hydrogen evolution reaction on nitrogen-doped carbon nanosheets with secondary heteroatoms[J]. ACS nano, 2017, 11(7): 7293-7300.

[37] García-Dalí S, Quílez-Bermejo J, Castro-Gutiérrez J, et al. Green and easy synthesis of P-doped carbon-based hydrogen evolution reaction electrocatalysts[J]. Carbon, 2023, 212: 118154.

[38] Li Y, Ai C, Deng S, et al. Nitrogen doped vertical graphene as metal-free electrocatalyst for hydrogen evolution reaction[J]. Materials Research Bulletin, 2021, 134: 111094.

[39] Bi Z, Huo L, Kong Q, et al. Structural evolution of phosphorus species on graphene with a stabilized electrochemical interface[J]. ACS Applied Materials & Interfaces, 2019, 11(12): 11421-11430.

[40] Béguerie T, Weiss-Hortala E, Nzihou A. Calcium as an innovative and effective catalyst for the synthesis of graphene-like materials from cellulose[J]. Scientific Reports, 2022, 12(1): 21492.

[41] Long Z, Sun L, Zhu W, et al. P-Doped carbons derived from cellulose as highly efficient metal-free catalysts for aerobic oxidation of benzyl alcohol in water under an air atmosphere[J]. Chemical Communications, 2018, 54(65): 8991-8994.

[42] Wang W, Bao T, Wang H, et al. Se and P dual doped carbon for highly selective oxidation of benzyl alcohol[J]. Molecular Catalysis, 2023, 541: 113112.

[43] Rosas J M, Ruiz-Rosas R, Rodríguez-Mirasol J, et al. Kinetic study of the oxidation resistance of phosphorus-containing activated carbons[J]. Carbon, 2012, 50(4): 1523-1537.

[44] Jiao L, Wang C, Wu Y, et al. A phosphorus-doped carbon material derived from a sodium alginate/phosphoric acid hydrogel as an efficient catalyst for catalytic oxidation of furfural to maleic acid[J]. Catalysis Science & Technology, 2024, 14(17): 4997-5008.

[45] Pels J R, Kapteijn F L, Moulijn J A, et al. Evolution of nitrogen functionalities in carbonaceous materials during pyrolysis[J]. Carbon, 1995, 33(11): 1641-1653.

[46] Xiao B, Boudou J P, Thomas K M. Reactions of nitrogen and oxygen surface groups in nanoporous carbons under inert and reducing atmospheres[J]. Langmuir, 2005, 21(8): 3400-3409.

[47] Wang H, Zhang C, Liu Z, et al. Nitrogen-doped graphene nanosheets with excellent lithium storage properties[J]. Journal of Materials Chemistry, 2011, 21(14): 5430-5434.

Chapter 7

Various amino acids serve as precursors for synthesizing nitrogen and phosphorus carbon materials.

In Chapter 6, the synergistic doping effects of N and P atoms on carbon skeleton has been explored. To achieve the optimal hydrogen adsorption energy, the maximizing content of graphitic N and C_3PO structures is essential. To realize this, we systematically investigated the influence of precursor types on the N and P dopants in the final products. Among various functional groups, the imidazole ring demonstrates strong conjugation with the hexagonal framework of phytic acid, enabling direct incorporation into the carbon skeleton during graphitization process and thereby enhancing the content of graphitic N. Additionally, the basic nitrogen atom in the imidazole ring can be protonated by phosphate groups, facilitating the stabilization of C_3PO structures. Consequently, we selected histidine and linear amino acids as comparative precursors to evaluate the optimization effect of the imidazole ring on the catalytic performance of N,P co-doped systems.

7.1 Introduction

In recent years, the misuse of fossil fuels has led to severe environmental problems, increasing the urgency to find renewable energy sources. Among all the possible options, hydrogen stands out because of its considerable energy density and non-polluting combustion products. While various methods for producing hydrogen, only water splitting is truly carbon-free. However, the implementation of this method has been hindered by its enormous energy barrier, which has plagued scientists over several decades. The hydrogen evolution reaction (HER), an essential half-reaction for water splitting, is a critical factor in determining the water splitting efficiency. The best HER catalysts are currently Pt-based, but their high cost and scarcity limit their use. Therefore, developing affordable catalysts with high HER efficiency to replace Pt-based.

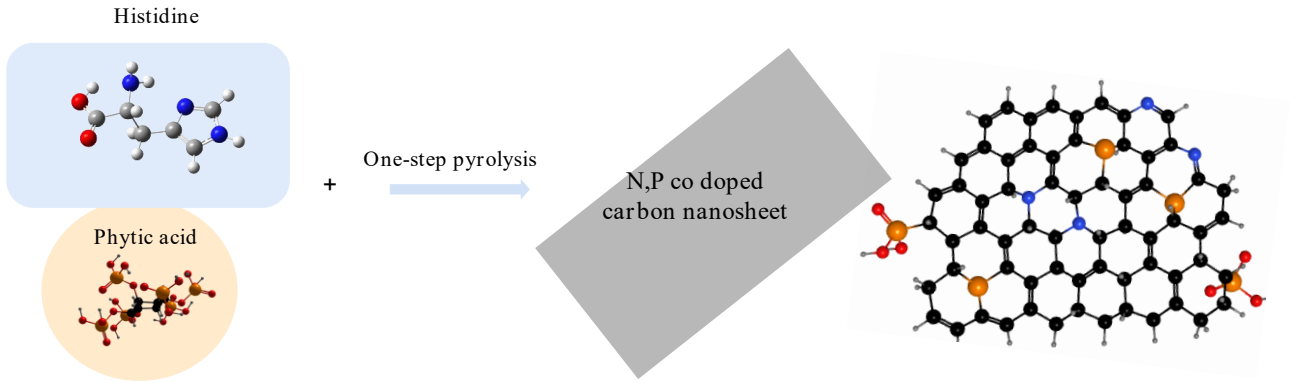

Scheme 7.1 The synthesis process of the various samples.

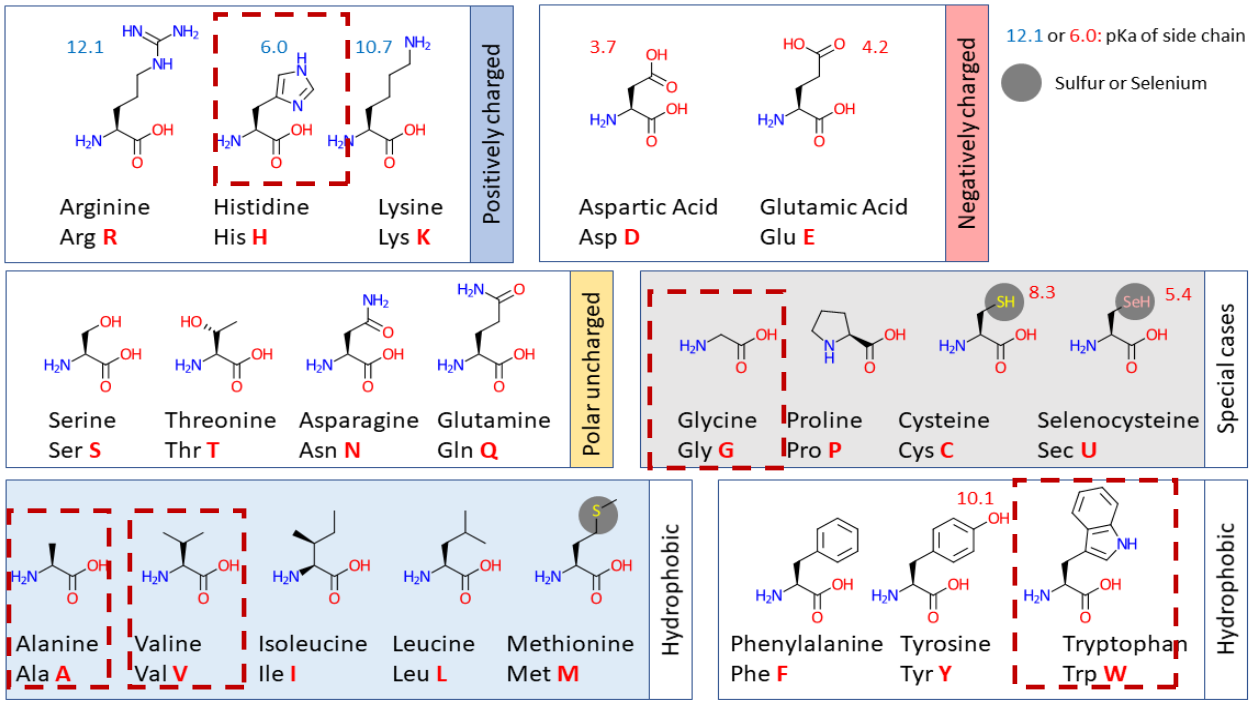

Figure 7.1 The nitrogen-containing precursor configuration employed in this study (within the red box).

At present, the leading HER catalysts are categorized into noble metal and transition metal-based catalysts. Noble metal catalysts are known for their minimal overpotential yet are limited by their rarity and high cost, rendering them impractical for an economy-driven approach. In contrast, transition metal based catalysts are economy-friendly, but their application for the HER is hindered by their low conductivity and tendency to aggregate at elevated temperatures, which compromises their suitability for HER tasks. In the realm of hydrogen evolution reaction (HER) catalysts, carbon-based materials have emerged as a focal point of research due to their distinctive advantages. Carbon-based materials are known for their adjustable pore structures, which amplify the exposure of catalytic active sites and expedite the transfer of reactant species. Additionally, their superior electrical conductivity facilitates rapid electron transfer, while their exceptional corrosion resistance ensures durability in both acidic and alkaline electrolytic environments over prolonged periods. However, a notable challenge with carbon materials is their suboptimal hydrogen adsorption free energy (ΔG_{H^*}), which can impede the efficient adsorption of hydrogen atoms at the active sites. Recent advancements suggest that doping carbon materials with heteroatoms can significantly alter the electron cloud density around carbon atoms, thereby potentially optimizing the ΔG_{H^*} towards more favorable conditions. Pioneering work by Qu et al. has shown that co-doping carbon materials with heteroatoms not only multiplies the active sites on their surface but also promotes a "cooperative coupling" effect. This synergistic interaction markedly boosts the electrochemical activity of the carbon-based catalysts. Similarly, Sergio et al. utilized P-rich biomass precursor systems to develop P-doped carbon-based catalysts for the HER. Their research proposes that the P-C bonds, formed at high carbonization temperatures, could serve as the primary active species facilitating the HER.

Among all of the N precursors, amino acids are environmentally friendly materials rich in diverse functional groups and side-chain structures, making them ideal candidates for the controlled synthesis

of N-doped carbon materials. The wide variety of amino acids, whose side chains may contain hydroxyl, aromatic, or imidazole groups, significantly influences the hydrophilicity and microstructure of the resulting carbon materials. Moreover, amino acids are cost-effective raw materials suitable for large-scale production. In previously study, the synergistic doping effects of N and P atoms on carbon skeleton has been explored. To achieve the optimal hydrogen adsorption energy, the maximizing content of graphitic N and C_3PO structures is essential.

Herein, we systematically investigated the influence of precursor types on the N and P dopants in the final products. Among various functional groups, the imidazole ring demonstrates strong conjugation with the hexagonal framework of phytic acid, enabling direct incorporation into the carbon skeleton during graphitization process and thereby enhancing the content of graphitic N. Additionally, the basic nitrogen atom in the imidazole ring can be protonated by phosphate groups, facilitating the stabilization of C_3PO structures. Consequently, we selected histidine and linear amino acids as comparative precursors to evaluate the optimization effect of the imidazole ring on the catalytic performance of N,P co-doped systems (**Scheme 7.1**). Additionally, we compared the precursors of histidine and tryptophan to confirm the impact of the benzene ring and imidazole ring on product's performance and structure. All amino acids selected are recorded in **Figure 7.1**.

7.2 Experimental

7.2.1 Materials

Amino acids, and 50 % phytic acid were purchased from Wako Pure Chemical Industries Ltd. (Osaka, Japan). Pt/C catalyst (20 wt.%), isopropanol and Nafion (5 wt.%) were purchased from Sigma-Aldrich (Saint Louis, USA). N_2 gas (purity 99.99 %) was purchased from IWATANI FINE GAS Co., Ltd. All reagents were used as received without purification.

7.2.2 Synthesis of CNP

Typically, Amino acids and 50% phytic acid were dissolved in 1 mL of deionized water. The mixture was then dried at 90 °C for 2 h to form the C/N/P solid precursor. The as-made precursor was placed in a tube furnace and heated to 900 °C with a ramp of 5 °C min^{-1} and kept for 3 h under a N2 flow (60 mL min^{-1}). The product is denoted as "Amino acid-P".

7.2.3 Characterizations

The morphology was conducted by transmission electron microscopy (TEM, Hitachi H800). The mass ratio of carbon and P was investigated using energy-dispersive X-ray spectroscopy (EDX). The N content was measured using elemental analyzers (CHN, Perkin Elmer 2400IICHNS/O). Powder X-ray diffraction (XRD, RINT2200 with Cu Kα radiation) was used to determine the structure of the carbon layers. The element doping and valence states were evaluated using XPS (JEOL JPS-9000MX) with Mg Kα as the energy source. Raman spectra of the samples were recorded using a confocal Raman microscope (LabRAM HR-800, Horiba, Ltd., Kyoto, Japan).

7.2.4 Electrochemical measurements

To evaluate the hydrogen evolution reaction (HER) activity of the samples, we employed an ALS 2325 bi-potentiostat equipped with a standard three-electrode system. Hg/Hg_2Cl_2 served as the reference electrode for the 0.5 M H_2SO_4 electrolyte, while a graphite rod functioned as the counter electrode. To prepare the working electrode, the following procedure was followed: 8 mg of catalyst powder was dispersed in a solution containing 1 ml of isopropanol, 5 wt% Nafion, and deionized water ($V_{isopropanol}$: V_{Nafion}: $V_{Deionized\ water}$ = 1:1:8). The mixture was ultrasonicated to obtain homogeneous catalyst ink. Subsequently, a suspension (4 μg) of the catalyst ink was evenly coated onto a carbon cloth (with an area of 0.1256 cm^2) of a rotating ring-disk electrode, forming a thin and uniform carbon layer. The working electrode was thoroughly dried under ambient conditions for 30 min to complete its preparation.

To assess the HER activity of the samples, linear sweep voltammetry (LSV) was conducted at a sweep rate of 5 mV s^{-1} and a rotation speed of 1600 rpm under a N_2 flow at 80 mL/min.

Table 7.2 The crystalline parameters of various samples (mass ratio).

Sample	FWMN	2 theta
Gly-P	12.5	24.9
Ala-P	12.3	24.9
His-P	9.7	24.3
Try-P	9.1	24.4

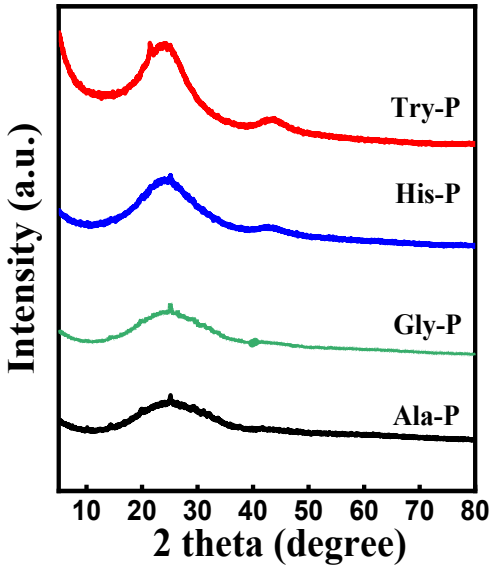

Figure 7.2 The XRD patterns of the various samples.

7.3 Results and discussion

7.3.1 The analyzing of crystalline phases for each sample by using XRD measurements

The XRD patterns of the N, P co-doped carbon materials synthesized at different temperatures are shown in Fig. 1 All samples exhibit an XRD pattern with a broad (002) diffraction peak centered at around 2θ = 23◦ (Amorphous carbon peak) and a (101) diffraction broad peak appears centered at around 2θ = 43◦, which relates to the formation of graphitic domains in the carbon structure. The enhancement of the signals at two peaks is attributed to the increased graphitization of the carbon material, which leads to a more orderly arrangement of carbon atoms. To quantify the degree of graphitization and the interlayer spacing of different samples, the half-width and peak positions of the samples were calculated. Sample Try-P exhibits the smallest FWHM, indicating that the benzene ring structure could effectively enhance graphitization degree when tryptophan serves as the precursor. Furthermore, histidine demonstrates superior graphitization compared to chain-type amino acids, suggesting that the imidazole ring also contributes to improved the graphitization degree of carbon skeleton. Moreover, we observed that Try-P and His-P samples exhibited larger lattice spacings compared to linear amino acids, suggesting that these two samples may possess a greater proportion of C_3PO structures.

7.3.2 The analysis of the amount for each sample by using CHN measurements

Table 7.3 The elements content of various samples (mass ratio).

Sample	C	P	P/C
Gly-P	87.98	2.73	3.10%
Ala-P	86.45	2.78	3.22%
Ser-P	87.03	2.54	2.92%
Val-P	86.14	2.23	2.59%
His-P	83.03	4.57	5.50%
Try-P	89.07	3.03	3.4%

To investigate the phosphorus fixation of different nitrogen-containing precursors, we tested the phosphorus content of various samples. **Table 7.3** lists the changes in P content in the products. It can be observed that when the precursor is histidine, the P content of the sample is significantly higher than that of other samples. This aligns with our hypothesis that the imidazole ring of histidine possesses excellent nitrogen-fixing capacity.

7.3.2 The analysis of the morphology of different samples by using SEM measurements

Figure 6.3 displays the morphology of the products. According to **Figure 7.3**, the homogeneous carbon nanosheets were successfully synthesized. The SEM images reveal that the glycine-derived product exhibits a well-defined porous architecture with clearly observable channels, attributable to the gaseous release (NH_3, CO_2) during pyrolysis and/or self-templating effects. In contrast, materials synthesized from other amino acids display relatively smooth surfaces, suggesting denser morphological features with limited porosity development. The TEM image reveals that Glycine/Alanine/Serine-derived samples consist of turbostratically stacked carbon layers, while the Histidine-derived sample exhibits

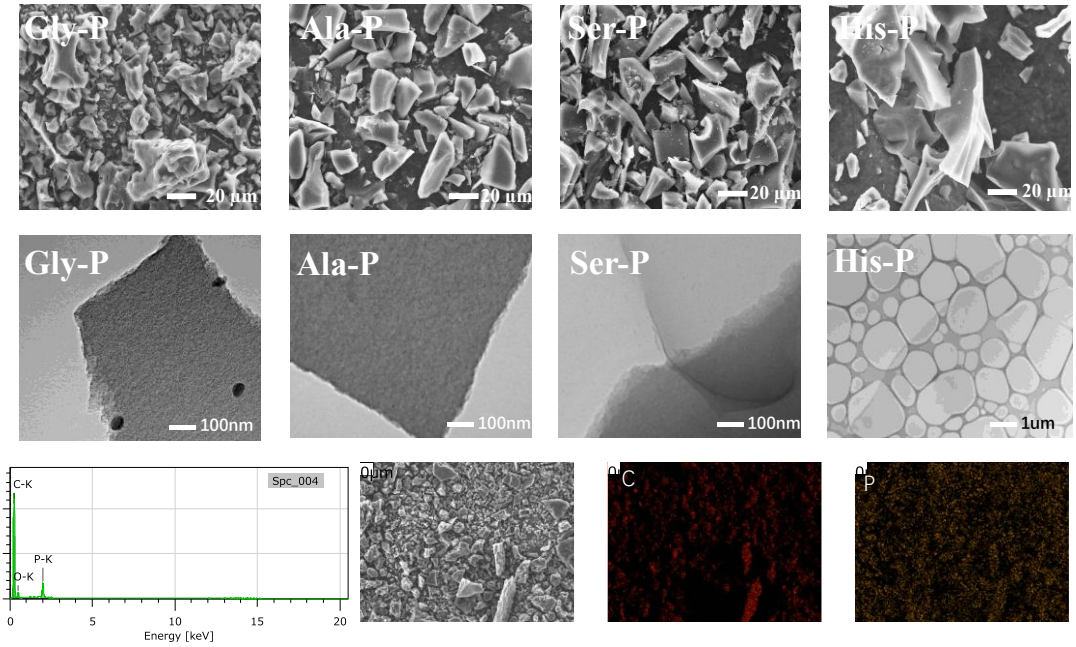

Figure 7.3 TEM, SEM and EDX images of the various samples.

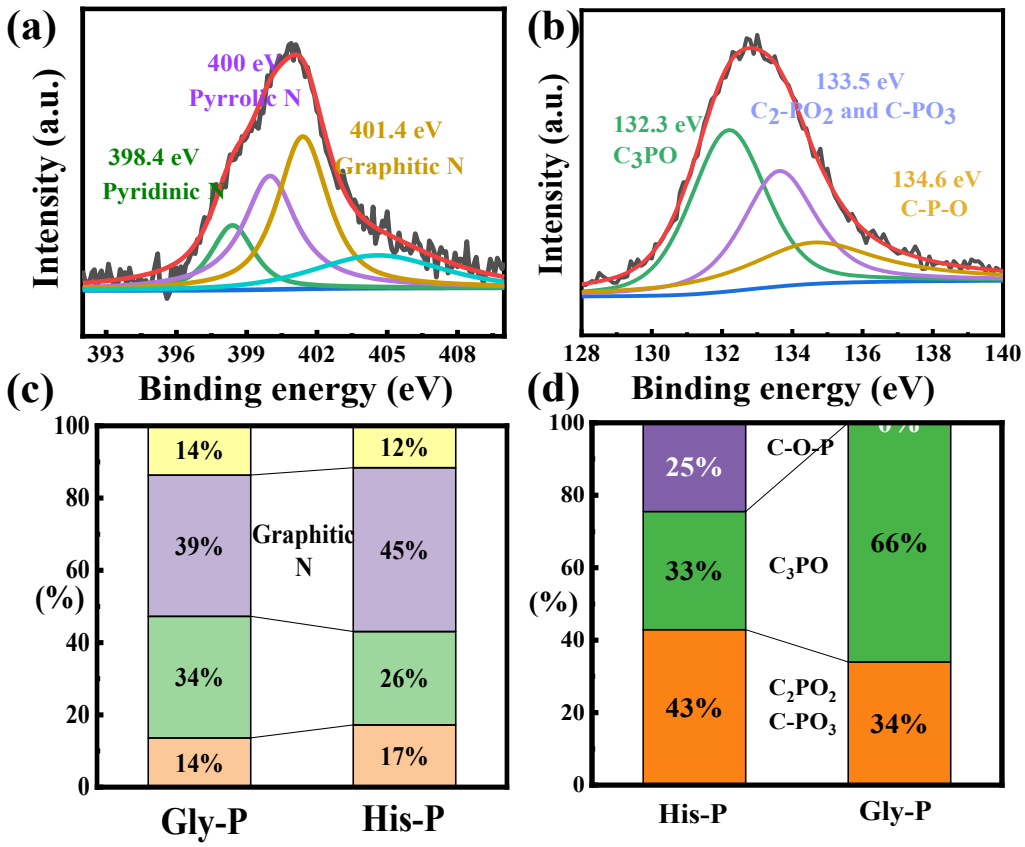

Figure 7.4 (a) The N 1s spectrum of His-P. (b) the P 2p spectrum of His-P. (c) The graphitic N content of His-P and Gly-P. (d) The P dopants of His-P and Gly-P.

an ultrathin nanosheet morphology, resulting from the chelating properties of histidine's imidazole group, which restricts vertical growth during carbonization. The divergent morphologies highlight precursor-dependent structural control, with glycine favoring porous networks and histidine enabling

2D nanostructures.

7.3.3 The identification of chemical composition for each samples using XPS measurements

Figure 7.4 shows the N 1s spectrum can be decomposed into three types of N atoms, graphitic N (401.4 eV), pyrrolic N (400. 1 eV), and pyridinic N (398.4 eV). This result confirmed thac wer0Zt almost all N species were incorporated into the carbon skeletons. The P 2p spectrum of His-P, which could be separated into two subpeaks (132.3 eV for C_3PO and 133.5 eV for C-PO_3 or C_2PO_2). It is worth noting that the peak at 132.5 eV for C_3PO reveals that P atoms were successfully doped into the carbon skeleton and replaced some carbon atoms. The peak at 133.5 eV for C-PO_3 or C_2PO_2 represents the bonding of P atoms with the edge carbon. To investigate the influence of amino acid precursors with different structures on the nitrogen and phosphorus species in the resulting products, we compared the composition of N and P species in Gly-P and His-P. As shown in the figure, compared to Gly-P, the pyridinic nitrogen content decreased in the His-P product, while pyrrolic nitrogen increased and graphitic nitrogen declined. This phenomenon may be related to the imidazole structure present in histidine. species, the His-P product exhibited a higher proportion of C_3PO structures than Gly-P. The slightly higher pyridinic nitrogen content in Gly-P and the relatively fewer C_3PO structures may stem from the gases released during glycine decomposition, which activate the carbon material—enhancing pore structure while disrupting the integrity of the graphitic layers.

7.3.4 The HER activity and ESCA of the catalysts

The activity of the hydrogen evolution reaction (HER) was measured using a typical three-electrode system consisting of a 0.5 M H_2SO_4 solution. The results are summarized in **Figure 7.5**. According to the findings, for amino acids with chain-like structures and smaller steric hindrance, HER performance deteriorates as the chain length increases, while Gly-P exhibits the best performance. Notably, among amino acids with greater steric hindrance, there is a significant difference between Try-P and His-P. Comparing the structures of Try-P and His-P, the imidazole ring of histidine exhibits strong alkalinity, and its nitrogen atom is more readily protonated, forming robust ionic bonds. From this perspective, histidine can effectively immobilize P species, which has been confirmed by XPS results. In contrast, the lone pair of electrons on the nitrogen atom of tryptophan's indole ring participates in extensive π-conjugation, resulting in very weak alkalinity and making protonation by phytic acid difficult. Consequently, electrostatic interactions during the pre-assembly process are significantly weaker than those of histidine. Additionally, we pyrolyzed histidine at different temperatures, and the performance of the catalyst decreased. This may be attributed to the leaching of nitrogen and phosphorus species at high temperatures. Meanwhile, we compared the ESCA spectra of Gly-P and His-P and ultimately found that Gly-P exhibits a larger active surface area. However, when evaluating their electrochemical activity, we observed that the intrinsic activity of His-P is significantly higher than that of Gly-P. This enhancement likely originates from a greater abundance of C_3PO structures and a higher degree of graphitization. Furthermore, the increased content of pyrrolic nitrogen may also contribute to this effect.

7.4 Conclusion

A one-step pyrolysis method was employed to investigate the reactions between different amino acids

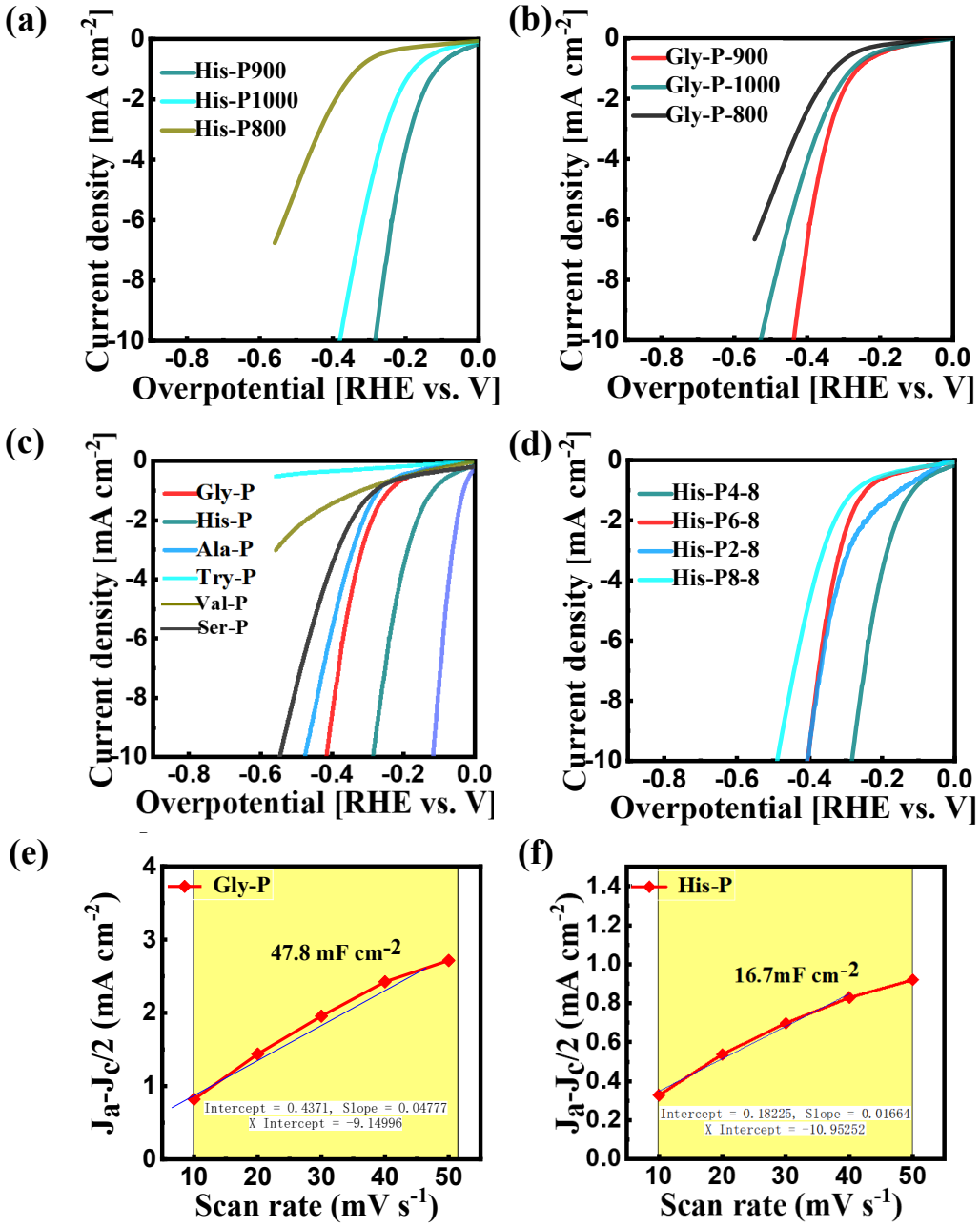

Figure 7.5 (a,b) The LSV curves of the Gly-P and His-P samples heating under different temperatures. (c) The LSV curves of the samples with different precursors. (d) The LSV curves of His-P with different precursors mass ratio. (e) The ESCA of sample Gly-P. (g) The ESCA of sample His-P.

and phytic acid. Among them, histidine and phytic acid exhibited strong coordination, resulting in products with high chemical activity. This strong coordination originates from electrostatic attraction during precursor pre-assembly, where phosphate groups ($-PO_4H_2$) protonate the nitrogen atom on histidine's imidazole ring (the N atom is preferentially protonated over the amino group), forming a positively charged moiety ($-N^+H-$) and reinforcing hydrogen bond networks. Specifically, dense hydrogen bond networks form between histidine's carboxyl group, amino group, and phytic acid's phosphate groups and hydroxyl groups. Additionally, π-π conjugation occurs between the imidazole

ring and the inositol structure.

Reference

[1] H. Li, M. Eddaoudi, M. O'Keeffe, O. M. Yaghi. Design and synthesis of an exceptionally stable and highly porous metal-organic framework. Nature, 1999, 402, 276–279.
[2] Dubouis N, Grimaud A. The hydrogen evolution reaction: from material to interfacial descriptors[J]. Chemical Science, 2019, 10(40): 9165-9181.
[3] A. E. Baumann, D. A. Burns, B. Liu, V. S. Thoi. Metal-organic framework functionalization and design strategies for advanced electrochemical energy storage devices. Commun Chem, 2019, 2, 86.
[4] Zeng M, Li Y. Recent advances in heterogeneous electrocatalysts for the hydrogen evolution reaction[J]. Journal of Materials Chemistry A, 2015, 3(29): 14942-14962.
[5] Zheng Y, Jiao Y, Jaroniec M, et al. Advancing the electrochemistry of the hydrogen-evolution reaction through combining experiment and theory[J]. Angewandte Chemie International Edition, 2015, 54(1): 52-65.
[6] Wang H, Fu W, Yang X, et al. Recent advancements in heterostructured interface engineering for hydrogen evolution reaction electrocatalysis[J]. Journal of materials chemistry A, 2020, 8(15): 6926-6956.
[7] Olivares-Ramírez J M, Campos-Cornelio M L, Godínez J U, et al. Studies on the hydrogen evolution reaction on different stainless steels[J]. International Journal of Hydrogen Energy, 2007, 32(15): 3170-3173.
[8] Bender J T, Petersen A S, Østergaard F C, et al. Understanding cation effects on the hydrogen evolution reaction[J]. ACS Energy Letters, 2022, 8(1): 657-665.
[9] Li Y, Wang H, Xie L, et al. MoS2 nanoparticles grown on graphene: an advanced catalyst for the hydrogen evolution reaction[J]. Journal of the American Chemical Society, 2011, 133(19): 7296-7299.
[10] Wei J, Zhou M, Long A, et al. Heterostructured electrocatalysts for hydrogen evolution reaction under alkaline conditions[J]. Nano-micro letters, 2018, 10(4): 75.
[11] Cao X, Han Y, Gao C, et al. Highly catalytic active PtNiCu nanochains for hydrogen evolution reaction[J]. Nano Energy, 2014, 9: 301-308.
[12] Sheng W, Myint M N Z, Chen J G, et al. Correlating the hydrogen evolution reaction activity in alkaline electrolytes with the hydrogen binding energy on monometallic surfaces[J]. Energy & Environmental Science, 2013, 6(5): 1509-1512.
[13] R. Ma, G. Lin, Y. Zhou, Q. Liu, T. Zhang, G. Shan, M. Yang, J. Wang. A review of oxygen reduction mechanisms for metal-free carbon-based electrocatalysts. npj Comput Mater, 2019, 5, 78.
[14] J. Zhang, L. Dai. Heteroatom-Doped Graphitic Carbon Catalysts for Efficient Electrocatalysis of Oxygen Reduction Reaction. ACS Catal., 2015, 5, 7244–7253.
[15] D. S. Su, G. Centi. A perspective on carbon materials for future energy application. Journal of Energy Chemistry, 2013, 22, 151–173.
[16] A. Serov, M. H. Robson, M. Smolnik, P. Atanassov. Templated bi-metallic non-PGM catalysts for oxygen reduction. Electrochimica Acta, 2012, 80, 213–218.
[17] J. Shui, M. Wang, F. Du, L. Dai. N-doped carbon nanomaterials are durable catalysts for oxygen reduction reaction in acidic fuel cells. Sci. Adv., 2015, 1, e1400129.
[18] D.-S. Yang, D. Bhattacharjya, S. Inamdar, J. Park, J.-S. Yu. Phosphorus-Doped Ordered Mesoporous Carbons with Different Lengths as Efficient Metal-Free Electrocatalysts for Oxygen Reduction Reaction in Alkaline Media. J. Am. Chem. Soc., 2012, 134, 16127–16130.

[19] J. Zhang, L. Qu, G. Shi, J. Liu, J. Chen, L. Dai. N,P-Codoped Carbon Networks as Efficient Metal-free Bifunctional Catalysts for Oxygen Reduction and Hydrogen Evolution Reactions. Angew. Chem. Int. Ed., 2016, 55, 2230–2234.
[20] K. Gong, F. Du, Z. Xia, M. Durstock, L. Dai. Nitrogen-Doped Carbon Nanotube Arrays with High Electrocatalytic Activity for Oxygen Reduction. Science, 2009, 323, 760–764.
[21] H. Zhong, J. Wang, Y. Zhang, W. Xu, W. Xing, D. Xu, Y. Zhang, X. Zhang. ZIF-8 Derived Graphene-Based Nitrogen-Doped Porous Carbon Sheets as Highly Efficient and Durable Oxygen Reduction Electrocatalysts. Angew. Chem. Int. Ed., 2014, 53, 14235–14239.
[22] L. Dai, D. W. Chang, J.-B. Baek, W. Lu. Carbon Nanomaterials for Advanced Energy Conversion and Storage. Small, 2012, 8, 1130–1166.
[23] H. Yu, L. Shang, T. Bian, R. Shi, G. I. N. Waterhouse, Y. Zhao, C. Zhou, L.-Z. Wu, C.-H. Tung, T. Zhang. Nitrogen-Doped Porous Carbon Nanosheets Templated from g-C3N4 as Metal-Free Electrocatalysts for Efficient Oxygen Reduction Reaction. Adv. Mater., 2016, 28, 5080–5086.
[24] H. B. Yang, J. Miao, S.-F. Hung, J. Chen, H. B. Tao, X. Wang, L. Zhang, R. Chen, J. Gao, H. M. Chen, L. Dai, B. Liu. Identification of catalytic sites for oxygen reduction and oxygen evolution in N-doped graphene materials: Development of highly efficient metal-free bifunctional electrocatalyst. Sci. Adv., 2016, 2, e1501122.
[25] G. Tao, L. Zhang, L. Chen, X. Cui, Z. Hua, M. Wang, J. Wang, Y. Chen, J. Shi. N-doped hierarchically macro/mesoporous carbon with excellent electrocatalytic activity and durability for oxygen reduction reaction. Carbon, 2015, 86, 108–117.
[26] Z. Lu, J. Wang, S. Huang, Y. Hou, Y. Li, Y. Zhao, S. Mu, J. Zhang, Y. Zhao. N,B-codoped defect-rich graphitic carbon nanocages as high performance multifunctional electrocatalysts. Nano Energy, 2017, 42, 334–340.
[27] J. Zhang, Y. Sun, J. Zhu, Z. Kou, P. Hu, L. Liu, S. Li, S. Mu, Y. Huang. Defect and pyridinic nitrogen engineering of carbon-based metal-free nanomaterial toward oxygen reduction. Nano Energy, 2018, 52, 307–314.
[28] O. L. Li, S. Chiba, Y. Wada, G. Panomsuwan, T. Ishizaki. Synthesis of graphitic-N and amino-N in nitrogen-doped carbon via a solution plasma process and exploration of their synergic effect for advanced oxygen reduction reaction. J. Mater. Chem. A, 2017, 5, 2073–2082.
[29] S. N. Faisal, E. Haque, N. Noorbehesht, W. Zhang, A. T. Harris, T. L. Church, A. I. Minett. Pyridinic and graphitic nitrogen-rich graphene for high-performance supercapacitors and metal-free bifunctional electrocatalysts for ORR and OER. RSC Adv., 2017, 7, 17950–17958.
[30] Sutarsis, J. Patra, C.-Y. Su, J. Li, D. Bresser, S. Passerini, J.-K. Chang. Manipulation of Nitrogen-Heteroatom Configuration for Enhanced Charge-Storage Performance and Reliability of Nanoporous Carbon Electrodes. ACS Appl. Mater. Interfaces, 2020, 12, 32797–32805.
[31] H. Jiang, J. Gu, X. Zheng, M. Liu, X. Qiu, L. Wang, W. Li, Z. Chen, X. Ji, J. Li. Defect-rich and ultrathin N doped carbon nanosheets as advanced trifunctional metal-free electrocatalysts for the ORR, OER and HER. Energy Environ. Sci., 2019, 12, 322–333.
[32] Y. Wang, Y. Pan, L. Zhu, N. Guo, R. Wang, Z. Zhang, S. Qiu. Structure regulation of amino acids derived nitrogen doped porous carbon nanosheet through facile solid state assembly method. Microporous and Mesoporous Materials, 2019, 277, 36–44.
[33] Z. Li, H. Chen, W. Liu. Full-Spectrum Photocatalytic Activity of ZnO/CuO/ZnFe2O4

Nanocomposite as a PhotoFenton-Like Catalyst. Catalysts, 2018, 8, 557.
[34] N. Joshi, L. F. da Silva, F. M. Shimizu, V. R. Mastelaro, J.-C. M'Peko, L. Lin, O. N. Oliveira. UV-assisted chemiresistors made with gold-modified ZnO nanorods to detect ozone gas at room temperature. Microchim Acta, 2019, 186, 418.
[35] C. E. Nanayakkara, P. M. Jayaweera, G. Rubasinghege, J. Baltrusaitis, V. H. Grassian. Surface Photochemistry of Adsorbed Nitrate: The Role of Adsorbed Water in the Formation of Reduced Nitrogen Species on α-Fe2O3 Particle Surfaces. J. Phys. Chem. A, 2014, 118, 158–166.
[36] K. Awsiuk, A. Psarouli, P. Petrou, A. Budkowski, S. Kakabakos, A. Bernasik, J. Rysz, I. Raptis. Spectroscopic and microscopic examination of protein adsorption and blocking of non-specific binding to silicon surfaces modified with APTES and GOPS. Procedia Engineering, 2011, 25, 334–337.
[37] T. Pillar-Little, D. Y. Kim. Differentiating the impact of nitrogen chemical states on optical properties of nitrogen-doped graphene quantum dots. RSC Adv., 2017, 7, 48263–48267.
[38] Y. Tang, J. Chen, Z. Mao, C. Roth, D. Wang. Highly N-doped carbon with low graphitic-N content as anode material for enhanced initial Coulombic efficiency of lithium-ion batteries. Carbon Energy, 2022, cey2.257.
[39] R. J. J. Jansen, H. van Bekkum. XPS of nitrogen-containing functional groups on activated carbon. Carbon, 1995, 33, 1021–1027.
[40] H. Viltres, O. F. Odio, Mark. C. Biesinger, G. Montiel, R. Borja, E. Reguera. Preparation of Amine- and Disulfide-Containing PAMAM-Based Dendrons for the Functionalization of Hydroxylated Surfaces: XPS as Structural Sensor. ChemistrySelect, 2020, 5, 4875–4884.
[41] H. Begum, M. S. Ahmed, Y.-B. Kim. Nitrogen-rich graphitic-carbon@graphene as a metal-free electrocatalyst for oxygen reduction reaction. Sci Rep, 2020, 10, 12431.
[42] J. Quílez-Bermejo, M. Melle-Franco, E. San-Fabián, E. Morallón, D. Cazorla-Amorós. Towards understanding the active sites for the ORR in N-doped carbon materials through fine-tuning of nitrogen functionalities: an experimental and computational approach. J. Mater. Chem. A, 2019, 7, 24239–24250.
[43] X. Ning, Y. Li, J. Ming, Q. Wang, H. Wang, Y. Cao, F. Peng, Y. Yang, H. Yu. Electronic synergism of pyridinic- and graphitic-nitrogen on N-doped carbons for the oxygen reduction reaction. Chem. Sci., 2019, 10, 1589–1596.
[44] L. Lai, J. R. Potts, D. Zhan, L. Wang, C. K. Poh, C. Tang, H. Gong, Z. Shen, J. Lin, R. S. Ruoff. Exploration of the active center structure of nitrogen-doped graphene-based catalysts for oxygen reduction reaction. Energy Environ. Sci., 2012, 5, 7936–7942.
[45] H. Kim, K. Lee, S. I. Woo, Y. Jung. On the mechanism of enhanced oxygen reduction reaction in nitrogen-doped graphene nanoribbons. Phys. Chem. Chem. Phys., 2011, 13, 17505.

General Conclusions

In this paper, I have investigated the current status of carbon-based catalysts in the field of HER, the mechanisms for designing HER catalysts, and the evaluation methods for catalytic performance (Chapters 1 and 2). I have also developed several synthesis methods for carbon-based electrocatalysts with specific morphologies (Chapters 3–7). In Chapter 1, the research background, current state of research, and several fundamental theories involved in the design of HER catalysts are explained. In Chapter 2, the testing system and key descriptors for HER activity are described. In Chapter 3, I explored the feasibility of using LDH structures as catalyst precursors. In Chapter 4, the phytic acid was used as a chelating agent that restricts the growth of CoP particles on the carbon substrate, controlling their size to 23 nm. In Chapter 5, by utilizing the spatial confinement effect of ion-exchange resins, cobalt species were anchored onto the organic carbon skeleton. Subsequently, by leveraging the molecular bridging effect of phytic acid, the P source was immobilized on the surface and within the pores of carbon skeleton. The resulting Co_2P particles were confined to a size of 13 nm. In addition, sulfur doping was successfully achieved using SO_2 generated from the decomposition of sulfonic acid groups, optimizing the hydrogen adsorption free energy of the active sites. In Chapter 6, ultrathin N,P co-doped nanosheets were synthesized via a simple one-step pyrolysis method. The synergistic doping mechanism of the C_3PO structure and graphitic nitrogen was analyzed by combining DFT calculations with experimental data. In Chapter 7, the influence of different amino acid precursors on the N and P species in products was investigated, as well as the phosphorus-fixing effect of imidazole groups.

Summary of Chapter 3

I present a flower-like carbon-coated transition metal alloy catalyst prepared through a combined CVD and hydrothermal approach. Layered double hydroxides (LDHs) was used as precursors, which could offer high specific surface area, exchangeable interlayer anions, and tunable active sites. Carbon coating was applied to LDHs materials using the CVD method, while simultaneously reducing them into alloy, significantly enhancing the conductivity of the catalyst system. Additionally, MoO_4^{2-} ions were used to chemically etch the LDH precursors, increasing the active surface area of the catalyst.

Summary of Chapter 4

In Chapter 4, a straightforward and eco-friendly one-step synthesis method was developed to prepare carbon-based materials loaded with nanosized transition metal phosphide particles. In this study, by leveraging the chelating effect of phytic acid on transition metal elements, the agglomeration of CoP particles in the product was effectively restricted. By adjusting the precursor ratio, it was found that when the Co/P ratio in the precursor was 0.89, a balance was achieved between cobalt loading and the chelating effect of phytic acid. At this point, the average size of CoP particles in the product was only 23 nm.

Summary of Chapter 5

In Chapter 5, I utilized the spatial confinement effect of ion-exchange resins on transition metal species

to develop a carbon-based catalyst loaded with nanoscale S-doped Co_2P particles. The sintering phenomenon of transition metal phosphides under high temperatures were reduced, ensuring the utmost exposure of active sites. The ESCA of the sample subjected to ion exchange is 2.4 times higher compared to sample subjected to physical mixing only. In addition, the introduction of S species can grab extra electrons from the Co site and regulate the electronic structure of the active center, so that the hydrogen adsorption free energy (ΔG_{H^*}) of the catalyst is closer to the thermo-neutral state, which improves the HER activity. The TOF(η = 250 mV) fo the sample doping S atoms was elevated from 0.021 s^{-1} to 0.085 s^{-1}, compared to sample without S element, suggesting there is 4-fold increase in intrinsic activity of the catalyst after doping S atoms.

Summary of Chapter 6

In Chapter 6, I developed N, P co-doped carbon-based catalysts based on the crosslinking interaction between phytic acid and glycine. By modulating precursors concentration, ultrathin heteroatom-doped carbon nanosheets were successfully prepared. Building on this, further optimization of precursor ratios and carbonization temperature yielded a series of products with gradient variations in N and P doping type and content. By combining DFT calculations with experimental data we found that when the graphitic N co-doped at the meta site of C_3PO, they have a synergistic effect and optimal hydrogen adsorption free energy (ΔG_{H^*}=0.13). In addition, the graphitic N can inject the lone electron into the large π bond, so that the HOMO orbital energy of graphene is enhanced and the HOMO-LUMO spacing is reduced, which accelerates the charge transfer rate and facilitates the adsorption reaction. The best catalyst exhibited outstanding HER activity, with an extraordinarily low overpotential of 306 mV at 10 mA cm^{-2}.

Summary of Chapter 7

In Chapter 7, I investigated the influence of precursor type on the distribution and content of nitrogen and phosphorus dopants in the final product. Using histidine and linear amino acids as comparative precursors, the research focuses on evaluating the optimization mechanism and enhancement effect of the imidazole ring on the catalytic performance of N, P-co-doped carbon-based materials, providing theoretical support and experimental evidence for the preparation of high-performance heteroatom-doped carbon-based catalysts.

List of Publications

1. **Xinran Yang**, Ryuji Takada, Xinyu Li, Kotaro Narimatsua, Koji Miyake, Yoshiaki Uchida and Norikazu Nishiyama., Undemanding synthesis of N, P co-doped carbon nanosheets for the hydrogen evolution reaction: combining experimental quantitative analysis and DFT calculation corroboration, J. Mater. Chem. A, 2025, 13, 13884-13897.
2. **Xinran Yang**, Ryuji Takada, Yurika Taniguchi, Koji Miyake, Tao Zheng, Yoshiaki Uchida, Norikazu Nishiyama., Straightforward synthesis of S-doped Co_2P nanoparticles on a P, S co-doped carbon substrate by using ion exchange resin for hydrogen evolution reaction., Fuel, 2024, 370, 131674.
3. **Xinran Yang**, Yasuhiro Shu, Ryuji Takada, Yurika Taniguchi, Koji Miyake, Yoshiaki Uchida and Norikazu Nishiyama., Facile and Cost-effective Synthesis of CoP@N-doped Carbon with High Catalytic Performance for Electrochemical Hydrogen Evolution Reaction, Chem Asian J. 2023, 18, e202300534.

Related papers

1. Xinyu Li, **Xinran Yang**, Zahratul Amanah, Koji Miyake, Yoshiaki Uchida and Norikazu Nishiyama., Pore size control of ordered mesoporous carbon by amino acid addition in solvent-free soft-template preparation., Microporous and Mesoporous Materials. 2025: 113831.
2. Ryuji Takada, Yasuhiro Shu, Yurika Taniguchi, **Xinran Yang**, Koji Miyake, Yoshiaki Uchida and Norikazu Nishiyama., Facile synthesis of carbon co-doped with nitrogen and phosphorus as Metal free electrocatalyst with precisely controlled pore structure and dual heteroatoms for oxygen reduction reaction, Carbon 218 (2024) 118719.
3. Yurika Taniguchi, Shinya Kokuryo, Ryuji Takada, **Xinran Yang**, Koji Miyake, Yoshiaki Uchida and Norikazu Nishiyama., Fluoropyridine-medicated zeolite templating method for N/F co-doped carbon with high electrocatalytic performance on oxygen reduction reaction, Electrochemistry Communications. 160 (2024)107665.
4. Yurika Taniguchi, Shinya Kokuryo, Ryuji Takada, **Xinran Yang**, Koji Miyake, Yoshiaki Uchida and Norikazu Nishiyama., Synthesis of N-doped carbon with a high concentration of pyridinic N using a zeolite template method with pyridine as the deposition source, Carbon Reports. 2024, 3(1): 11-17.
5. Yasuhiro Shu, Ryuji Takada, Yurika Taniguchi, **Xinran Yang**, Koji Miyake, Yoshiaki Uchida and Norikazu Nishiyama., Facile Synthesis of N Doped Metal-Free Catalysts for Oxygen Reduction Reaction via a Self-Sacrificed Template Method Using Zinc Amino-Acid Complex, ACS Omega. 2023, 8, 46276−46283.
6. Ryuji Takada, Kotaro Narimatsu, Yurika Taniguchi, **Xinran Yang**, Koji Miyake, Yoshiaki Uchida and Norikazu Nishiyama., Nitrogen, Fluorine, and Phosphorus Tri-Doped Porous Carbon with High Electrical Conductivity as an Excellent Metal-Free Electrocatalyst for Oxygen Reduction Reaction, ChemCatChem, 2024, 16(21): e202400749.

Acknowledge

Firstly, I would like to express my deep and sincere gratitude to Professor Norikazu Nishiyama, Associate Professor Yoshiaki Uchida and Dr. Koji Miyake, for all the guidance and support for this research. I really appreciate that Professor Nishiyama allowed me to do research and provided invaluable guidance for not only the research but also life in Japan. He gave me a lot of advice on my research and taught me to think critically. Professor Uchida gave me a lot of advice about further research. Miyake sensei always helped me set up a new process for experiments and patiently taught me to do experiments. I really appreciate his supervision and crucial comments in research. They helped me revise papers, always carefully and patiently. It was a great privilege and honor to work and study under their guidance.

I would like to say thanks to Dr Li XINYU, Dr. Yasuhiro Shu, Dr. Hernandez Gaitan, J. A., and Ms. Kaixin Ye. We often engage in academic exchanges and daily life interactions, making our doctoral years fulfilling and joyful. Their expertise, constructive feedback, and collaborative spirit have significantly enriched my research and helped me overcome challenges with clarity and confidence.

Next, I would like to express my gratitude to all members of the Carbon Group. The vibrant academic environment of the Carbon Group has facilitated numerous breakthroughs, particularly tin the field of carbon-based catalyst design. Our team members have conducted extensive discussions on material synthesis, characterization techniques, and catalytic performance analysis, which not only improved my methodology but also inspired me to explore innovative perspectives. Whether in laboratory meetings or joint experiments, the exchange of ideas has played an important role in the formation of this work.

I sincerely thank all the members of our laboratory for their consistent enthusiasm and collaborative spirit throughout my research process. The vibrant atmosphere they created is filled with shared curiosity, lively discussions, and mutual support, which is the cornerstone of my academic growth. Sincere thanks to everyone for taking care of me

Last, I am grateful to my parents for their financial and emotional support. They covered all the costs of my studies abroad, and I am very grateful for that. They always cared about me and were willing to share their lives with me. I hope they will be in good health and happy every day.

Xinran Yang

2026